Vierbein walls in condensed matter

G. E. Volovik

Low Temperature Laboratory, Helsinki University of Technology, P. O. Box 2200, FIN-02015 HUT, Finland; L. D. Landau Institute of Theoretical Physics, 117940 Moscow, Russia

The effective field, which plays the part of the vierbein in general relativity, can have topologically stable surfaces, vierbein domain walls, at which the effective contravariant metric is degenerate. We consider vierbein walls separating domains with flat spacetime which are not causally connected at the classical level. The possibility of a quantum mechanical connection between the domains is discussed. © *1999 American Institute of Physics.* [S0021-3640(99)00123-1]

PACS numbers: 67.57.−z, 74.20.−z, 04.20.Gz

In some classes of superfluids and superconductors there is an effective field arising in the low-energy corner which acts on quasiparticles as a gravitational field. Here we discuss topological solitons representing the vierbein domain wall in superfluids and superconductors. On such a surface in 3D space (or on the 3D hypersurface in $3+1$ space) the vierbein is degenerate, so that the determinant of the contravariant metric $g^{\mu\nu}$ becomes zero on the surface. An example of the vierbein domain was discussed in Ref. 1 for a ^{3}He-A film. When such a vierbein wall moves, it splits into a black hole/white hole pair, which experiences the quantum friction force due to Hawking radiation.[1] Here we discuss a stationary wall, which is topologically stable and thus does not experience any dissipation. Such domain walls, at which one of the three ''speeds of light'' crosses zero, can be realized in other condensed matter, too: in superfluid ^{3}He-B,[2] in chiral p-wave superconductors,[3,4] and in d-wave superconductors.[5]

In the literature two types of the walls have been considered: with degenerate $g^{\mu\nu}$ and with degenerate $g_{\mu\nu}$ (Ref. 6). The case of degenerate $g_{\mu\nu}$ was discussed in detail in Refs. 6 and 7. Both types of wall could be generic. According to Horowitz,[8] for a dense set of coordinate transformations the generic situation is the 3D hypersurface on which the covariant metric $g_{\mu\nu}$ has rank 3.

The physical origin of the walls with the degenerate metric $g^{\mu\nu}$ in general relativity has been discussed by Starobinsky.[9] They can arise after inflation, if the inflaton field has a Z_2 degenerate vacuum. The domain walls separate domains with 2 different vacua of the inflaton field. The metric $g^{\mu\nu}$ can everywhere satisfy the Einstein equations in vacuum, but on the surfaces considered, the metric $g^{\mu\nu}$ cannot be diagonalized as $g^{\mu\nu} = \text{diag}(1,-1,-1,-1)$. Instead, on such a surface the metric is diagonalized as $g^{\mu\nu} = \text{diag}(1,0,-1,-1)$ and thus cannot be inverted. Though the spacetime can be flat everywhere, such a surface cannot be removed by a coordinate transformation: it can only

be moved to infinity. Thus the system of such vierbein domain walls divides the space-time into domains which cannot communicate with each other. Each domain is flat and infinite as viewed by a local observer living in a given domain. In principle, the domains can have different spacetime topology, as is emphasized by Starobinsky.[9]

Here we consider the vierbein walls separating flat spacetime domains that classically cannot communicate with each other across the wall, and we discuss the quantum mechanical behavior of fermions in the presence of the domain wall.

VIERBEIN DOMAIN WALL

The simplest example of the vierbein walls we are interested in is provided by the domain wall which separates domains having opposite orientations of the unit vector $\hat{\mathbf{l}}$ of the orbital momentum of Cooper pairs in a superfluid ^{3}He-A film: $\hat{\mathbf{l}} = \pm\hat{\mathbf{z}}$. Here the $\hat{\mathbf{z}}$ is along the normal to the film. The Bogoliubov–Nambu Hamiltonian for fermionic quasiparticles is

$$\mathcal{H} = \left(\frac{p_x^2 + p_y^2 - p_F^2}{2m}\right)\tau^3 + \mathbf{e}_1 \cdot \mathbf{p}\tau^1 + \mathbf{e}_2 \cdot \mathbf{p}\tau^2. \tag{1}$$

Here τ^a are 2×2 matrices for the Bogoliubov–Nambu spin; $\mathbf{p} = \hat{\mathbf{x}}p_x + \hat{\mathbf{y}}p_y$ is the 2D momentum (for simplicity we assume that the film is narrow, so that the motion along the normal to the film is quantized and only the motion along the film is free); the complex vector

$$\mathbf{e} = \mathbf{e}_1 + i\mathbf{e}_2, \quad \hat{\mathbf{l}} = \frac{\mathbf{e}_1 \times \mathbf{e}_2}{|\mathbf{e}_1 \times \mathbf{e}_2|} = \pm\hat{\mathbf{z}} \tag{2}$$

is the order parameter. If one considers the first term in Eq. (1) as the mass term, then the vectors $\mathbf{e}_1$ and $\mathbf{e}_2$ play the part of the zweibein for the 2D motion in the film. We assume the following order parameter texture in the wall:

$$\mathbf{e}_1(x) = \hat{\mathbf{x}}c_x(x), \quad \mathbf{e}_2 = \hat{\mathbf{y}}c_y(x), \tag{3}$$

where the ''speed of light'' is constant for light propagating along the y axis, while the ''speed of light'' changes sign across the wall for light propagating along the x axis:

$$c_y(x) = c_0, \quad c_x(x) = c_0 \tanh(x/d). \tag{4}$$

At $x=0$ the zweibein is degenerate: the vector product $\mathbf{e}_1 \times \mathbf{e}_2 = 0$, so that the vector $\hat{\mathbf{l}}$ is not determined.

Since the momentum projection p_y is a conserved quantity, we come to pure $1+1$ motion. Further we assume that: (i) $p_y = \pm p_F$; and (ii) the parameters of the system are such that the thickness d of the domain wall is large: $d \gg \hbar/mc_0$. This allows us to consider the range of the momentum $\hbar/d \ll p_x \ll mc_0$, where the term p_x^2 can be either neglected as compared to the linear term or considered in the semiclassical approximation. Then, rotating the Bogoliubov spin and neglecting the noncommutativity of the p_x^2 term and $c(x)$, one has the following Hamiltonian for the $1+1$ particle:

$$\mathcal{H} = M(\mathcal{P})\tau^3 + \frac{1}{2}(c(x)\mathcal{P} + \mathcal{P}c(x))\tau^1, \tag{5}$$

$$M^2(\mathcal{P}) = \mathcal{P}^4/4m^2 + c_0^2 p_y^2, \tag{6}$$

where the momentum operator $\mathcal{P}_x = -i\partial_x$ is introduced. If the $\mathcal{P}^2$ term is completely neglected, one obtains the $1+1$ Dirac fermions

$$\mathcal{H} = M\tau^3 + \frac{1}{2}(c(x)\mathcal{P} + \mathcal{P}c(x))\tau^1, \tag{7}$$

$$M^2 = M^2(\mathcal{P}=0) = c_0^2 p_y^2. \tag{8}$$

The classical spectrum of quasiparticles,

$$E^2 - c^2(x)p_x^2 = M^2, \tag{9}$$

corresponds to the contravariant metric

$$g^{00} = 1, \quad g^{xx} = -c^2(x). \tag{10}$$

The line element of the effective spacetime is

$$ds^2 = dt^2 - (c(x))^{-2} dx^2. \tag{11}$$

The metric element g_{xx} is infinite at $x=0$.

Equation (11) represents a *flat* effective spacetime for any function $c(x)$. However the singularity at $x=0$, where $g_{xx}=\infty$, cannot be removed by a coordinate transformation. If at $x>0$ one introduces a new coordinate $\xi = \int dx/c(x)$, then the line element takes the standard flat form

$$ds^2 = dt^2 - d\xi^2. \tag{12}$$

However, the other domain – the half space with $x<0$ – is completely removed by such a transformation. The situation is thus the same as that discussed by Starobinsky for the domain wall in the inflaton field.[9]

The two flat spacetimes are disconnected in the relativistic approximation. However, this approximation breaks down near $x=0$, where the ''Planck energy physics'' becomes important and nonlinearity in the energy spectrum appears in Eq. (6): The two halves actually communicate due to high-energy quasiparticles, which are superluminal and thus can propagate through the wall.

FERMIONS ACROSS A VIERBEIN WALL

In the classical limit, low-energy relativistic quasiparticles do not communicate across the vierbein wall, because the speed of light $c(x)$ vanishes at $x=0$. However, a quantum mechanical connection may be possible. There are two ways to treat the problem. One approach is to do the coordinate transformation first. Then in one of the domains, say, at $x>0$, the line element is Eq. (12), and one comes to the standard solution for a Dirac particle propagating in flat space:

$$\chi(\xi) = \frac{A}{\sqrt{2}}\exp(i\xi\tilde{E})\begin{pmatrix} Q \\ Q^{-1} \end{pmatrix} + \frac{B}{\sqrt{2}}\exp(-i\xi\tilde{E})\begin{pmatrix} Q \\ -Q^{-1} \end{pmatrix}, \tag{13}$$

$$\tilde{E} = \sqrt{E^2 - M^2}, \quad Q = \left(\frac{E+M}{E-M}\right)^{1/4}. \tag{14}$$

Here A and B are arbitrary constants. In this approach it makes no sense to discuss any connection to the other domain, which simply does not exist in this representation.

In the second approach we do not make the coordinate transformation and we work with both domains. The wave function for the Hamiltonian (7) at $x>0$ follows from the solution in Eq. (13) after restoring the old coordinates:

$$\chi(x>0)=\frac{A}{\sqrt{2c(x)}}\exp(i\xi(x)\widetilde{E})\begin{pmatrix} Q \\ Q^{-1} \end{pmatrix}+\frac{B}{\sqrt{2c(x)}}\exp(-i\xi(x)\widetilde{E})\begin{pmatrix} Q \\ -Q^{-1} \end{pmatrix}, \quad (15)$$

$$\xi(x)=\int^x \frac{dx}{c(x)}. \tag{16}$$

A similar solution exists for $x<0$. We can now connect the solutions for the right and left half spaces using (i) the analytical continuation across the point $x=0$; and (ii) the conservation of the quasiparticle current across the interface. The quasiparticle current at $x>0$, for example, is

$$j=c(x)\chi^\dagger \tau^1 \chi=|A|^2-|B|^2. \tag{17}$$

The analytical continuation depends on the choice of the contour around the point $x=0$ in the complex x plane. Thus, starting from Eq. (16), we obtain two possible solutions at $x<0$. The first solution is obtained when the point $x=0$ is shifted to the lower half plane:

$$\chi^{\mathrm{I}}(x<0)=\frac{-iAe^{-\widetilde{E}/2T_H}}{\sqrt{2|c(x)|}}\exp(i\xi(x)\widetilde{E})\begin{pmatrix} Q \\ Q^{-1} \end{pmatrix}$$

$$+\frac{-iBe^{\widetilde{E}/2T_H}}{\sqrt{2|c(x)|}}\exp(-i\xi(x)\widetilde{E})\begin{pmatrix} Q \\ -Q^{-1} \end{pmatrix}, \tag{18}$$

where T_H is

$$T_H=\frac{\hbar}{2\pi}\frac{dc}{dx}\Big|_{x=0}. \tag{19}$$

Conservation of the quasiparticle current (17) across the point $x=0$ gives the connection between parameters A and B:

$$|A|^2-|B|^2=|B|^2 e^{\widetilde{E}/T_H}-|A|^2 e^{-\widetilde{E}/T_H}. \tag{20}$$

The quantity T_H looks like the Hawking radiation temperature determined at the singularity. As follows from Ref. 1, it is the limit of the Hawking temperature when the white hole and black hole horizons in the moving wall merge to form the static vierbein wall. Note that there is no real radiation if the wall does not move. The parameter $T_H/\widetilde{E}\sim\partial\lambda/\partial x$, where $\lambda=2\pi/p_x=(2\pi/\widetilde{E})\partial c/\partial x$ is the de Broglie wavelength of the quasiparticle. Thus the quasiclassical approximation holds if $T_H/\widetilde{E}\ll1$.

The second solution is obtained when the point $x=0$ is shifted to the upper half plane:

$$\chi^{II}(x<0) = \frac{iAe^{\tilde{E}/2T_H}}{\sqrt{2|c(x)|}}\exp(i\xi(x)\tilde{E})\begin{pmatrix} Q \\ Q^{-1} \end{pmatrix} + \frac{iBe^{-\tilde{E}/2T_H}}{\sqrt{2|c(x)|}}\exp(-i\xi(x)\tilde{E})\begin{pmatrix} Q \\ -Q^{-1} \end{pmatrix},$$

(21)

and the conservation of current gives the following relation between parameters A and B:

$$|A|^2 - |B|^2 = |B|^2 e^{-\tilde{E}/T_H} - |A|^2 e^{\tilde{E}/T_H}.$$

(22)

Two solutions, the wave functions χ^I and χ^{II}, are connected by the relation

$$\chi^{II} \propto \tau_3(\chi^I)^*$$

(23)

which follows from the symmetry of the Hamiltonian

$$H^* = \tau_3 H \tau_3.$$

(24)

The general solution is a linear combination of χ^I and χ^{II}.

Though on the classical level the two worlds on either side of the singularity are well separated, there is a quantum mechanical interaction between the worlds across the vierbein wall. The wave functions across the wall are connected by the relation $\chi(-x) = \pm i\tau_3\chi^*(x)$ in spite of the impossibility of communication in the relativistic regime.

NONLINEAR (NONRELATIVISTIC) CORRECTION

In the above derivation we relied upon the analytical continuation and on the conservation of quasiparticle current across the wall. Let us justify this using the nonlinear correction in Eq. (6), which was neglected before. We shall work in the quasiclassical approximation, which holds if $\tilde{E} \gg T_H$. In the purely classical limit one has the dispersion relation

$$E^2 = M^2 + c^2(x)p_x^2 + p_x^4/4m^2,$$

(25)

which determines two classical trajectories

$$p_x(x) = \pm\sqrt{2m(\sqrt{\tilde{E}^2 + m^2 c^4(x)} - mc^2(x))}.$$

(26)

It is clear that there is no singularity at $x=0$—the two trajectories cross the domain wall continuously in opposite directions, while the Bogoliubov spin continuously changes its direction. Far from the wall these two trajectories give the two solutions, χ^I and χ^{II}, in the quasiclassical limit $\tilde{E} \gg T_H$. The function χ^I

$$\chi^I(x>0) = \frac{1}{\sqrt{2|c(x)|}}\exp(i\xi(x)\tilde{E})\begin{pmatrix} Q \\ Q^{-1} \end{pmatrix},$$

(27)

$$\chi^I(x<0) = \frac{-i}{\sqrt{2|c(x)|}}\exp(-i\xi(x)\tilde{E})\begin{pmatrix} Q \\ -Q^{-1} \end{pmatrix},$$

(28)

describes the propagation of the quasiparticle from the left to the right without reflection at the wall: in the quasiclassical limit reflection is suppressed. The function χ^{II} describes the propagation in the opposite direction:

$$\chi^{\text{II}}(x>0)=\frac{1}{\sqrt{2|c(x)|}}\exp(-i\xi(x)\tilde{E})\begin{pmatrix} Q \\ -Q^{-1} \end{pmatrix},\qquad(29)$$

$$\chi^{\text{II}}(x<0)=\frac{i}{\sqrt{2|c(x)|}}\exp(i\xi(x)\tilde{E})\begin{pmatrix} Q \\ Q^{-1} \end{pmatrix}.\qquad(30)$$

The quasiparticle current far from the wall does obey Eq. (17) and is conserved across the wall. This confirms the result of the previous Section as to the presence of a quantum mechanical connection between the spaces.

In the limit of small mass $M\to 0$, the particles become chiral, with the spin directed along or opposite to the momentum p_x. The spin structure of the wave function in the semiclassical approximation is given by

$$\chi(x)=e^{i\tau_2\frac{\alpha}{2}}\chi(+\infty),\quad \tan\alpha=p_x/2mc(x).\qquad(31)$$

Since α changes by π across the wall, the spin of the chiral quasiparticle rotates by π: the right-handed particle transforms to the left-handed one when the wall is crossed.

It appears that there is a quantum mechanical coherence between the two flat worlds, which classically do not interact across the vierbein wall. The coherence is established by the nonlinear correction to the spectrum of the chiral particle: $E^2(p)=c^2p^2+ap^4$. The parameter a is positive in the condensed-matter analogy, which allows the superluminal propagation across the wall at high momenta p. But the result does not depend on the magnitude of a: in the relativistic low-energy limit the amplitudes of the wave function on the left and right sides of the wall remain equal in the quasiclassical approximation, even though communication across the wall is classically forbidden in the low-energy corner. Thus the only relevant input of the ''Planck energy'' physics is the mere possibility of superluminal communication between the worlds across the wall. That is why coherence between particles propagating in two classically disconnected worlds can be obtained even in the relativistic domain, by using analytical continuation and the conservation of the particle current across the vierbein wall.

[1] T. A. Jacobson and G. E. Volovik, JETP Lett. **68**, 874 (1998).
[2] M. M. Salomaa and G. E. Volovik, Phys. Rev. B **37**, 9298 (1988); J. Low Temp. Phys. **74**, 319 (1989).
[3] M. Matsumoto and M. Sigrist, J. Phys. Soc. Jpn. **68**, 994 (1999); http://xxx.lanl.gov/abs/cond-mat/9902265.
[4] M. Sigrist and D. F. Agterberg, http://xxx.lanl.gov/abs/cond-mat/9910526.
[5] G. E. Volovik, JETP Lett. **66**, 522 (1997).
[6] I. Bengtsson, Class. Quantum Grav. **8**, 1847 (1991).
[7] I. Bengtsson and T. Jacobson, Class. Quantum Grav. **14**, 3109 (1997); erratum *ibid.* **15**, 3941 (1998).
[8] G. T. Horowitz, Class. Quantum Grav. **8**, 587 (1991).
[9] A. Starobinsky, Plenary talk at Cosmion-99, Moscow, 17–24 October, 1999.

Quark and gluon condensates in a magnetic field

N. O. Agasian*[)] and I. A. Shushpanov†[)]

Institute of Theoretical and Experimental Physics, 117218 Moscow, Russia

The two-loop expression for the vacuum energy density in a constant magnetic field is obtained on the basis of the chiral perturbation theory. The dependence of the quark and gluon condensates on the field intensity H is found. © *1999 American Institute of Physics.* [S0021-3640(99)00223-6]

PACS numbers: 12.39.Fe, 12.38.Bx

1. The dependence of the quark condensate on the magnetic field H in the Nambu–Jona–Lasinio model was investigated in Ref. 1. For quantum chromodynamics (QCD) the single-loop result was obtained in Ref. 2. In both cases it was found that the condensate grows with increasing H, which shows that the naive analogy with superconductivity theory, where the Cooper-pair condensate is destroyed by a magnetic field, is inapplicable.

In the present letter, on the basis of the chiral perturbation theory (ChPT) for small (compared with the characteristic hadronic scale) values of eH, the two-loop approximation is obtained for the vacuum energy density and the dependence of the quark and gluon condensates on the field intensity is found. We note that although gluons do not carry electric charge, the virtual quarks whcich they generate and which interact with a magnetic field, change the gluon condensate.

2. In the Euclidean formulation the QCD partition function in the presence of an external Abelian field A_μ can be written in the form

$$Z = \exp\left\{ -\frac{1}{4} \int d^4x F_{\mu\nu}^2 \right\} \int [\mathcal{D}B_\mu^a][\mathcal{D}\bar{q}_f][\mathcal{D}q_f] \exp\left\{ -\int d^4x L_{\text{QCD}} \right\}, \tag{1}$$

where the QCD Lagrangian in the background field has the form

$$L_{\text{QCD}} = \frac{1}{4g_0^2}(G_{\mu\nu}^a)^2 + \sum_f \bar{q}_f \left[\gamma_\mu \left(\partial_\mu - iQ_f eA_\mu - i\frac{\lambda^a}{2}B_\mu^a \right) + m_f \right] q_f, \tag{2}$$

Q_f is the charge matrix of quarks with flavor $f = (u,d)$, and for simplicity we do not write here explicitly the ''ghost'' and gauge-fixing terms.

The energy density of the system is determined by the expression $V_4 \epsilon_v(H,m_f) = -\ln Z$. In a constant magnetic field H a quark condensate in the chiral limit ($m_f \to 0$) can be written in the form

$$\langle \bar{q}_f q_f \rangle(H) = \frac{\partial \epsilon_v(H, m_f)}{\partial m_f}\bigg|_{m_f=0}. \tag{3}$$

It follows from Eq. (1) that the gluon condensate $\langle G^2 \rangle \equiv \langle (G^a_{\mu\nu})^2 \rangle$ is determined by the relation

$$\langle G^2 \rangle = 4\frac{\partial \epsilon_v(H, m_f)}{\partial(1/g_0^2)}\bigg|_{m_f=0}. \tag{4}$$

The phenomenon of dimensional transmutation leads to the appearance of a nonperturbative dimensional parameter

$$\Lambda = M \exp\left\{ \int_{\alpha_s(M)}^{\infty} \frac{d\alpha_s}{\beta(\alpha_s)} \right\}, \tag{5}$$

where M is the ultraviolet-cutoff mass, $\alpha_s = g_0^2/4\pi$, and $\beta(\alpha_s) = d\alpha_s(M)/d\ln M$ is the Gell-Mann–Low function. The system described by the partition function (1) contains in the chiral limit ($m_f = 0$) two dimensional parameters M and H. Since the vacuum energy density is an observable quantity, it possesses the property of renormalization invariance and its anomalous dimension is zero. Therefore ϵ_v possesses only a normal (canonical) dimension, equal to 4. Using the renormalization invariance of Λ, we can write

$$\epsilon_v = \Lambda^4 f(H/\Lambda^2), \tag{6}$$

where f is an unknown function. It is easy to obtain from Eqs. (5) and (6)

$$\frac{\partial \epsilon_v}{\partial(1/g_0^2)} = \frac{8\pi\alpha_s^2}{\beta(\alpha_s)}\left(2 - H\frac{\partial}{\partial H}\right)\epsilon_v. \tag{7}$$

Using the expression (4), we find for the gluon condensate

$$\langle G^2 \rangle(H) = \frac{32\pi\alpha_s^2}{\beta(\alpha_s)}\left(2 - H\frac{\partial}{\partial H}\right)\epsilon_v. \tag{8}$$

In the absence of an external field we obtain the well-known expression for the nonperturbative vacuum energy density in the chiral limit, which in the single-loop approximation ($\beta = -b_0\alpha_s^2/2\pi$, $b_0 = (11N_c - 2N_f)/3$) has the form

$$\epsilon_v = -\frac{b_0}{128\pi^2}\langle G^2 \rangle. \tag{9}$$

3. The formulas obtained make it possible to find the values of the condensates in the chiral limit as a function of H, provided the vacuum energy density is known. To calculate ϵ_v the vacuum loops in an external magnetic field must be examined. For weak fields $eH \ll \mu_{\text{hadr}}^2 \sim (4\pi F_\pi)^2$ the characteristic momenta in the loops are small and the theory is adequately described by an effective low-energy chiral Lagrangian L_{eff},[3] which can be represented as a series expansion in the momenta (derivatives) and masses:[1)]

$$L_{\text{eff}} = L^{(2)} + L^{(4)} + L^{(6)} + \cdots \tag{10}$$

The leading term in Eq. (10) is similar to the Lagrangian of the nonlinear σ model in an external vector field V_μ

$$L^{(2)} = \frac{F_\pi^2}{4} \text{Tr}(\nabla_\mu U^+ \nabla_\mu U) + \Sigma \text{ReTr}(\mathcal{M}U^+), \tag{11}$$

$$\nabla_\mu U = \partial_\mu U - i[U, V_\mu].$$

Here U is a unitary $SU(2)$ matrix, $F_\pi = 93$ MeV is the pion decay constant, and the parameter Σ is the quark condensate $\Sigma = |\langle \bar{u}u \rangle| = |\langle \bar{d}d \rangle|$. An external Abelian magnetic field H directed along the z axis corresponds to $V_\mu(x) = e(\tau^3/2)A_\mu(x)$, where the vector potential A_μ is chosen in the form $A_1(x) = -Hx_2$. The mass difference between the u and d quarks appears in the effective chiral Lagrangian only quadratically. Further, since to obtain an expression for the quark condensate in the chiral limit only the first derivative with respect to the mass of one of the quarks is used, we can neglect the mass difference between the u and d quarks and assume the mass matrix to be diagonal $\mathcal{M} = m\hat{I}$.

To a first approximation the Lagrangian (11) is identical to the Lagrangian of scalar electrodynamics. The single-loop expression for the magnetic field dependence of the vacuum energy in this theory was found by Schwinger[4]

$$\epsilon_v^{(1)}(H) = -\frac{1}{16\pi^2} \int_0^\infty \frac{ds}{s^3} e^{-M_\pi^2 s} \left[\frac{eHs}{\sinh eHs} - 1 \right]. \tag{12}$$

Using the formulas (3) and (4) and the Gel-Mann–Oakes–Renner (GMOR) relation $2m\Sigma = F_\pi^2 M_\pi^2$, we find an expression for the condensates in a magnetic field:

$$\Sigma(H) = \Sigma \left[1 + \frac{eH \ln 2}{(4\pi F_\pi)^2} \right], \tag{13}$$

$$\langle G^2 \rangle(H) = \langle G^2 \rangle + \frac{\alpha_s^2}{3\pi\beta(\alpha_s)} (eH)^2. \tag{14}$$

In the chiral perturbation theory in an external field a series expansion is made in powers of the parameter $eH/(4\pi F_\pi)^2$. To find ϵ_v in the next order the two-loop diagrams with vertices from $L^{(2)}$, one-loop diagrams with a vertex from $L^{(4)}$, and a tree contribution from $L^{(6)}$ must be taken into account. The Feynman diagrams for $\epsilon_v^{(2)}$ are presented in Fig. 1.

To calculate the two-loop diagrams (a), (b), and (c) we shall require an expansion of the chiral Lagrangian $L^{(2)}$ up to the four-pion vertices. The matrix U can be parameterized in different ways. We employ Weinberg's parameterization

$$U = \sigma + \frac{i\pi^a \tau^a}{F_\pi}, \quad \sigma^2 + \frac{\pi^2}{F_\pi^2} = 1. \tag{15}$$
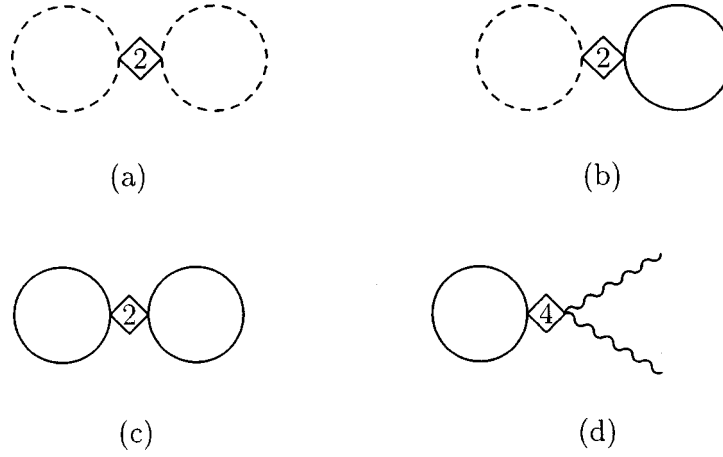
Then the expansion of $L^{(2)}$ has the form

FIG. 1. Diagrams for calculating the vacuum energy density in an external magnetic field in second-order chiral perturbation theory. A solid line corresponds to a charged pion, a broken line corresponds to a neutral pion, and a wavy line corresponds to an external electromagnetic field.

$$L^{(2)} = \frac{1}{2}(\partial_\mu \pi^0)^2 - \frac{M_\pi^2(\pi^0)^2}{2} + (\partial_\mu \pi^+ + ieA_\mu \pi^+)(\partial_\mu \pi^- - ieA_\mu \pi^-) - M_\pi^2 \pi^+ \pi^-$$

$$+ \frac{1}{2F_\pi^2}[\pi^0 \partial_\mu \pi^0 + \partial_\mu(\pi^+ \pi^-)]^2 - \frac{M_\pi^2}{8F_\pi^2}[2\pi^+ \pi^- + (\pi^0)^2]^2, \tag{16}$$

where we have introduced the charged $\pi^\pm$ and neutral π^0 meson fields:

$$\pi^0 = \pi^3, \quad \pi^\pm = \frac{1}{\sqrt{2}}(\pi^1 \pm i\pi^2). \tag{17}$$

The propagator of charged scalar particles in a magnetic field in a Euclidean metric has the form

$$D^H(x,y) = \Phi(x,y) \int \frac{d^4 k}{(2\pi)^4} e^{ik(x-y)} D^H(k), \tag{18}$$

where $\Phi(x,y) = \exp\{ie\int_y^x A_\mu(z)dz_\mu\}$ is the Abelian phase and the integral is taken along a straight line connecting the points x and y. The function $D^{(H)}(k)$ can be written in the form[5]

$$D^H(k) = \int_0^\infty \frac{ds}{\cosh(eHs)} \exp\left\{-s\left(k_\parallel^2 + k_\perp^2 \frac{\tanh eHs}{eHs} + M_\pi^2\right)\right\} \tag{19}$$

and $k_\parallel^2 = k_3^2 + k_4^2$ and $k_\perp^2 = k_1^2 + k_2^2$.

The correction to the vacuum energy density corresponding to the diagram (a) can be written in the form

$$\epsilon_v^{(2)}[\text{diagram(a)}] = -\frac{M_\pi^2}{8F_\pi^2} D^2(0), \tag{20}$$

where $D(0)$ is the free propagator of a scalar massive particle at coinciding points. In dimensional regularization it is

$$D(0) = \int \frac{d^d k}{(2\pi)^d} \frac{1}{k^2 + M^2} = 2M^2\left(\lambda + \frac{1}{32\pi^2}\ln\frac{M^2}{\mu^2}\right), \tag{21}$$

where μ is the mass parameter of dimensional regularization and the singular term

$$\lambda = \frac{\mu^{d-4}}{16\pi^2}\left[\frac{1}{d-4} - \frac{1}{2}(\ln 4\pi - \gamma_E + 1)\right] \tag{22}$$

has been introduced in Eq. (21). The expression (20) does not change the condensates; it simply reduces to renormalization of ϵ_v in the absence of a field.

The diagram (b) gives the following contribution in ϵ_v:

$$\epsilon_v^{(2)}[\text{diagram(b)}] = \frac{M_\pi^2}{2F_\pi^2} D(0)D^H(0), \tag{23}$$

where $D^H(0) = D^H(x,x)$. In accordance with GMOR, the expression (23) is proportional to the squared quark mass, and in the chiral limit it does not contribute to the condensates.

Carrying out the calculations for the diagram in Fig. 1c, we obtain

$$\epsilon_v^{(2)}[\text{diagrm(c)}] = \frac{1}{F_\pi^2} D^H(0)\int \frac{d^d k}{(2\pi)^d}(k^2 + M_\pi^2)D^H(k). \tag{24}$$

This expression contains a quartic divergence. However, in dimensional regularization $\int d^d k = 0$, and this divergence can be dropped.[2] Subtracting 1 from the integrand in Eq. (24) and passing to the limit $d \to 4$, we find that $\epsilon_v^{(2)}[\text{diagram(c)}] = 0$. Therefore the two-loop diagrams do not make a contribution linear in the quark mass to the vacuum energy. Besides the diagrams examined above, in this order the expansion in $eH/(4\pi F_\pi)^2$ also contains single-loop diagrams with vertices from $L^{(4)}$. Since an external field carries zero momentum, only two terms from $L^{(4)}$ are important for us:

$$L^{(4)} = -\frac{2l_5}{F_\pi^2}(eF_{\mu\nu})^2\pi^+\pi^- - \frac{2il_6}{F_\pi^2}eF_{\mu\nu}[\partial_\mu\pi^-\partial_\nu\pi^+ + ieA_\mu\partial_\nu(\pi^+\pi^-)], \tag{25}$$

where the constants l_5 and l_6 are determined in Ref. 3. The corresponding diagrams are presented in Fig. 1d. A direct calculation gives

$$\epsilon_v^{(2)}[\text{diagram(d)}] = \frac{2(eH)^2}{F_\pi^2}(2l_5 - l_6)D^H(0). \tag{26}$$

Although the constants l_5 and l_6 are infinite, their combination appearing in Eq. (26) is finite[3]

$$2l_5 - l_6 = \frac{1}{96\pi^2}(\bar{l}_6 - \bar{l}_5), \tag{27}$$

where $\bar{l}_6 - \bar{l}_5 \approx 2.7$.

The complete expression for $L^{(6)}$ is quite complicated,[7] but for our purposes only one term is important. This term can be written in a form convenient for us as

$$L^{(6)} = \frac{80d}{9F_\pi^4}(eF_{\mu\nu})^2 \Sigma \, \mathrm{Re} \, \mathrm{Tr}\{\mathcal{M}U^+\}. \tag{28}$$

Here $d = d^r(\mu) + \mathrm{const} \cdot \lambda$ and λ contains the pole $\mu^{(d-4)}/(d-4)$. By construction of the chiral perturbation theory, the divergent part in Eq. (28) cancels with the pole terms arising from the single-loop diagrams with vertices from $L^{(4)}$. The quantity d^r can be determined using the results obtained in Ref. 8, where the process $\gamma\gamma \to \pi^0\pi^0$ was considered. Using the notation of Ref. 8, the expression for d^r reduces to the form

$$d^r = \frac{9}{320}(\bar{a}_1 + 2\bar{a}_2 + 4\bar{b}), \tag{29}$$

where $\bar{a}_1$, $\bar{a}_2$, and $\bar{b}$ are coefficients in front of different tensor structures in the amplitude of the process $\gamma\gamma \to \pi^0\pi^0$. The numerical values of $\bar{a}_1$, $\bar{a}_2$, and $\bar{b}$ were determined using the explicit saturation of the amplitude of the process by scalar, vector, and tensor resonances.[8] Calculation shows that only the exchange scalar mesons contribute to d^r and

$$d^r(\mu \sim 0.75 \, \mathrm{GeV}) \approx \pm 4 \cdot 10^{-6}. \tag{30}$$

The ambiguity in the sign of d^r is due to the fact that the coupling constant of a scalar meson with photons or pions appears quadratically in the experimentally measured decay widths, while they appear linearly in the effective Lagrangian and, correspondingly, the sign of d^r is not determined from experiment.

We now obtain the final result. Assuming that to obtain the quark condensate we must retain terms which are only first order in M_π^2, we obtain

$$D^H(0) = [D^H(0) - D(0)] + D(0) \approx -\frac{eH \ln 2}{16\pi^2} + \frac{M_\pi^2}{16\pi^2}\left[\ln\frac{eH}{M_\pi^2} + C\right]$$

$$+ 2M_\pi^2\left[\lambda + \frac{1}{32\pi^2}\ln\frac{M_\pi^2}{\mu^2}\right], \tag{31}$$

where C is a slowly varying function eH/M_π^2 and $C(0) \approx -0.2$. Collecting together the results obtained above, we obtain the final answer for the vacuum energy density

$$\epsilon_v(H) = \epsilon_v(0) + \epsilon_v^{(1)}(H) + \frac{1}{48\pi^2}\frac{(eH)^2}{(4\pi F_\pi)^2}(\bar{l}_6 - \bar{l}_5)$$

$$\times\left\{-eH\ln 2 + M_\pi^2\left[\ln\frac{eH}{\mu^2} + C\right]\right\} - \frac{160d^r(\mu)}{9F_\pi^2}(eH)^2 M_\pi^2. \tag{32}$$

Using the formulas (3) and (8) and the GMOR relation, we find the H dependence of the quark condensate:

$$\Sigma(H) = \Sigma \left\{ 1 + \frac{eH}{(4\pi F_\pi)^2} \ln 2 - \frac{1}{3} \frac{(eH)^2}{(4\pi F_\pi)^4} \right.$$
$$\left. \times \left[(\bar{l}_6 - \bar{l}_5) \left(\ln\frac{eH}{\mu^2} + C \right) - \frac{160(4\pi)^4}{3} d^r(\mu) \right] \right\}. \tag{33}$$

For the gluon condensate we have the expression

$$\langle G^2 \rangle(H) = \langle G^2 \rangle + \frac{\alpha_s^2}{3\pi\beta(\alpha_s)} (eH)^2 \left[1 + 2\frac{eH}{(4\pi F_\pi)^2} (\bar{l}_6 - \bar{l}_5) \ln 2 \right]. \tag{34}$$

On account of asymptotic freedom $\beta(\alpha_s) < 0$ and, correspondingly, the gluon condensate decreases with increasing magnetic field. In the single-loop approximation for the chromodynamic β function ($\beta(\alpha_s) = -b_0\alpha_s^2/2\pi$) this change is

$$\Delta\langle G^2 \rangle = -\frac{2\pi}{3b_0} (eH)^2 \left[1 + 2\frac{eH}{(4\pi F_\pi)^2} (\bar{l}_6 - \bar{l}_5) \ln 2 \right]. \tag{35}$$

We introduce the dimensionless variable $x = eH/(4\pi F_\pi)^2$. Substituting into Eq. (3) the numerical values presented above, we rewrite the quark condensate as a function of x in the form

$$\Sigma(x)/\Sigma = 1 + x \ln 2 - ax^2 \ln x - bx^2. \tag{36}$$

Here $a \simeq 0.9$ and $b \simeq 0.65 \pm 1.77$ where we have used for the coefficient b the two values of d^r from Eq. (30). We note that the behavior of the quark condensate depends fundamentally on the sign of d^r. For $d^r > 0$ the quark condensate starts to decrease for field intensities $x > 0.23$.

4. In summary, on the basis of chiral perturbation theory, a two-loop approximation has been obtained for the vacuum energy density and the dependence of the quark and gluon condensates on H was found. We can see that the gluon condensate decreases with increasing H, while the chiral condensate Σ, depending on the choice of the sign of d^r, in the two-loop level of the ChPT either continues to grow (as happens for one loop) or decreases with increasing H. We note that the decrease of the condensate Σ occurs in the region of applicability of ChPT in a magnetic field $eH/(4\pi F_\pi)^2 < 1$. As discussed above, it is impossible to determine the value of d^r unequivocally by comparing with experimental data. We shall not present here the various speculative arguments about the behavior of Σ in a magnetic field. We confine ourselves only to the assertion that the increase or decrease of the quark condensate with H can be determined only when the coefficients in the effective chiral Lagrangian are calculated from first principles of QCD.

*)e-mail: agasyan@heron.itep.ru

†)e-mail: shushpan@heron.itep.ru

[1] We note that the passage to the chiral limit means that $eH \gg M_\pi^2$.

[2] For other regularizations the quartic divergence vanishes only if a nontrivial measure of integration is taken into account. Examples of explicit two-loop calculations can be found in Ref. 6.

[1] S. P. Klevansky and R. H. Lemmer, Phys. Rev. D **39**, 3478 (1989).

[2] I. A. Shushpanov and A. V. Smilga, Phys. Lett. **402B**, 351 (1997).

[3] J. Gasser and H. Leutwyler, Ann. Phys. (N.Y.) **158**, 142 (1984); J. Gasser and H. Leutwyler, Nucl. Phys. B **250**, 465 (1985).

[4] J. Schwinger, Phys. Rev. **82**, 664 (1951); *Particles, Sources, and Fields* (Addison-Wesley, New York, 1973).

[5] A. Chodos, K. Everding, and D. A. Owen, Phys. Rev. **42**, 2881 (1990).

[6] J. Honerkamp and K. Meetz, Phys. Rev. D **2**, 1996 (1971); J. M. Charap, Phys. Rev. D **2**, 1998 (1971); I. A. Shushpanov and A. V. Smilga, Phys. Rev. D **59**, 054013 (1999).

[7] J. Bijnens, G. Colangelo, and G. Ecker, hep-ph/9907333.

[8] S. Bellucci, J. Gasser, and M. E. Sainio, Nature (London), Phys. Sci. **423**, 80 (1994).

Translated by M. E. Alferieff

Amplification of the generation of the sum-frequency signal in multilayer periodic structures at the edges of the Bragg band gap

A. V. Balakin, V. A. Bushuev, B. I. Mantsyzov, P. Masselin,
I. A. Ozheredov,*) and A. P. Shkurinov

M. V. Lomonosov Moscow State University, 119899 Moscow, Russia

D. Boucher

Laboratoire de PhysicoChimie de l'Atmosphère, Université du Littoral, 59140 Dunkerque, France

A new property of a one-dimensional periodic structure — amplification of the sum-frequency signal arising under the simultaneous action of two laser pulses on this structure with radiation frequencies corresponding to the edges of the fixed Bragg band gap — is experimentally observed and described. © *1999 American Institute of Physics.*
[S0021-3640(99)00323-0]

PACS numbers: 42.70.Qs, 42.65.Ky

1. Investigations of nonlinear-optical phenomena in photonic crystals have been arousing great interest in the last few years.[1] A multilayer periodic structure (MPS) is a particular case of a one-dimensional photonic crystal and is characterized by the existence of regions of forbidden frequencies where total Bragg reflection occurs.[2] In recently published investigations,[3–5] it is shown that a signal at the frequency of the second harmonic can be amplified at the edge of the region of selective Bragg reflection. One possible mechanism of this amplification, examined in Refs. 3 and 4, is due to the linear increase of the energy density of the field at the fundamental frequency.

The subject of the present letter is an investigation of the mechanism of asynchronous amplification of the signal at the sum frequency $\omega_{sf} = \omega_1 + \omega_2$ in an MPS. It is established that the efficiency of the generation of the signal at the sum frequency (SF) ω_{sf} increases substantially if the frequencies ω_1 and ω_2 of the two laser pulses incident on the MPS at the same angle are chosen near the opposite edges of a given Bragg band gap. We believe that our investigations show that this asynchronous amplification is largely due to the simultaneous increase of the energy density of the fields in the structure at the frequencies ω_1 and ω_2. Indeed, under the conditions of our experient the frequency of the sum harmonic lies far from the electronic resonances of the materials used for preparing the MPS and/or Bragg band gaps. This makes it possible to rule out amplification due to synchronous mechanisms, i.e., amplification arising when additional phase-matching conditions are satisfied in the presence of spatial and frequency dispersions.

2. Let us examine the generation of a signal at the sum frequency in an MPS consisting of alternating layers with substantially different refractive indices. It is assumed that the layers with a large refractive index have a large quadratic nonlinearity.

Since the sum-harmonic signal is weak compared with the intensities of the incident waves, and taking into account the fact that the duration of the pulses is much longer than the propagation time of light through the sample, we shall seek the spatially rapidly varying amplitude of the quasistationary fields $E(\mathbf{r},t)=E(\mathbf{r})\exp(-i\omega t)$ at the fundamental frequencies, solving the linear wave equation

$$\Delta^2 E(\mathbf{r})+(\omega n(z)/c)^2 E(\mathbf{r})=0.$$

The exact solution of this equation in an arbitrary layer with number m has the form of a sum of the direct and backward (reflected) plane waves

$$E_{jm}(z)=A_{jm}\exp(ik_{j0}s_{jm}z)+B_{jm}\exp(-ik_{j0}s_{jm}z),$$

where $s_{jm}=(n_{jm}^2-\sin^2\vartheta)^{1/2}$, the indices $j=1,2$ correspond to one of the incident waves, n_{jm} is the refractive index for the j-th wave in the m-th layer, $k_{j0}=2\pi/\lambda_j$, ϑ is the angle of incidence, and z is the coordinate ''into'' the structure. To determine the amplitudes A_{jm} and B_{jm} we used the Parratt's method of recurrence relations,[6] which for the present problem yields the relations

$$A_{j,m+1}=A_{jm}Q_{jm}\frac{g_{jm}+R_{jm}g_{jm}^{-1}}{1+R_{j,m+1}}, \qquad B_{jm}=R_{jm}A_{jm}, \tag{1}$$

$$R_{jm}=\frac{R_{j,m+1}+F_{jm}}{1+R_{j,m+1}F_{jm}}g_{jm}^2, \qquad F_{jm}=\frac{s_{jm}-s_{j,m+1}Q_{jm}^2}{s_{jm}+s_{j,m+1}Q_{jm}^2},$$

where $g_{jm}=\exp(ik_{j0}s_{jm}d_m)$, d_m is the thickness of the m-th layer, $Q_{jm}=1$ and $Q_{jm}=n_{jm}/n_{j,m+1}$, respectively, for the s- and p-polarized waves. The recurrence relations (1) are solved for the boundary conditions $A_{j0}=E_j$; the reflection coefficient of the $N+1$ boundary is $R_{N+1}=0$; the vacuum refractive index is $n_0=1$; $g_0=1$; E_j are the amplitudes of the incident waves; and, N is the number of layers. Assuming that the intensity of the sum-frequency signal in the m-th layer is proportional to $|A_{1m}A_{2m}|^2$ for the direct and $|B_{1m}B_{2m}|^2$ for the backward waves, we shall estimate the total intensity of the SF signal as the sum of the corresponding intensities over all layers of the MPS with a large refractive index.

The computed dependences of the linear reflection coefficient of the MPS described below are presented in Figs. 1a, b for the two wavelengths $\lambda_1=812$ nm and $\lambda_2=733$ nm of the incident linearly p-polarized (i.e., polarized in the plane of incidence) radiation. The values chosen for λ_1 and λ_2 correspond to two edges of the Bragg band gap with angle of incidence of the radiation on the medium (MPS) $\vartheta=25°$. According to Eq. (1), near this value of the angle ϑ the amplitudes of the waves diffracted in the medium grow substantially, and the maximum localization of the energy of the incident radiation in the medium occurs at both wavelengths. This is clearly seen from the theoretical angular dependences of the total energy density of the corresponding backward waves $|B_{1m}|^2$ and $|B_{2m}|^2$ in layers with a large refractive index (Fig. 1a and 1b). For this reason, the efficiency of generation of the reflected SF signal depends on the angle ϑ, and its intensity I_{sf} has a maximum at $\vartheta=25°$ (Fig. 1c), solid line). If λ_1 and λ_2 are
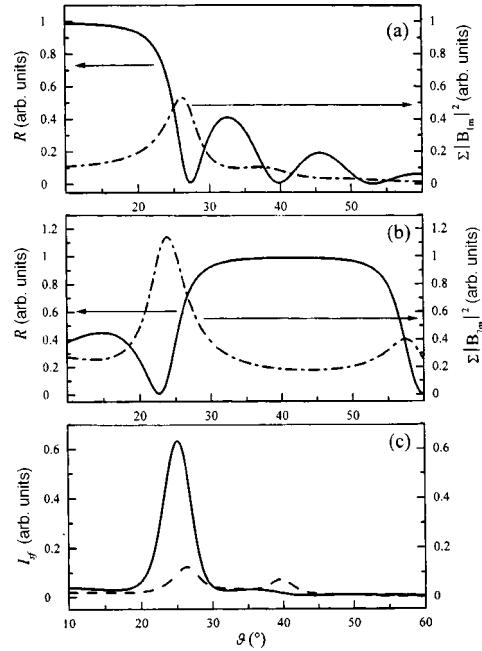
FIG. 1. a, b. Computed dependences of the reflection coefficient R versus the angle of incidence ϑ of the radiation on the MPS for two wavelengths $\lambda_1 = 812$ nm (a) and $\lambda_2 = 733$ nm (solid lines) and the angular dependences of the total energy density of the corresponding backward waves $\Sigma |B_{1m}|^2$ and $\Sigma |B_{2m}|^2$ in non-linear layers (dot-dashed curves); c) computed angular dependences of the intensity I_{sf} of the reflected SF signal with simultaneous incidence of two waves with $\lambda_1 = 812$ nm and $\lambda_2 = 733$ nm (solid line) on the MPS at an angle ϑ and for the case where $\lambda_1 = 812$ nm and $\lambda_2 = 706$ nm (dashed line).

chosen so that the edges of the reflection curves do not intersect, for example, $\lambda_1 = 812$ nm and $\lambda_2 = 706$ nm, the intensity of the SF signal is low, and amplification does not occur (Fig. 1c, dashed line). The second maximum of the SF signal at $\vartheta = 40°$ (Fig. 1c) corresponds to the position of the edge of the reflection curve for $\lambda = 706$ nm.

In summary, for the optimal choice of wavelengths λ_1 and λ_2 amplification of the generation efficiency of the SF frequency, which does not depend on the satisfaction of phase-matching conditions, can be expected.

3. To observe the asynchronous amplification of the SF signal experimentally, we used a sample consisting of eight layers of ZnS ($n_1 = 2.316$) and seven layers of SrF$_2$ ($n_2 = 1.52$), deposited in the form of an MPS on a glass substrate.[4] The thickness of each layer was $d_i = 3\lambda/4n_i$ for wavelength $\lambda = 790$ nm. In all experiments λ_1 was fixed and equal to 812 nm (first channel, ω_1), and λ_2 could vary from 650 to 740 nm (second channel, ω_2); the duration of the pulses was less than 200 fs, the pulse repetition frequency was 200 kHz, and the energy could vary from 0 to 20 nJ/pulse. The synchronous detection technique was used to detect the SF signal. Both radiations at the fundamental frequencies (ω_1 and ω_2) and at the SF were linearly p-polarized.

The efficiency of generation of radiation at the SF as a function of the angle ϑ of incidence on the MPS was measured in the experiments.
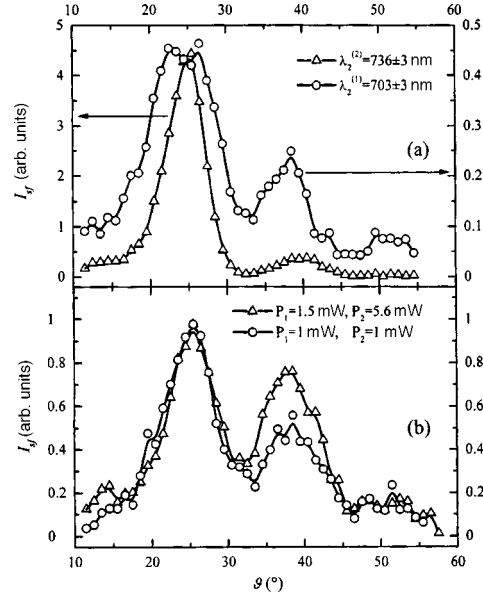
FIG. 2. a) Experimental dependences of the SF signal intensity I_{sf} versus the angle of incidence ϑ on the MPS for two different wavelengths $\lambda_2^{(1)}$ and $\lambda_2^{(2)}$ in the second channel; b) Angular dependence of the SF signal intensity I_{sf} for two different values of the average radiation power (P_1 and P_2) in the channels. The plots are normalized to the signal maximum for $\vartheta = 24°$.

The experimental dependences of the SF signal intensity on the angle of incidence on the MPS are shown in Fig. 2a for two values of the wavelengths of the second channel $\lambda_2^{(1)}$ and $\lambda_2^{(2)}$. The wavelengths $\lambda_2^{(1)} = 736$ nm and $\lambda_2^{(2)} = 703$ nm were chosen so that the edges of the reflection curves corresponding to them and $\lambda_1 = 812$ nm would intersect in one case ($\lambda_2^{(1)}$) and not in the other ($\lambda_2^{(2)}$). For the wavelength $\lambda_2^{(1)}$, an at least ten-fold amplification of the SF signal compared with the case $\lambda_2^{(2)}$ was observed experimentally; this agrees well with the theoretical results (Fig. 1c). The dependence of the SF signal amplitude on the angle of incidence on the MPS is presented in Fig. 2b for various values of the power of the incident radiation. It is evident from the figure that the maximum near $\vartheta = 40°$, corresponding to an increase in the energy density of the field near the edge of the reflection curve for radiation at the wavelength $\lambda_2^{(2)} = 703$ nm, increases with the power of the radiation at the fundamental frequency in the second channel.

4. The good agreement between the theoretical and experimental results shows that we have observed experimentally the asynchronous amplification of the generation of the SF signal in an MPS. The mechanism of such amplification is an increase in the energy density of the localized fields at two frequencies (ω_1, ω_2) near the opposite edges of a fixed Bragg band gap.

de Calais, and Fond Européen de Développement Economique des Régions.

*)e-mail: ilya@lasmed.ilc.msu.su

———————

[1] *Photonic Band Gap Materials,* edited by C. M. Soukoulis (Kluwer Academic, Dordrecht, 1996); E. Yablonovitch, J. Mod. Opt. **41**, 173 (1994).

[2] A. Yariv and P. Yen, *Optical Waves in Crystals, Propagation and Control of Laser Radiation*, John Wiley & Sons, New York, 1984) [Russian translation, Mir, Moscow, 1987, p. 616].

[3] M. Scalora, M. J. Bloemer, A. S. Manka *et al.*, Phys. Rev. A **56**, 3166 (1997); J. W. Haus, R. Viswanathan, M. Scalora *et al.*, Phys. Rev. A **57**, 2120 (1998).

[4] A. V. Balakin, D. Boucher, V. A. Bushuev *et al.*, Opt. Lett. **24**, 793 (1999).

[5] A. V. Andreev, O. A. Andreeva, A. V. Balakin *et al.*, Kvant. Élektron. **28**, 75 (1999) [Quantum Electron. **29**, 632 (1999)].

[6] L. G. Parratt, Phys. Rev. **95**, 359 (1954).

Translated by M. E. Alferieff

Temperature dependence of the spin polarization of composite fermions

I. V. Kukushkin*)

Institute of Solid-State Physics, Russian Academy of Sciences, 142432 Chernogolovka, Moscow Region, Russia; Max Planck Institüt, 70569 Stuttgart, Germany

K. von Klitzing

Max Planck Institute, 70569 Stuttgart, Germany

K. G. Levchenko

Institute of Solid-State Physics, Russian Academy of Sciences, 142432 Chernogolovka, Moscow Region, Russia

Yu. E. Lozovik

Institute of Spectroscopy, Russian Academy of Sciences, 142092 Troitsk, Moscow Region, Russia

It is found that at a critical value of the magnetic field in which a system of composite fermions becomes completely spin-polarized, the temperature dependence of the electronic spin polarization is a linear function at low temperatures. It is shown that the slope of this dependence is determined by the Fermi energy of the composite fermions. This made it possible to measure the Fermi energy and the Zeeman splitting of the composite fermions. A large amplification of the spin splitting of composite fermions for complete spin polarization of the system is found. This makes it possible to measure the strength of the interaction between composite fermions. © *1999 American Institute of Physics.* [S0021-3640(99)00423-5]

PACS numbers: 05.30.Pr, 71.10.Pm

The concept of new quasiparticles, composite fermions, consisting of an electron with an even number of attached magnetic-flux quanta, has been proposed to explain the fractional quantum Hall effect.[1] New states of compressible quantum liquids, realized with fractional fillings of the Landau levels with even denominators, have been predicted on the basis of the composite-fermion picture.[2] The existence of composite fermions has been demonstrated in various experiments in two-dimensional electronic systems in strong magnetic fields.[3–5]

Composite fermions, having the same charge, spin, and statistics as electrons, differ from the latter by the fact that in the mean-field approximation they are influenced by the effective magnetic field $B^* = B - 2n_e\phi_0$, where B is the external field, $\phi_0 = hc/e$ is the magnetic flux quantum, and n_e is the electron density. For half-filling of Landau levels

composite fermions move in a zero effective magnetic field, since the external magnetic field is compensated on the average by the attached magnetic flux quanta of a gauge field. A system of such quasiparticles can be characterized by a definite value of the Fermi energy. A deviation of the magnetic field from the value corresponding precisely to half-filling of the Landau levels leads to the appearance of a nonzero effective magnetic field in which the composite fermions move.

The presence of the *g* factor leads to spin polarization of composite fermions. There arises the interesting question of a transition from a two-component spin-unpolarized state of composite fermions into a completely spin-polarized state. Such a transition can be investigated by keeping the filling ν of the Landau levels fixed and varying the magnetic field. This can be done, for example, by investigating a system with a fixed magnetic field, transverse to the sample, and a varying parallel magnetic field. A different, more direct and reliable, method is to keep ν fixed and to vary at the same time the density of the electron gas and the transverse magnetic field. Since the mass of composite fermions is determined by the fluctuations of a gauge field, and the Zeeman splitting is renormalized by them, the values of these parameters, generally speaking, should vary for large values of the spin polarization (this question will be investigated in detail in a separate work). This makes the problem of the spin polarization of a system of composite fermions interesting and nontrivial.

The present letter is devoted to the experimental and theoretical investigation of the temperature dependence of the spin polarization of composite fermions. By comparing the experimental dependences with the results obtained on the basis of a very simple model of noninteracting composite fermions, we were able to measure the Fermi energy and the Zeeman splitting of the composite fermions.

We measured the spin polarization of the electronic system by analyzing the degree of circular polarization of the radiative recombination of two-dimensional electrons with photoexcited holes bound on acceptors.[6] We note that in this method it is necessary to perform time-resolved measurements of the radiative recombination, specifically, for time delays corresponding to complete thermalization of the photoexcited holes right up to the bath temperature.[7] A detailed description of the experimental method can be found in Refs. 6 and 7.

The characteristic temperature dependences of the electronic spin polarization, which were measured in various magnetic fields with a fixed filling factor of the lowest Landau level $\nu = 1/2$, are shown in Fig. 1a. As shown in Ref. 6, the critical magnetic field at which a transition occurs into a completely spin-polarized state is $B_c = 9.3$ T. As one can see from Fig. 1a, for $B > B_c$ and $B < B_c$ the electronic spin polarization exhibits saturation at low temperatures, while at $B = B_c$ a clearly expressed linear temperature dependence is observed in the limit $T = 0$. To explain the observed linear temperature dependence we shall examine first the very simple case of noninteracting composite fermions.

For fixed ν the electron density n_e, equal to the density n^* of composite fermions, is proportional to the magnetic field (here and below all quantities referring to composite fermions are marked with an asterisk):
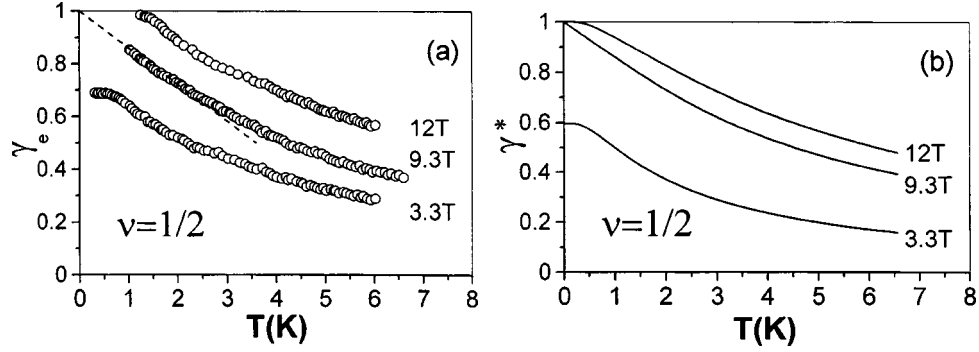
$$n^* = n_e = \frac{eB}{2\pi\hbar c}\nu. \tag{1}$$

FIG. 1. Measured (a) and computed (b) temperature dependences of the electronic spin polarization obtained for $\nu = 1/2$ in various magnetic fields: 12 T, 9.3 T, and 3.3 T. The linear extrapolation for $B = B_c$, from whose slope the Fermi energy of composite fermions was determined, is shown in Fig. 1a.

Let us consider a two-dimensional electronic system, whose filling factor is held constant, equal to $\nu = 1/2$. In this case the motion of the composite fermions is not quantized and the system of these quasiparticles possesses a Fermi surface characterized by the Fermi energy

$$\varepsilon_F^* = \frac{2\pi\hbar^2}{m^*} n_e = \frac{e\hbar}{2m^*c} B, \tag{2}$$

where m^* is the effective mass, which in strong fields (similarly to Ref. 6) should be determined only by the interactions of the electrons and the magnetic field.

The value of the effective mass can be estimated from dimensional analysis[2] as

$$\frac{\hbar^2}{m^*} = \frac{C}{(4\pi n_e)^{1/2}} \frac{e^2}{\epsilon}, \tag{3}$$

where ϵ is the permittivity of the medium and C is a dimensionless constant.

If follows from Eqs. (1)–(3) that $m^* \sim \sqrt{B}$ and therefore $\epsilon_F^* \sim n_e/m^* \sim \sqrt{B}$. Since the Zeeman splitting increases with increasing magnetic field more rapidly than ε_F^*, there exists a nonzero critical value of the magnetic field B_c for which the Fermi energy is equal to the Zeeman splitting $[\varepsilon_F^*(B_c) = E_Z(B_c)]$ and the system becomes completely polarized.

The densities of quasiparticles with different spin orientation are

$$n_\pm = \frac{m^*}{2\pi\hbar^2} \int_0^\infty \frac{1}{\exp\{(\varepsilon \mp E_Z/2 - \mu^*)/T\} + 1} d\varepsilon = \frac{m^*}{2\pi\hbar^2} T\ln(1 + \exp\{(\mu^* \pm E_Z/2)/T\}). \tag{4}$$

Here $\mu^* = \mu^*(T, B)$ is the chemical potential of the system of composite fermions in a magnetic field B at temperature T measured in energy units.

Determining next the degree of spin polarization of the system of quasiparticles as

$$\gamma^*(T,B) = \frac{n_+ - n_-}{n_- + n_+}, \tag{5}$$

expressing the chemical potential μ^* from the condition that the sum of the densities of the quasiparticles with spin parallel and antiparallel to the magnetic field is equal to the total density of the particles in the system in a given field B

$$n_- + n_+ = n_e(B) \tag{6}$$

and substituting the expression (4) and the value of μ^* from Eq. (6) into Eq. (5), we find for the degree of spin polarization of a system of composite fermions

$$\gamma^*(T,B) = 1 - \frac{2T}{\varepsilon_F^*} \ln\left\{ \frac{1}{2}[1 - \exp(-E_Z/T) \right.$$

$$\left. + \sqrt{(1 - \exp(-E_Z/T))^2 + 4\exp((\varepsilon_F^* - E_Z)/T)}] \right\}. \tag{7}$$

Plots of the temperature dependence of the degree of spin polarization of the system of composite fermions, constructed using the formula (7), are presented in Fig. 1b. Comparing Figs. 1a and Fig. 1b, we can see that the experimental and theoretical dependences are in good qualitative agreement with one another.

It is of interest to consider various limiting cases of the formula (7), valid for arbitrary values of T and B. We find from Eq. (7)

$$\gamma^*(T,B) = \begin{cases} \dfrac{E_Z}{\varepsilon_F^*} - \dfrac{T}{\varepsilon_F^*}\exp((E_Z - \varepsilon_F^*)/2T), \\[2mm] B < B_c, \quad T \ll \varepsilon_F^*, \quad E_z, \quad |\varepsilon_F^* - E_Z|; \\[2mm] 1 - \dfrac{2T}{\varepsilon_F^*}\left(\ln((\sqrt{5}+1)/2) - \dfrac{1}{\sqrt{5}}\exp(-\varepsilon_F^*/T) \right), \\[2mm] B = B_c, \quad T \ll \varepsilon_F^*, \quad E_Z; \\[2mm] 1 - \dfrac{2T}{\varepsilon_F^*}\exp\left(\dfrac{\varepsilon_F^* - E_Z}{T} \right), \quad B > B_c, \quad T \ll \varepsilon_F^*, \quad E_Z, \quad |\varepsilon_F^* - E_Z|; \\[2mm] 1 - \dfrac{2T}{\varepsilon_F^*}\left[\ln\left(\dfrac{1+\sqrt{5}}{2} \right) - \dfrac{1}{\sqrt{5}}\exp\left(-\dfrac{E_Z}{T} \right) + \dfrac{2}{\sqrt{5}+5}\dfrac{\varepsilon_F^* - E_Z}{T} \right], \\[2mm] |\varepsilon_F^* - E_Z| \ll T \ll \varepsilon_F^*, \quad E_Z. \end{cases} \tag{8}$$

As one can see from Eq. (8), for $B = B_c$ the temperature dependence of the degree of spin polarization is a linear function at low temperatures and is determined by a single parameter — the Fermi energy of composite fermions. By linearly extrapolating the experimental dependence measured at $B = B_c = 9.3$ T we determined the Fermi energy of composite fermions, which was found to be 6.9 K. Since for $B = B_c$ the values of the Fermi and Zeeman energies are the same, we have $E_Z = E_F = 6.9$ K. Since the electronic Zee-
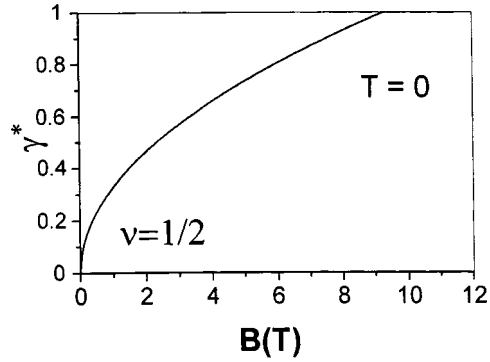
FIG. 2. Computed dependence of the spin polarization of composite fermions ($\nu=1/2$) on the magnetic field at $T=0$ K.

man splitting in GaAs for $B=9.3$ T is 2.8 K, we must conclude that a substantial amplification of the spin splitting (by a factor of 2.5), due to the interaction of composite fermions, is observed in our experiment. Thus the characteristic interaction energy of the composite fermions is about 4–5 K. The effective mass can be determined from the measured Fermi energy of composite fermions for $B=B_c=9.3$ T: $m^*=0.92m_e$, where m_e is the free-electron mass.

It is evident from Eq. (8) that for $B<B_c$, in the low-temperature limit $\gamma^*\sim\sqrt{B}$. The dependence $\gamma^*(B)$, calculated at $T=0$ K assuming a constant g factor for composite fermions ($g^*=1.1$, since $E_Z=6.9$ K for $B=9.3$ T), is shown in Fig. 2. This dependence agrees well with the experimental results of Ref. 6. We obtained the value of the phenomenological parameter $C=0.0892$ from Eq. (3), knowing the mass of composite fermions and their density at $B=B_c=9.3$ T.

A separate work will be devoted to an investigation of Fermi-liquid effects in a system of composite fermions, specifically, the dependence of the effective mass and the Zeeman splitting on the degree of polarization of the system, and the ratio between the mass m^* appearing in the expression for the Fermi energy, and the effective mass of composite fermions, which determines the low-lying excitations of a system of composite fermions.[1] Here we note only that the good agreement between the experimental and theoretical temperature dependences of γ^* attests to the applicability of the picture of noninteracting compact fermions. However, to explain the temperature dependences in fields differing strongly from the critical field, it must be assumed that the Zeeman splitting and the effective mass depend strongly on the degree of polarization of the system.

In summary, in the present work the Fermi energy and the Zeeman splitting of composite fermions were measured from the temperature dependence of the electronic spin polarization for $\nu=1/2$. It was found that the Zeeman splitting, from which the interaction energy of composite fermions is determined, is intensified.

*)e-mail: kukush@issp.ac.ru

[1)]The latter determine, specifically, the Pauli paramagnetism, the specific heat, and so on in a system of composite fermions.

[1] J. K. Jain, Phys. Rev. Lett. **63**, 199 (1989); Adv. Phys. **41**, 105 (1992).

[2] B. I. Halperin, P. A. Lee, and N. Read, Phys. Rev. B **47**, 7312 (1993).

[3] R. L. Willett, R. R. Ruel, K. W. West, and L. N. Pfeiffer, Phys. Rev. Lett. **71**, 3846 (1993).

[4] R. R. Du, H. L. Stormer, D. C. Tsui *et al.*, Phys. Rev. Lett. **70**, 2944 (1993); R. R. Du, A. S. Yeh, H. L. Stormer *et al.*, Phys. Rev. Lett. **75**, 3926 (1995).

[5] W. Kang, H. L. Stormer, L. N. Pfeiffer *et al.*, Phys. Rev. Lett. **71**, 3850 (1993).

[6] I. V. Kukushkin, K. v. Klitzing, and K. Eberl, Phys. Rev. Lett. **82**, 3665 (1999).

[7] I. V. Kukushkin, K. v. Klitzing, and K. Eberl, Phys. Rev. B **55**, 10607 (1997).

[8] I. V. Lerner and Yu. E. Lozovik, Zh. Éksp. Teor. Fiz. **78**, 1167 (1980) [Sov. Phys. JETP **51**, 588 (1980)].

Translated by M. E. Alferieff

Ostwald step rule in films of metastable nanocrystalline alloys Fe–C prepared by pulsed plasma vaporization

R. S. Iskhakov,[a] S. V. Komogortsev, S. V. Stolyar, D. E. Prokof'ev, V. S. Zhigalov, and A. D. Balaev

Institute of Physics, Siberian Branch of the Russian Academy of Sciences, 660036 Krasnoyarsk, Russia

Ferromagnetic nanocrystalline Fe(C) films were prepared by pulsed plasma vaporization. A comprehensive investigation of the structure and magnetic properties made it possible to identify the type of short-range order here and to establish the sequence of structural states occurring in these films in the process of thermal relaxation: fcc-Fe(C)→hcp-Fe(C)→bcc-Fe+C. On the basis of an analysis of the metastable phase diagrams using Ostwald's rule, it is shown that the observed scenario of the structural transformations in these metastable nanocrystalline alloys Fe(C) is a natural phenomenon. © *1999 American Institute of Physics.* [S0021-3640(99)00523-X]

PACS numbers: 81.05.Ys, 75.50.Bb, 75.40.−s

It is well-known that crystalline iron exists in three polymorphic modifications, bcc-Fe (α-Fe, δ-Fe), thermodynamically stable in the temperature range 1183–1667 K Fe (γ-Fe), and thermodynamically stable at high pressures (~130 kbar) hcp-Fe (ϵ-Fe). The latter two modifications of the close-packed structure of Fe in the form of metastable phases can also be obtained at low temperatures and atmospheric pressure. These metastable phases are ordinarily prepared in the form of ultrathin (several molecular layers) films on appropriate substrates[1,2] or small coherent inclusions (precipitates) in the appropriate materials,[3] and in the form of thin films and microwires by fast cooling of the melt.[4,5]

A new technological method, called here pulsed plasma vaporization (PPV) in vacuum, has been developed at the Institute of Physics of the Siberian Branch of the ran.[6–8] In this technology condensation occurs at a high rate (estimated to be ~10^4 Å/s in a pulse), and solidification of the condensate occurs according to the scheme vapor → liquid → crystal. This technology makes it possible to obtain films of a transition metal with a high carbon content (~20 at.%) in a metastable nanocrystalline state.[9]

The purpose of the present work is to identify the initial and investigate the sequence of structural states of films of a nanocrystalline alloy Fe (synthesized under ultrafast condensation conditions), which appear in the process of thermal relaxation.

EXPERIMENTAL PROCEDURE

The experimental methods used in our work are based on a study of the static and dynamic magnetic properties of nanocrystalline Fe films, as well as the atomic and chemical structure of this material. Fe films, 200–2000 Å thick, were obtained on dielectric substrates (cover glass, pyrex glass, NaCl, MgO) by PPV in vacuum with residual-gas pressure $P_0 \approx 5.5 \cdot 10^{-6}$ mm Hg. The atomic structure of the nanocrystalline Fe films prepared by the PPV method was determined by x-ray diffraction of synchrotron radiation (SR) (Institute of Nuclear Physics, Siberian Branch of the Russian Academy of Sciences, Siberian International Center for SR). The SR wavelength was 1.49 Å. The electronic structure and chemical composition of these films were determined from investigations of photoelectron and Auger spectra on a RIBER photoelectron spectrometer (a source with an Mg anode and energy of the Mg K line $h\nu = 1253.6$ eV was used) at the Institute of Semiconductor Physics of the Siberian Branch of the Russian Academy of Sciences.

The dynamical magnetic properties of nanocrystalline Fe films, determining the ferromagnetic resonance (FMR) parameters, was studied in a standard ÉPA-2M spectrometer with frequency $f = 9.2$ GHz. The FMR resonance fields were measured in the entire range of angles between the external field and the film plane in order to calculate the effective magnetization M_{eff} from the equation

$$H_{\perp}^r - 4\pi M_{\mathrm{eff}} = \sqrt{H_{\parallel}^r(H_{\parallel}^r + 4\pi M_{\mathrm{eff}})}, \tag{1}$$

where $H_{\perp}^r$ and $H_{\parallel}^r$ are the FMR fields with the corresponding experimental geometry. The measurements were performed at room temperature.

The static magnetic measurements were performed with an automated vibrating magnetometer with fields up to 20 kOe and temperatures ranging from 4.2 to 250 K. The temperature dependence of the saturation magnetization $M_s(T)$ of nanocrystalline Fe films, measured with external field $H = 20$ kOe in the temperature range 70–210 K is described well by the law

$$M_s(T) = M_{s0}(1 - BT^{3/2}), \tag{2}$$

which made it possible to determine the saturation magnetization and the numerical value of the constant B and to calculate the exchange interaction constant A:

$$A = \frac{k}{8\pi} \left(\frac{g\mu_B}{M_{s0}} \right)^{1/3} \left(\frac{2.612}{B} \right)^{2/3}. \tag{3}$$

The high-temperature dependences of the saturation magnetization $M_s(T)$ were measured on a torsional anisometer in the temperature range from 273 to 750 K with constant field $H = 5.7$ kOe. The Curie temperatures T_c of nanocrystalline Fe were determined by extrapolating the temperature dependence $M_s(T)$ to zero magnetization using the linear dependence of M_s^2 on T near T_c, observed for these materials.

The static magnetic measurements also included measurements of the magnetization curve $M(H)$. The local anisotropy H_a (related with the magnetocrystalline anisotropy constant by the relation $K = H_a \cdot M_s/2$) was calculated from the magnetization curves up to saturation, measured in the film plane at $T = 250$ K.

TABLE I.

	Initial state	$T_{an}=200\,°C$	$T_{an}=400\,°C$	bcc-Fe
M_{s0}, G	1540	1180	1150	1740
M_{eff} (FMR), G	1180	1030	–	1740
T_c, °C	400	300	300	770
A, 10^{-7} ergs/cm	5.5	3.2	3.7	20
H_a, kOe	2.0	5.9	6.1	0.5

In the course of the investigations the initial nanocrystalline Fe films were subjected to thermal annealing. The annealing was performed in a high-vacuum chamber for 1 h at temperatures 200 and 400 °C.

RESULTS AND DISCUSSION

The results of the analysis of the photoelectron spectra showed that the surface of the films of nanocrystalline Fe is oxidized — the line O1S (530.4 eV) due to oxygen and a component attesting to the hydroxyl group (OH^-) are observed in the electronic spectra. The shape of the Fe $2P_{3/2}$ line qualitatively indicates two types of nearest-neighbor environment of the Fe atom. The profile of elements contained in nanocrystalline Fe over the film depth was reconstructed by Auger-electron spectroscopy. The composition of the experimental films was as follows: Fe ($\sim$75 at.%) and C ($\sim$20 at.%) with a uniform distribution of the elements (x_{Fe}/x_C) over the film depth.

The results of the magnetic measurements are presented in Table I. It is evident that the initial metastable state (which we call X_1), realized in films of the alloy Fe(C), is characterized by the following basic magnetic parameters: $A=0.56\cdot10^{-6}$ ergs/cm, M_0 $=1540$ G, $H_a=2$ kOe, $T_c=400\,°C$. As a result of thermal relaxation, the initial state transforms into a different metastable state (which we call X_2) with the magnetic parameters $A=0.3\cdot10^{-6}$ ergs/cm, $M_0=1200$ G, $H_a=6.1$ kOe, and $T_c=300\,°C$.

The large difference in the measured magnetic parameters A, M_0, T_c, and H_a attests to structural differences between the observed metastable states. A transition into the thermodynamically equilibrium bcc-Fe phase occurs after a 1-h anneal at $T=600\,°C$.

The results of x-ray crystallographic analysis performed on the initial Fe films ($\sim$1000 Å thick) and on the annealed Fe films ($T_{an}=200\,°C$) are presented in Fig. 1. The diffraction curve of the initial films, measured in SR (curve *1* in Fig. 1), contained one broadened peak centered near $d=2.04$ Å and $\Delta(2\theta)\approx3°$ wide. Such a diffraction curve indicates a nanocrystalline structure of the initial material with a grain size of the order of 40 Å. However, it is impossible to draw a conclusion about the type of atomic lattice in these nanocrystalline grains on the basis of a single reflection. The annealed films of nanocrystalline Fe were characterized by a diffraction curve (curve *2* in Fig. 1) containing a set of reflections. Five of the reflections with the highest intensities, marked in Fig. 1, attest to a hexagonal close-packed structure (hcp) for these Fe films. (The fact that a complete set of reflections characterizing a polycrystalline hcp structure is lacking attests, in our view, to a certain degree of texture in these films.) Analysis of these reflections gives the following values for the lattice parameters of Fe: $a=2.63$ Å, $c=4.46$ Å, c/a
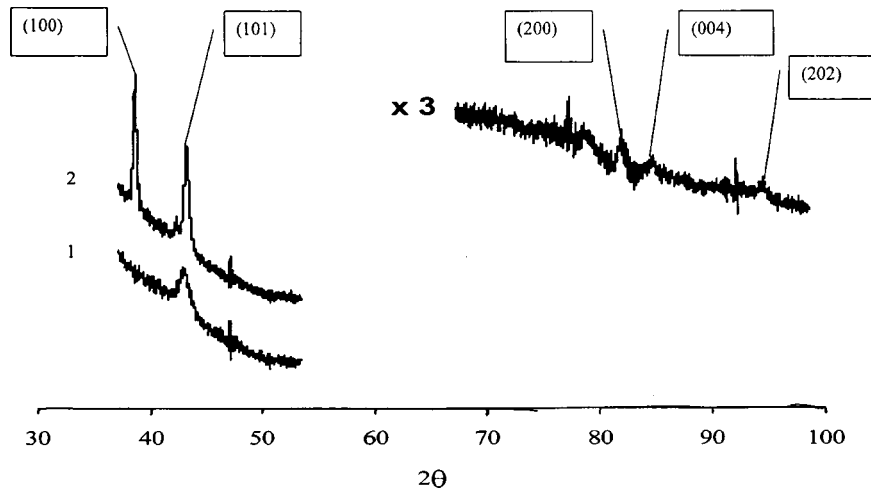
FIG. 1. X-Ray diffraction patterns of the initial nanocrystalline Fe film (1) and a film (2) annealed at T_{an} $=200\,°C$.

$=1.696$. The volume per Fe atom calculated from these parameters is $V_{at}=13\ Å^3$. We note that the computed volume V_{at} per Fe atom in these Fe films is more than 10% greater than the analogous quantity in thermodynamically equilibrium hcp-Fe and is close to the value $V_{at}\approx13\ Å^3$ observed in rapidly quenched metastable alloys hcp-Fe-C.[5]

The results of x-ray diffraction on SR made it possible to identify the atomic structure of the metastable state X_2 and to assert with adequate substantiation that this is hcp-Fe. Structural investigations using a TEM turned out to be most informative for identifying the initial metastable state X_1. The point is that the transition $X_1 \rightarrow X_2$ can be obtained not only by isothermal annealing at $T=200\,°C$, $t=1$ h, but also by irradiation with a beam of electrons in an electron microscope (voltage 150 kV). Under such actions the initial ''x-ray amorphous'' state in the nanocrystalline films transforms into the hcp solid solution Fe(C). This process is virtually instantaneous (several seconds). Careful analysis of the observed transformations in nanocrystalline films of the alloy Fe(C) established that the hcp-Fe reflections arising in the electron diffraction pattern under the action of an electron beam are secondary. Initially, ordering of the initial ''x-ray amorphous'' (nanocrystalline) state occurs. This is indicated by the appearance of reflections against the background of the initial halo. In the course of the further action of the electron beam on the experimental film, reflections of the hcp phase of Fe appear, and reflections of the initial metastable state vanish. We were able to identify the initial metastable phase. This was found to be a state with face-centered cubic packing fcc-Fe. The lattice parameter of this fcc state is $a=3.72\ Å$ and the volume per Fe atom is V_{at} $=13.05\ Å$. Figure 2 shows the diffraction pattern of the initial nanocrystalline state (Fig. 2a) and its transformation under the action of the electron beam. Figure 2b shows the interpretation of the metastable structures that arise. Using the well-known relation Δa $\sim f$ (at. %C), we determined the chemical composition of the fcc solid solution of a microsection from which the diffraction pattern presented in Fig. 2b — $Fe_{82}C_{18}$ was obtained.
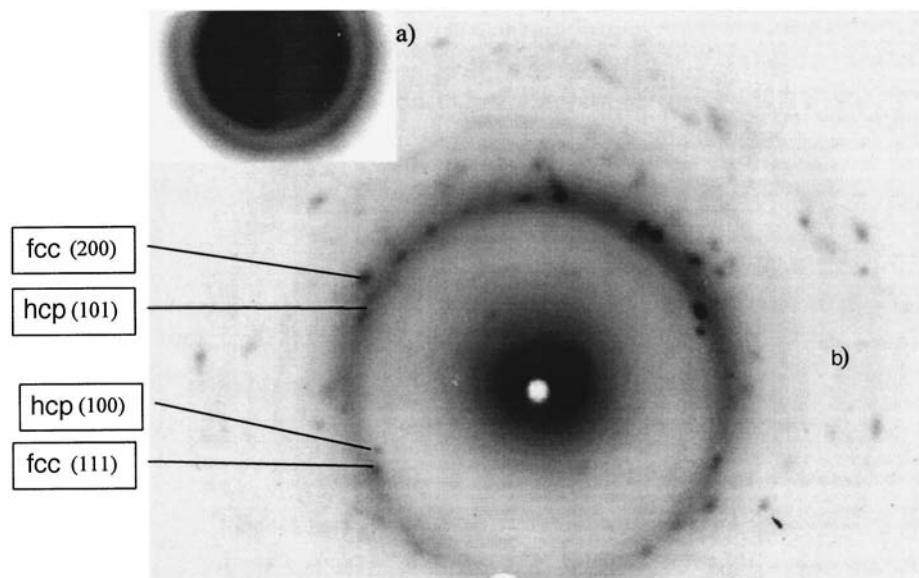
FIG. 2. Electron diffraction patterns of nanocrystalline films Fe(C): a) initial state; b) annealed by an electron beam.

The magnetic order of metastable close-packed phases of iron, fcc and hcp, is determined by the volume per Fe atom. The volume per Fe atom $V_{at} = 11.5 - 12$ Å^3 in this material is critical. When this volume is reached the atoms of the close-packed structures transform from a low- into a high-spin state.[1] Nanocrystalline films of the alloy Fe(C) obtained by PPV are supersaturated solid solutions. The volumes per atom in these structures are $V_{at} \approx 13$ Å^3, which is more than 10% greater than the corresponding volumes per Fe atom in thermodynamically stable close–packed fcc and hcp structures ($V_{at} \approx 11$ Å^3). For this reason, the ferromagnetic (high-spin) state of the metastable Fe phases which we investigated is a natural state.

Thus, the initial metastable fcc phase Fe(C) is characterized by the following magnetic parameters: $A = 0.56 \cdot 10^{-6}$ ergs/cm, $M_0 = 1540$ G, $H_a = 2$ kOe, and $T_c = 400\,°C$. The basic magnetic characteristics of the metastable phase of hcp-Fe(C) — $A = 0.3 \cdot 10^{-6}$ ergs/cm, $M_0 = 1200$ G, $H_a = 6$ kOe, and $T_c = 300\,°C$ — are close to the corresponding values for cubic tight packing. An exception here is the magnetocrystallographic anisotropy field, which is three times greater than H_a in the fcc phase of Fe.

We have shown above, by structural investigations and measurement of the magnetic characteristics, that in a nanocrystalline iron alloy with the carbon structural transformations fcc-Fe(C) → hcp-Fe(C) occur as a result of thermal relaxation. A clear understanding of the sequence of the observed states can be obtained using Ostwald's rule. According to this rule, at a transition from a nonequilibrium into an equilibrium state, the system passes through all possible intermediate metastable states. Figure 3 shows the qualitative room-temperature (G, x) phase diagram of iron, where the Gibbs energy is $G = H - TS$ (H is the enthalpy and S is the entropy) and x is the carbon concentration. Here the order of magnitudes of the transition enthalpies are $\Delta H^{\gamma \to \epsilon} \approx 0.11$ kcal/mole and
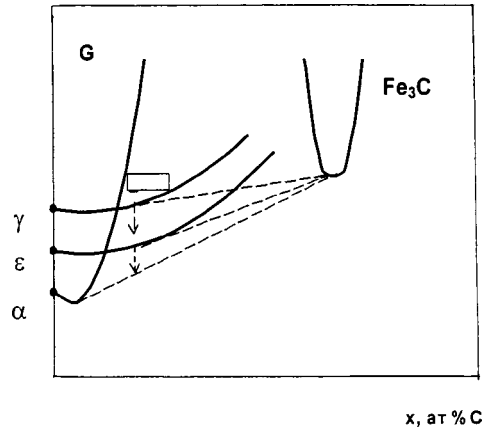
FIG. 3. Qualitative (G,X) phase diagram of iron.

$\Delta H^{\gamma \rightarrow \alpha} = 0.22$ kcal/mole, the stoichiometric compound Fe_3C (cementite) is characterized by a positive formation energy $\Delta H = 5.4$ kcal/mole.[10]

This phase diagram gives an idea of the possible scenarios realized in the metastable system Fe(C). The realization of a particular metastable state will be determined by the initial coordinates (G_0, x_0) in the phase plane or, in other words, the stored excess energy ΔG relative to the stable equilibrium of the mechanical mixture bcc-Fe + graphite. The degree of nonequilibrium ΔG of the Fe(C) condensates obtained is dictated by the technological processes of PPV. In the first place, this method makes it possible to obtain supersaturated solid solutions Fe(C), which increases the elastic energy due to an increase in the interatomic distances; in the second place, the nanocrystalline alloy Fe(C) is characterized by a small grain size (40 Å) and therefore a large energy contribution due to the specific surface area S_n. The contributions enumerated above to the thermodynamic Gibbs potential can be represented as $\Delta G = P\Delta V + \sigma_n S_n$, where P is the internal pressure, ΔV is the change in the molar volume, and σ_n is the surface energy density. According to the experimental results presented above, the initial state of the nanocrystalline alloy Fe(C), obtained by the PPV method, occupies in the (G,x) phase diagram a location indicated by the dashed rectangle. It is evident that under relaxation of the initial state Fe(C), in this case, the following structural transformations should be observed:

fcc-Fe(C) $\rightarrow$ hcp-Fe(C) $\rightarrow$ bcc-Fe+C.

The fcc and hcp solid solutions Fe(C) in the (G,x) phase diagram are shown to be in equilibrium with the stoichiometric carbide Fe_3C. Structural investigations (TEM) of separate sections of nanocrystalline Fe(C) films indicate a negligible presence of cementite. However, the high-temperature investigations of the saturation magnetization $M_s(T)$ of nanocrystalline Fe(C) films did not show the presence of an F_3C phase, characterized by the temperature $T_c = 210\,°C$. Therefore the volume fraction of iron carbide Fe_3C in the experimental Fe(C) metastable films, in all probability, does not exceed 10%.

a)e-mail: rauf@iph.krasnoyarsk.su

———————

[1] W. Keune, T. Ezawa, W. A. A. Macedo *et al.*, Physica B **161**, 269 (1989).

[2] M. Maurer, M. Piecuch, M. F. Ravet *et al.*, J. Magn. Magn. Mater. **93**, 15 (1991).

[3] V. L. Sedov, *Antiferromagnetism of Gamma Iron. The Problem of Invar* (Nauka, Moscow, 1987).

[4] I. S. Miroshnichenko, *Quenching from the Liquid State* (Metallurgiya, Moscow, 1982).

[5] J. M. Dubois and G. Le Caer, Acta Metall. **25**, 609 (1977).

[6] G. I. Frolov, V. S. Zhigalov, V. I. Pol'skiĭ *et al.*, Fiz. Tverd. Tela (St. Petersburg) **38**, 1208 (1996) [Phys. Solid State **38**, 668 (1996)].

[7] V. S. Zhigalov, G. I. Frolov, and L. I. Kveglis, Fiz. Tverd. Tela (St. Petersburg) **40**, 2074 (1998) [Phys. Solid State **40**, 1878 (1998)].

[8] S. M. Zharkov, V. S. Zhigalov, and G. I. Frolov, Fiz. Met. Metalloved. **81**, 170 (1996).

[9] R. S. Iskhakov, S. V. Komogortsev, S. V. Stolyar *et al.*, Fiz. Met. Metalloved. **88**(3) (1999).

[10] *Thermal Constants of Substances*, No. 6 (Nauka, Moscow, 1972).

Translated by M. E. Alferieff

Fluctuations in random *RL−C* networks: nonlinear *σ*-model description

Yan V. Fyodorov*)

Fachbereich Physik, Universität-GH Essen, D-45117 Essen, Germany

Disordered $RL-C$ networks are known to be an adequate model for describing fluctuations of electric fields in a random metal–dielectric composite. We show that under appropriate conditions the statistical properties of such a system can be studied in the framework of Efetov's nonlinear σ model. This fact provides a direct link to the theory of Anderson localization. © *1999 American Institute of Physics.* [S0021-3640(99)00623-4]

PACS numbers: 81.05.Mh, 72.80.Tm, 84.30.Bv, 05.40.−a, 72.15.Rn

The optical properties of random metal–dielectric films (also known as cermets or semicontinuous metal films) have attracted a lot of research interest recently, both theoretical and experimental (see Refs. 1–4 and references therein). It was discovered that for metal concentrations close to the percolation threshold, the absorption of microwave radiation in such materials fluctuates anomalously. In turn, these anomalous properties were traced back to high local field fluctuations detected in such compounds. A very insightful approach to the problem[1-4] is to represent the system as a large random network consisting of capacitances C and inductances L, the latter being in series with a weak resistance R. The network description naturally arises when discretizing the equations satisfied by the scalar potential of the electric field. The capacitors model dielectric bridges, while isolated metallic granules are indeed characterized by an almost purely inductive response for radiation frequencies ω such that $\omega_\tau \ll \omega \lesssim \omega_p$, where ω_p is the plasma frequency and ω_τ is the plasmon relaxation rate.[1-4]

For frequencies close to $\omega_0 = 1/(LC)^{1/2}$ the electromagnetic response of such a network is dominated by resonance effects provided that the losses are small, i.e., the quality factor $Q = (L/C)^{1/2}R^{-1}$ is large. The resonance frequencies can be determined as (generalized) eigenvalues of some linear lattice operator arising when solving the system of Kirchhoff equations $\Sigma_j \sigma_{ij}(v_i - v_j) = 0$ for on-site potentials $v_i \equiv v(\mathbf{r}_i)$.[4,5] Here σ_{ij} is the conductance between a pair of nodes $\mathbf{r}_i$ and $\mathbf{r}_j$ if the two nodes are connected by a direct bond, and $\sigma_{ij} = 0$ otherwise. In the simplest case, one can think of the network as being connected to an ac voltage by two external leads attached to lattice nodes with the coordinates $\mathbf{r}_A$ and $\mathbf{r}_B$, the corresponding potentials being $v_A = e^{-i\omega t}$ and $v_B = 0$, respectively. Omitting the common time-dependent factor, it is easy to see that the amplitude of the potential $v(\mathbf{r_i})$ at an internal lattice node $\mathbf{r}_i$ is given by

$$v(\mathbf{r_i}) = \sum_j \ (\hat{D}^{-1})_{ij}\sigma_{Aj}, \tag{1}$$

$$\hat{D}_{ij} = \left(\sigma_{Ai} + \sigma_{Bi} + \sum_{j\neq i} \ \sigma_{ij} \right)\delta_{ij} - (1-\delta_{ij})\sigma_{ij}.$$

In a random $RL-C$ network each nonzero conductance σ_{ij} at frequency $f=\omega/2\pi$ is equal to either $\sigma_0 = iC\omega$ or $\sigma_1 = (R+iL\omega)^{-1}$, with specified probabilities (in what follows we concentrate on the case of equal probabilities of finding L and C bonds in the network). Then it is convenient to introduce ''symmetric'' variables h_{ij} such that $h_{ij} = -1$ if $\sigma_{ij} = \sigma_0$ and $h_{ij} = 1$ if $\sigma_{ij} = \sigma_1$, so that $\sigma_{ij} = e_{ij}\frac{1}{2}([\sigma_0 + \sigma_1] + [\sigma_1 - \sigma_0]h_{ij})$, with $e_{ij} = 1$ for directly connected nodes and $e_{ij} = 0$ otherwise. In terms of these variables we can write $D = \hat{H} - \lambda\hat{W}$, where

$$\hat{W}_{ij} = (Z+e_{Ai}+e_{Bi})\delta_{ij} - (1-\delta_{ij})e_{ij}, \tag{2}$$

$$\hat{H}_{ij} = \left(\tilde{h}_{Ai} + \tilde{h}_{Bi} + \sum_{k\neq i} \tilde{h}_{ik} \right)\delta_{ij} - (1-\delta_{ij})\tilde{h}_{ij}, \tag{3}$$

with $Z = \Sigma_j e_{ij}$ standing for the coordination number of the lattice and $\tilde{h}_{ij} = h_{ij}e_{ij}$. The frequency-dependent parameter λ is defined as

$$\lambda = \frac{\sigma_0 + \sigma_1}{\sigma_0 - \sigma_1} \approx \left(\frac{\omega}{\omega_0} - 1 \right) - \frac{i}{2Q} \equiv \text{Re}\lambda - i\frac{\Gamma}{2}, \tag{4}$$

where we have made use of $\omega \approx \omega_0$ and $Q \gg 1$.

We see that the statistics of the scalar potential $v(\mathbf{r})$ (and hence of the electric field $\mathcal{E}_{ij}$, proportional to the voltage difference $v(\mathbf{r}_i) - v(\mathbf{r}_j)$ across the bond ij) is determined basically by the properties of the operator $\hat{H}$. In Ref. 1 it was suggested that operators of this type acting on a lattice be called Kirchhoff Hamiltonians (KHs). The off-diagonal elements of such a Hamiltonian assume random values ± 1 for directly connected nodes. This property makes the KH similar, in a sense, to a tight-binding Hamiltonian describing the motion of a quantum particle on a disordered lattice with an off-diagonal disorder. The latter model is a paradigmatic one in the theory of Anderson localization. That kind of analogy, first discussed in Ref. 1, led the authors to relate the anomalous fluctuations of the electric fields to localized properties of the corresponding eigenfunctions. Further numerical and experimental work confirmed the quantitative validity of the proposed picture.

At the same time, the extent to which the analogy between the Anderson model and the KH can be carried is a far from trivial question. Indeed, the KH has a specific feature: the diagonal elements H_{ii} are strongly correlated with the off-diagonal elements $H_{i\neq j}$. It is known that correlations of various kinds can substantially modify the localization behavior (see, e.g., Ref. 6). Therefore, it is highly desirable to find a realistic approach that will shed more light on the question of equivalence between the models.

The main goal of this paper is to show that the equivalence indeed exists, and the unifying concept is provided by the so-called Efetov supermatrix nonlinear σ model (ENSM).[7] The latter model is known to be the most powerful tool in understanding

fluctuation phenomena in disordered conductors in the last decade (see, e.g., Ref. 8). As a matter of fact, we derive the ENSM from a version of the KH and thus lay a regular analytical groundwork for the quantitative description of the statistical properties of semicontinuous films.

To derive the ENSM from a microscopic random Hamiltonian one has to exploit some large parameter which physically controls the strength of the disorder. Experience in dealing with the usual tight-binding models suggests that the role of such a parameter can be played, e.g., by a large radius of connectivity b (i.e., a large coordination number $Z \sim b^d$).[9,10] Formally, we consider a d-dimensional lattice of linear size L with unit lattice spacing and a connectivity radius b. To facilitate bookkeeping of terms of different orders it is convenient make the redefinition $e_{ij} \to e_{ij} Z^{-1/2}$, where $e_{ij} = 1$ for $|\mathbf{r}_i - \mathbf{r}_j| \leq b$ and $e_{ij} = 0$ otherwise. The radius of connectivity b is chosen to satisfy $1 \ll b \ll L$. Both inequalities are important: $b \gg 1$ allows one to map the problem to the ENSM, while $b \ll L$ is necessary to ensure the adequate description of Anderson localization effects. Indeed, it has been shown recently[5] that a full-connectivity LC network with $b = L$ can be mapped on the zero-dimensional version of the ENSM, which precludes taking localization effects into account.

To demonstrate the mapping it is instructive to address the simplest nontrivial correlation function of the potentials: $C_i(\Omega, \Gamma) = \langle v_{\omega_1}^*(\mathbf{r}_i) v_{\omega_2}(\mathbf{r}_i) \rangle$, where we have introduced the frequency difference $\Omega \propto (\omega_1 - \omega_2)/2\omega_0 \ll 1$, and the brackets stand for the disorder averaging.[1)]

Our starting expression is:

$$C_i(\Omega, \Gamma) = \left\langle \sum_{k_1, k_2} e_{A k_1} e_{A k_2} (\tilde{h}_{A k_1} - \lambda_1^*)(\tilde{h}_{A k_2} - \lambda_2) \left[\frac{1}{H - \lambda_1 W} \right]_{i k_1}^* \left[\frac{1}{H - \lambda_2 W} \right]_{i k_2} \right\rangle. \quad (5)$$

To perform the disorder averaging we follow the standard procedure and represent the matrix element of the resolvent $(H - \lambda W)^{-1}$ in terms of the Gaussian integral

$$\left[\frac{1}{H - (\operatorname{Re}\lambda \pm i\Gamma/2)W} \right]_{ik} = \pm i \int \left[\prod_{l=1}^N d\Psi_l(\pm) \right] s_i^*(\pm) s_k(\pm) \exp\left\{ \pm \frac{i}{2} \sum_{m,n}^N \Psi_m^\dagger(\pm) \right.$$

$$\left. \times [W_{mn}(\operatorname{Re}\lambda \pm i\Gamma/2) - H_{mn}] \Psi_n(\pm) \right\} \quad (6)$$

over 4-component supervectors $\Psi_l(\pm)$,

$$\Psi_l(\pm) = \begin{pmatrix} \mathbf{S}_l(\pm) \\ \boldsymbol{\eta}_l(\pm) \end{pmatrix}, \quad \mathbf{S}_l(\pm) = \begin{pmatrix} s_l(\pm) \\ s_l^*(\pm) \end{pmatrix},$$

$$\boldsymbol{\eta}_l(\pm) = \begin{pmatrix} \chi_l(\pm) \\ \chi_l^*(\pm) \end{pmatrix}, \quad d\Psi_l = \frac{ds_l ds_l^*}{2\pi} d\chi_l^* d\chi_l, \quad (7)$$

where the components $s_l(+), s_l(-), l = 1, 2, \ldots, N$ are complex commuting variables, and $\chi_l(+), \chi_l(-)$ form the corresponding Grassmannian parts of the supervectors $\Psi_l(\pm)$.

To facilitate the presentation, it is appropriate to anticipate few facts whose validity can be verified by the same method as presented below. First of all, after averaging, the double sum in expression (5) is dominated in the limit $1 \ll b \ll L$ by the diagonal terms with indices $k_1 = k_2$. Another fact which is useful to exploit from the very beginning is that all the resonance frequencies are concentrated in an interval of the order of $\delta\omega/\omega_0 \sim Z^{-1/2}$ around $\omega = \omega_0$, so that the typical spacing Δ between the neighboring resonances is of the order of $\Delta \sim \omega_0/(NZ^{1/2})$, with $N \sim L^d$ being the total number of resonance frequencies. We anticipate nontrivial correlations occurring on a frequency scale $\omega_1 - \omega_2 \sim \Delta$ (Ref. 5). For this reason we scale $\mathrm{Re}\lambda_{1,2} = (r \pm \Omega/2N)/Z^{1/2}$, considering both r and Ω to be of the order of unity. By the same reasoning we consider the losses to be small enough to ensure that $\gamma = \Gamma(NZ^{1/2})$ is of the order of unity. Physically this requirement means that a typical resonance width $\omega_0\Gamma$ is assumed to be comparable to the typical resonance spacing Δ.

With these facts in mind, we can easily average the products of the resolvents over $\tilde{h}_{ij} = \pm 1/Z^{1/2} e_{ij}$ in the limit $N \gg Z \gg 1$. All further steps follow the method used in Ref. 5 (cf. Refs. 10 and 11) adapted to the present model. We have:

$$C_i(\Omega,\gamma) = \frac{1}{Z} \sum_k e_{Ak} \int \left[\prod_l d\Phi_l \right] s_i^*(-)s_i(+)s_k^*(+)s_k(-) \exp\left\{ \frac{i}{4NZ}(\Omega + i\gamma) \right.$$

$$\left. \times \sum_{m<n} e_{mn}(\Phi_m^\dagger - \Phi_n^\dagger)(\Phi_m - \Phi_n) \right\} \exp\left\{ -\frac{1}{16Z} \sum_{m,n} e_{mn}\mathcal{K}(\Phi_m,\Phi_n) \right\}. \quad (8)$$

Here the integration goes over the 8-component supervectors $\Phi_l^\dagger = (\Psi_l^\dagger(+),\Psi_l^\dagger(-))$ and

$$\mathcal{K}(\Phi_a,\Phi_b) = -4ir(\Phi_a^\dagger - \Phi_b^\dagger)\hat{\Lambda}(\Phi_a - \Phi_b) + [(\Phi_a^\dagger - \Phi_b^\dagger)\hat{\Lambda}(\Phi_a - \Phi_b)]^2 \quad (9)$$

with $\hat{\Lambda} = \mathrm{diag}(1,1,1,1,-1,-1,-1,-1)$. Only those terms are left in the exponent which will later on contribute to the final expressions in the limit under discussion.

The next step is to use the following Hubbard–Stratonovich functional transformation (cf. Refs. 10,11, and 5):

$$\exp\left\{ -\frac{1}{16Z} \sum_{m,n} e_{mn}\mathcal{K}(\Phi_m,\Phi_n) \right\}$$

$$= \int \mathcal{D}(g) \exp\left\{ \frac{i}{8} \sum_{m=1}^{N} g_m(\Phi_m) \right\} \exp\left\{ -\frac{Z}{16} \sum_{mn} [\hat{e}^{-1}]_{mn} \right.$$

$$\left. \times \int d\Phi_a d\Phi_b g_m(\Phi_a)\mathcal{C}(\Phi_a,\Phi_b)g_n(\Phi_b) \right\},$$

where $[\hat{e}^{-1}]$ is the matrix inverse to the matrix $\hat{e} = [e_{ij}]|_{i,j=1,\ldots,N}$, and the kernel $\mathcal{C}(\Phi_a,\Phi_b)$ is, in a sense, the inverse of the (symmetric) kernel $\mathcal{K}(\Phi_a,\Phi_b)$:

$$\int d\Phi \mathcal{K}(\Phi_a,\Phi)\mathcal{C}(\Phi,\Phi_b) = \delta(\Phi_a,\Phi_b), \quad (10)$$

with $\delta(\Phi_a,\Phi_b)$ playing the role of a δ-functional kernel in a space spanned by the functions $g(\Phi)$.

With the help of these relations one easily brings each term of the sum in Eq. (8) to the form:

$$\int \mathcal{D}(g)\mathcal{F}_{+,-}[g_i]\mathcal{F}_{-,+}[g_k]\exp[\mathcal{L}\{g\}+\delta\mathcal{L}_1\{g\}], \tag{11}$$

where

$$\mathcal{F}_{\pm,\mp}[g]=\frac{\int d\Phi\, s^*(\pm)s(\mp)\exp\left\{\frac{i}{8}g(\Phi)\right\}}{\int d\Phi\, \exp\left\{\frac{i}{8}g(\Phi)\right\}}, \tag{12}$$

$$\mathcal{L}\{g\}=\sum_m \ln\int d\Phi\, \exp\left\{\frac{i}{8}g_m(\Phi)\right\}$$

$$-\frac{Z}{16}\sum_{m,n}[e^{-1}]_{mn}\int d\Phi_a d\Phi_b g_m(\Phi_a)\mathcal{C}(\Phi_a,\Phi_b)g_n(\Phi_b), \tag{13}$$

$$\delta\mathcal{L}_1\{g\}=i\frac{(\Omega+i\gamma)}{4NZ}$$

$$\times\sum_{m<n}e_{mn}\frac{\int d\Phi_m d\Phi_n \exp\left\{\frac{i}{8}[g_m(\Phi_m)+g_n(\Phi_n)]\right\}(\Phi_m^\dagger-\Phi_n^\dagger)(\Phi_m-\Phi_n)}{\int d\Phi_m d\Phi_n \exp\left\{\frac{i}{8}[g_m(\Phi_m)+g_n(\Phi_n)]\right\}} \tag{14}$$

and we have restricted ourselves by the leading-order term in $\delta\mathcal{L}_1\{g\}$, which is only a small correction to $\mathcal{L}\{g\}$.

The next step is to evaluate the functional integral over $g(\Phi)$ by the saddle-point method, which is justified by two large parameters: Z and N. The saddle-point configuration $g_m^{(s)}(\Phi)$ can be found by requiring a vanishing variation of the "action" $\mathcal{L}\{g\}$ and satisfies the following system of equations:

$$Z\sum_n[e^{-1}]_{mn}g_n^{(s)}(\Phi_a)=i\frac{\int d\Phi_b \mathcal{K}(\Phi_a,\Phi_b)\exp\left\{\frac{i}{8}g_m^{(s)}(\Phi_b)\right\}}{\int d\Phi_b \exp\left\{\frac{i}{8}g_m^{(s)}(\Phi_b)\right\}}. \tag{15}$$

In deriving Eq. (16) we have used Eq. (11).

Given the form of the kernel (9) and making use of the fact that $Z\sum_n[e^{-1}]_{mn}=1$, one can find a space-independent solution $g_n^{(s)}(\Phi)\equiv g^{(s)}(\Phi)$ to equation Eq. (16):

$$g^{(s)}(\Phi_a)=4(r-G_1)(\Phi_a^\dagger\hat{\Lambda}\Phi_a)+4iG_2(\Phi_a^\dagger\Phi_a)+i(\Phi_a^\dagger\hat{\Lambda}\Phi_a)^2 \tag{16}$$

provided that the real coefficients G_1,G_2 are solutions of the system of two conjugate equations:

$$G_2 \pm iG_1 = \int_0^\infty du \, \exp\left\{ \pm \frac{i}{2} u(r - G_1 \pm iG_2) - \frac{u^2}{8} \right\}. \tag{17}$$

Hints for verifying such a solution can be found in Ref. 5.

For further analysis it is very important that a solution to equations (18), such that $G_2(r) > 0$, exists for arbitrary $-\infty < r < \infty$. Actually, the mean density of resonances is merely given by $\rho(r) = \frac{1}{\pi} G_2(r)$ (Ref. 5).

The most important consequence of the existence of the solution $g^{(s)}(\Phi_a)$ in the form (16) with $G_2 \neq 0$ is actually the simultaneous existence of a whole *continuous manifold* of saddle points parametrized as

$$g_T(\Phi_a) = g^{(s)}(\hat{T}\Phi_a), \quad \hat{T}^\dagger \hat{\Lambda} \hat{T} = \hat{\Lambda}. \tag{18}$$

If it hadn't been for the condition $G_2 \neq 0$ all these solutions would trivially coincide: $g_T(\Phi) \equiv g^{(s)}(\Phi)$ for any $\hat{T}$ defined as above. In the actual case the presence of the combination $\Phi_a^\dagger \Phi_a$ which is *not* invariant with respect to a transformation $\Phi_a \rightarrow \hat{T}\Phi_a$ ensures the existence of the aforementioned manifold. This fact is just a particular manifestation of the phenomenon of spontaneous symmetry breaking. Different nontrivial solutions are actually parametrized by the supermatrices $\hat{T}$ which are elements of a graded coset space $UOSP(2,2/4)/UOSP(2/2) \otimes UOSP(2/2)$.

As a result, the functional integral over $g_m(\Phi)$ is dominated by ''Goldstone modes'' which are slowly changing in space and parametrized as $g_m^{(G)}(\Phi) = g^{(s)}(\hat{T}_m\Phi)$, with matrices $\hat{T}_m$ which depend on the lattice site index $m = 1, \ldots, N$. Our next step is to determine the effective action for these modes, that is $\mathcal{L}\{g_m^{(G)}\} + \delta \mathcal{L}_1\{g_m^{(G)}\}$.

First of all we notice that

$$\int d\Phi \, \exp\left\{ \frac{i}{8} g_m^{(G)}(\Phi) \right\} = 1,$$

which allows one to perform the following manipulations:

$$\int d\Phi_a d\Phi_b g_m^{(G)}(\Phi_a) \mathcal{C}(\Phi_a, \Phi_b) g_n^{(G)}(\Phi_b)$$

$$= i \int d\Phi \, g_n^{(G)}(\Phi) \exp\left\{ \frac{i}{8} g_m^{(G)}(\Phi) \right\} = i \int d\Phi \, g^{(s)}(\hat{T}_n \hat{T}_m^{-1} \Phi) \exp\left\{ \frac{i}{8} g^{(s)}(\Phi) \right\}$$

$$= -4 G_2^2 \text{Str}(\hat{T}_n \hat{T}_m^{-1} \hat{\Lambda} (\hat{T}_n \hat{T}_m^{-1})^{-1} \hat{\Lambda}) = -4(\pi\rho)^2 \text{Str}(\hat{T}_m^{-1} \hat{\Lambda} \hat{T}_m \hat{T}_n^{-1} \hat{\Lambda} \hat{T}_n). \tag{19}$$

Here we have first exploited the saddle-point equation (16) together with Eq. (11) and then performed a change of variables: $\hat{T}_m\Phi \rightarrow \Phi$, which does not effect the measure $d\Phi$ because of the (pseudo) unitarity of the matrices $\hat{T}$. Then the integral can be readily evaluated with help of the explicit form in Eq. (17) (see, e.g., examples of similar calculations in Refs. 5 and 11) and brought to the final form by employing the cyclic permutation and the aforementioned relation between G_2 and the density of resonances $\rho(r)$. In the very same way we also find:

$$\delta\mathcal{L}_1\{g\} = \frac{(\Omega+i\gamma)}{4NZ} G_2 \sum_{m<n} e_{mn} \text{Str}(\hat{T}_m^{-1}\hat{\Lambda}\hat{T}_m\hat{\Lambda} + \hat{T}_n^{-1}\hat{\Lambda}\hat{T}_n\hat{\Lambda})$$

$$= \pi\rho(\Omega+i\gamma)\frac{1}{4N} \sum_m \text{Str}(\hat{T}_m^{-1}\hat{\Lambda}\hat{T}_m\hat{\Lambda}). \tag{20}$$

The pre-exponential factors $\mathcal{F}_{+,-}[g_i]$ are calculated analogously and are given by

$$\mathcal{F}_{+,-}[g_i] = \pi\rho[\hat{T}_i^{-1}\hat{\Lambda}\hat{T}_i]^{2,5}; \quad \mathcal{F}_{-,+}[g_k] = \pi\rho[\hat{T}_k^{-1}\hat{\Lambda}\hat{T}_k]^{6,1},$$

where the indices of the supermatrix elements are inherited from the structure of the diadic product $\Phi\otimes\Phi^\dagger$.

We see that calculating the correlation function (8) in the limit $L\gg b\gg 1$ amounts to evaluating the following integral over the set of supermatrices $\hat{Q}_m = \hat{T}_m^{-1}\hat{\Lambda}\hat{T}_m$:

$$C_i = \frac{(\pi\rho)^2}{Z} \sum_k e_{Ak} \int \left[\prod_{l=1}^{N} d\hat{Q}_l\right] Q_i^{2,5} Q_k^{6,1} e^{\mathcal{L}(\hat{Q})}, \tag{21}$$

$$\mathcal{L}(\hat{Q}) = \frac{Z(\pi\rho)^2}{4} \sum_{m,n=1}^{N} [e^{-1}]_{mn} \text{Str}\hat{Q}_m\hat{Q}_n + i\frac{\pi\rho(\Omega+i\gamma)}{4N} \sum_{m=1}^{N} \text{Str}(\hat{Q}_m\hat{\Lambda}). \tag{22}$$

The action in Eq. (23) is actually equivalent to the discretized version of the super-matrix nonlinear σ model, well-studied in the context of Anderson localization.[7,8] Indeed, following Ref. 9, we note that the condition $b\gg 1$ ensures slow variation of the matrices $\hat{Q}_m$ with index m, so that it is legitimate to pass from the lattice to the continuum, whereupon the action assumes the standard form:

$$\mathcal{L}(\hat{Q}) = \frac{\pi\rho}{8} \int d\mathbf{r}\,\text{Str}\left[D(\nabla\hat{Q})^2 + 2i\frac{(\Omega+i\gamma)}{V}\hat{Q}(\mathbf{r})\hat{\Lambda}\right], \tag{23}$$

where $D = \pi\rho Z^{-1}\Sigma_{|\mathbf{r}|<b}\mathbf{r}^2$ plays the role of the effective diffusion constant, and $V = \int d\mathbf{r}$. The large value of $D \propto b^2$ ensures that the typical spatial scale ξ of variation of $\hat{Q}(\mathbf{r})$ is large: $\xi \propto b^2$. Thus over distances of the order of b the matrices $\hat{Q}$ do not change, and therefore

$$C_i = (\pi\rho)^2 \int \mathcal{D}\hat{Q}(\mathbf{r}) Q^{2,5}(\mathbf{r}_i) Q^{6,1}(\mathbf{r}_A) e^{\mathcal{L}(\hat{Q})}. \tag{24}$$

In conclusion, we have managed to express the correlation function of the scalar potentials in terms of the ENSM. A similar reduction is also possible for other quantities of interest. As is well known,[7,8] explicit evaluation of integrals of the type in Eq. (25) depends crucially on the parameter $g = 2\pi\rho DL^{d-2}$. For $g\to\infty$ the integral is dominated by the constant configuration: $\hat{Q}(\mathbf{r}) = \hat{Q}_0$, and the result for Eq. (25) is very simple: $\tilde{C}_i = 2i\pi\rho(r)/(\Omega+i\gamma)$. This is the so-called "zero-dimensional" limit, corresponding to the infinite-range connectivity model.[5] One can take into account weak localization effects, finding $1/g$ corrections in any dimension d (see, e.g., Ref. 8). For a quasi-one-dimensional lattice one can calculate the integrals exactly in the limit $\Omega, \eta\to 0$ (Ref. 9). One should be able also to study the singular parts of higher correlation functions. These questions are left for further investigations.

---

*) On leave from Petersburg Nuclear Physics Institute, 188350 Gatchina, Russia.

1) Actually, the lowest correlation function of the electric fields $\mathcal{E}_{ij}(\omega) = v_\omega(\mathbf{r}_i) - v_\omega(\mathbf{r}_j)$ amounts to the local correlations of the scalar potential, since, in fact, in the present model $\langle v^*(\mathbf{r}_i) v(\mathbf{r}_i) \rangle \gg \langle v^*(\mathbf{r}_i) v(\mathbf{r}_j) \rangle$ for any $i \neq j$.

---

[1] S. Gresillon *et al.*, Phys. Rev. Lett. **82**, 4520 (1999); A. K. Sarychev and V. M. Shalaev, Physica A **266**, 115 (1999); L. Zekri *et al.*, http://xxx.lanl.gov/abs/cond-mat/9908487.

[2] F. Brouers *et al.*, Physica A **241**, 146 (1997); Phys. Rev. B **55**, 13234 (1997); Y. Yagil *et al.*, Phys. Rev. B **46**, 2503 (1991).

[3] M. V. Entin, Zh. Éksp. Teor. Fiz. **114**, 669 (1998) [JETP **87**, 365 (1998)]; E. M. Baskin *et al.*, Physica A **242**, 49 (1997).

[4] J. P. Clerk *et al.*, Adv. Phys. **39**, 191 (1990); J. Phys. A: Math. Gen. **29**, 4781 (1996); Th. Jonckheere and J. M. Luck, J. Phys. A: Math. Gen. **31**, 3687 (1998).

[5] Y. V. Fyodorov, J. Phys. A **32**, 7429 (1999).

[6] I. M. Izrailev and A. A. Krokhin, Phys. Rev. Lett. **82**, 4062 (1999); M. Janssen, unpublished.

[7] K. B. Efetov, *Supersymmetry in Disorder and Chaos*, Cambridge University Press, Cambridge–New York (1997).

[8] A. D. Mirlin, http://xxx.lanl.gov/abs/cond-mat/9907126.

[9] Y. V. Fyodorov and A. D. Mirlin, Phys. Rev. Lett. **67**, 2405 (1991); Int. J. Mod. Phys. **8**, 3795 (1994).

[10] Y. V. Fyodorov *et al.*, J. Phys. I France **2**, 1571 (1992).

[11] A. D. Mirlin and Y. V. Fyodorov, J. Phys. A **24**, 2273 (1991); Y. V. Fyodorov and H.-J. Sommers, Z. Phys. B: Condens. Matter **99**, 123 (1995).

Variational procedure and generalized Lanczos recursion for small-amplitude classical oscillations

E. V. Tsiper

Department of Physics, SUNY at Stony Brook, Stony Brook, NY 11794, USA

A variational procedure is developed which yields the lowest frequencies of small-amplitude oscillations of classical Hamiltonian systems. The genuine Lanczos recursion is generalized to treat related non-Hermitian eigenvalue problems. © *1999 American Institute of Physics.* [S0021-3640(99)00723-9]

PACS numbers: 45.20.Jj, 02.60.−x

The normal modes ξ and frequencies ω of small oscillations of a classical system about equilibrium are determined by the secular equation[1]

$$\omega^2 M\xi = K\xi, \tag{1}$$

where M and K are $N \times N$ symmetric positive-definite matrices of the mass coefficients and spring constants, respectively. In many applications the number N of degrees of freedom is large, while only a few lowest frequencies are of interest.[2] Equation (1) represents a problem more complex than a regular symmetric eigenvalue problem, unless M or K is diagonal.

Equation (1) can be transformed into Hamiltonian form by introducing the canonical momentum $\eta = \omega M\xi$:

$$K\xi = \omega\eta, \quad T\eta = \omega\xi, \tag{2}$$

where $T = M^{-1}$. Thus the frequencies of the normal modes are the eigenvalues of a $2N \times 2N$ matrix

$$\begin{pmatrix} 0 & T \\ K & 0 \end{pmatrix}. \tag{3}$$

The spectrum of this matrix consists of pairs $\pm\omega$, since $(\xi, -\eta)$ is also a solution of (2) that corresponds to $-\omega$. The lowest frequency $\omega_{\min}$ is the lowest *positive* eigenvalue of the matrix (3).

Although the eigenvalues of the matrix (3) are always real, the matrix itself is non-Hermitian, unless $K = T$. Therefore, its diagonalization poses a formidable task. The major problem is that no general minimum principle exists that yields eigenvalues of

751

arbitrary diagonalizable non-Hermitian matrices. This precludes the formulation of a variational procedure similar to the Rayleigh–Ritz procedure for Hermitian matrices. If $K = T$, the matrix (3) is Hermitian, and its positive eigenvalues coincide with those of K and T.

As is known from quantum mechanics, the lowest eigenvalue ϵ_{min} of a Hermitian matrix H can be obtained from the minimum principle

$$\epsilon_{min} = \min_{\{\psi\}} \frac{(\psi H \psi)}{(\psi \psi)}. \tag{4}$$

The minimum is to be sought over all vectors ψ. The Ritz variational procedure is an approximation when the set $\{\psi\}$ in (4) is restricted to some subspace $\mathcal{K}$ of dimension $n < N$. The best approximation to ϵ_{min} in the sense of (4) is obtained as the lowest eigenvalue of the $n \times n$ Rayleigh matrix $\tilde{H}$, obtained by projection of H onto $\mathcal{K}$.

The special paired structure of the matrix (3) makes it possible to generalize (4) so as to yield ω_{min}. In fact,

$$\omega_{min} = \min_{\{\xi, \eta\}} \frac{(\xi K \xi) + (\eta T \eta)}{2 |(\xi \eta)|}. \tag{5}$$

The minimum is to be sought over all possible phase space configurations $\{\xi, \eta\}$. Before providing the proof to this equation, let me point out some of its features.

First, it states that ω_{min} is the minimum arithmetic mean of $(\xi K \xi)$ and $(\eta T \eta)$ over all pairs of vectors ξ, η with scalar product $(\xi \eta) = 1$. Since K and T are both positive-definite, the right-hand side is strictly positive and so is ω_{min}. Second, Eq. (5) is symmetric in K and T, according to the nature of the problem. When $K = T$ the minimum is achieved at $\xi = \eta$, and (5) becomes the same as (4).

Note that the functional in (5) has no maximum, since the denominator can be made arbitrarily small. A global minimum, however, always exists. This is not obvious, since the set of all pairs of vectors with $(\xi \eta) = 1$ is not compact. Indeed, say, any vector orthogonal to η can be added to ξ, making $|\xi|$ arbitrarily large. However, the functional in (5) grows indefinitely in this case, so that the global minimum is achieved at finite $|\xi|$ and $|\eta|$.

Variation of (5) with respect to ξ and η yields Eq. (2). Thus the solutions of (2) are the stationary points of (5). The global minimum (5), therefore, indeed gives ω_{min}. The singularity in the denominator poses no problem, since it corresponds to infinitely large values of the functional, while near the minimum it is analytic.

The minimum principle (5) can, in fact, be obtained from the Thouless minimum principle,[3] derived for non-Hermitian matrices that appear in the random phase approximation (RPA). Equation (5) is transformed into the Thouless minimum principle by the following substitution: $A = (K + T)/2$, $B = (K - T)/2$, $x = (\xi + \eta)/2$, and $y = (\xi - \eta)/2$.

A variational procedure similar to the Rayleigh–Ritz procedure can be formulated if the coordinates ξ and momenta η in (5) are restricted to some subspaces $\mathcal{U}$ and $\mathcal{V}$ of dimension n, respectively.

Let $\{\xi_i\}$ and $\{\eta_i\}$ be two sets of vectors that span $\mathcal{U}$ and $\mathcal{V}$, such that $(\xi_i \eta_j) = \delta_{ij}$. Expanding $\xi = \Sigma u_i \xi_i$, $\eta = \Sigma v_i \eta_i$ and varying (5) with respect to u_i and v_i, we find the latter to obey a $2n \times 2n$ eigenvalue equation

$$\begin{pmatrix} 0 & \tilde{T} \\ \tilde{K} & 0 \end{pmatrix} \begin{pmatrix} u \\ v \end{pmatrix} = \tilde{\omega} \begin{pmatrix} u \\ v \end{pmatrix}, \tag{6}$$

with $\tilde{K}_{ij} = (\xi_i K \xi_j)$ and $\tilde{T}_{ij} = (\eta_i T \eta_j)$. Equation (6) generalizes the Hermitian Rayleigh–Ritz eigenvalue equation for $\tilde{H}$. It has $2n$ solutions $\pm \tilde{\omega}$, the lowest positive one of which gives the best approximation to $\omega_{\min}$ in the sense of Eq. (5).

The Krylov subspace[2] for the matrix (3) can be constructed by operating with it many times on an arbitrary vector (ξ_1, η_1):

$$\begin{pmatrix} \xi_1 \\ \eta_1 \end{pmatrix}, \quad \begin{pmatrix} T\eta_1 \\ K\xi_1 \end{pmatrix}, \quad \begin{pmatrix} TK\xi_1 \\ KT\eta_1 \end{pmatrix}, \quad \cdots . \tag{7}$$

The subspace that spans the first n vectors of this sequence has the property of approximating an invariant subspace of (3). Thus it is natural to expand the approximation to an eigenvector of (3) as a linear combination of these vectors. In other words, the natural choice for the subspaces $\mathcal{U}$ and $\mathcal{V}$ for the variational procedure described above are the subspaces $\mathcal{U}_n$ and $\mathcal{V}_n$ that span the upper and lower components of first n vectors of (7).

In order to implement the variational procedure, it is necessary to construct a biorthogonal basis $\{\xi_i, \eta_i\}$, $i = 1, \ldots, n$ in $\mathcal{U}_n$ and $\mathcal{V}_n$ and compute matrix elements of $\tilde{K}$ and $\tilde{T}$. Both tasks can be performed simultaneously using the following recursion:

$$\xi_{i+1} = \beta_{i+1}^{-1}(T\eta_i - \alpha_i \xi_i - \beta_i \xi_{i-1}) \tag{8a}$$

$$\eta_{i+1} = \delta_{i+1}^{-1}(K\xi_i - \gamma_i \eta_i - \delta_i \eta_{i-1}). \tag{8b}$$

The four coefficients α_i, β_i, γ_i, and δ_i are to be chosen at each step i so as to make ξ_{i+1} orthogonal to η_i and η_{i-1} and to make η_{i+1} orthogonal to ξ_i and ξ_{i-1}. This appears to be enough to ensure global biorthogonality $(\xi_i \eta_j) = \delta_{ij}$.

Indeed, assume biorthogonality to hold up to step i. Multiplying (8a) by η_j, $j < i - 1$, we have $(\eta_j \xi_{i+1}) \propto (\eta_j T \eta_i) = (\eta_i T \eta_j) = 0$ due to the Hermiticity of T and the fact that $T\eta_j$ is a linear combination of all ξ_k with $k \le j+1 < i$. Thus, the biorthogonality also holds for the step $i+1$.

Multiplying (8a) by η_{i-1}, η_i, and η_{i+1} and using biorthogonality, we get $(\xi_i \eta_i) = 1$, $\tilde{K}_{ii} = \alpha_i$, and $\tilde{K}_{i,i-1} = \tilde{K}_{i-1,i} = \beta_i$. Similarly, $\tilde{T}_{ii} = \gamma_i$ and $\tilde{T}_{i,i-1} = \tilde{T}_{i-1,i} = \delta_i$. All other matrix elements of $\tilde{K}$ and $\tilde{T}$ vanish.

The recursion (8) is a straightforward generalization of the Hermitian Lanczos recursion[2,4]

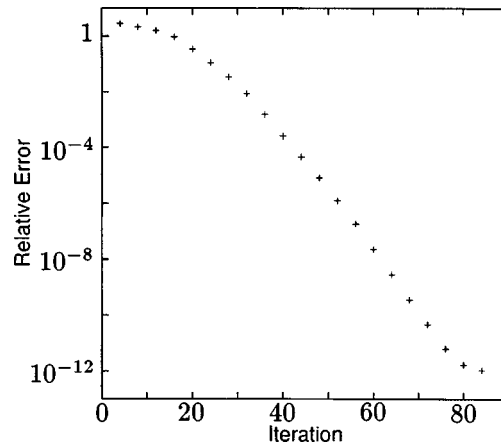$$\psi_{i+1} = \beta_{i+1}^{-1}(H\psi_i - \alpha_i \psi_i - \beta_i \psi_{i-1}) \tag{9}$$

FIG. 1. Convergence of the generalized Lanczos algorithm for a random matrix of the form (3) and size $2N = 200000$.

applicable to any Hermitian matrix H. When $K=T$ and $\xi_1 = \eta_1$, both Equations (8) coincide with each other and with Eq. (9), up to notation.

As in the case of the Hermitian Lanczos algorithm, the several lowest frequencies can be found by projecting the ξ and η components of converged eigenvectors out of the $\mathcal{V}_n$ and $\mathcal{U}_n$ subspaces, respectively.

The method was tested on a set of large sparse random matrices of the form (3). Symmetric matrices T and K were generated having an average of 40 randomly distributed and randomly positioned matrix elements in each row. Both K and T were shifted by an appropriate constant to ensure positive-definiteness. Figure 1 demonstrates the convergence results for a matrix of size $2N = 200000$.

For smaller matrices up to $2N = 2000$, where it was possible to obtain all eigenvalues with regular methods, the present method has converged to the true lowest frequency in all instances.

In conclusion, we have proposed a method that generalizes the Rayleigh–Ritz variational procedure and Lanczos recursion to the case of non-Hermitian matrices of the form (3) which determine the normal modes and frequencies of small-amplitude oscillations of Hamiltonian systems.

Equations (2) have numerous applications beyond purely mechanical problems. The Schrödinger equation in a nonorthogonal basis represents a generalized symmetric eigenvalue problem similar to (1). The RPA and other time-dependent techniques in nuclear physics and quantum chemistry lead to equations similar to (2).[3,5] Last, eigenvectors of so-called Hamiltonian matrices, of which (3) is a special case, solve the nonlinear algebraic Riccati equation which appears in the theory of stability and optimal control.[6]

[1] L. D. Landau and E. M. Lifshitz, *Mechanics*, Butterworth–Heinemann, Oxford (1996).

[2] B. N. Parlett, *The Symmetric Eigenvalue Problem*, Prentice Hall, London (1980).

[3] D. J. Thouless, Nucl. Phys. **22**, 78 (1961).

[4] C. Lanczos, J. Res. Natl. Bur. Stand. **45**, 255 (1950).

[5] J.-P. Blaizot and G. Ripka, *Quantum Theory of Finite Systems*, MIT Press, Cambridge, Mass. (1986).

[6] S. Bittanti, A. J. Laub, and J. C. Willems (eds.), *The Riccati Equation*, Springer-Verlag, Berlin (1991).

Condensed water in superfluid He-II

L. T. Mezhov-Deglin and A. M. Kokotin

Institute of Solid-State Physics, Russian Academy of Sciences, 142432 Chernogolovka, Moscow Region, Russia

It was found that when ^{4}He gas containing water vapor as an impurity condenses on the surface of superfluid He-II cooled to ~ 1.4 K, semitransparent clouds (icebergs) form in the volume of a glass cell filled with He-II below the He-II surface. The form of the icebergs extracted from the superfluid liquid remains virtually unchanged on heating up to ~ 1.8 K. In the temperature range 1.8–2.2 K the thermometers register sharp temperature jumps, which are accompanied by jumps in the gas pressure in the cell and a repeated decrease, by more than two orders of magnitude, in the total volume of the condensate, i.e., the water content in the volume of an iceberg does not exceed 10^{20} H_2O molecules per 1 cm^3. It can be inferred that porous icebergs, permeated with superfluid liquid and containing cores consisting of small clusters surrounded by a layer of solidified helium, form in the volume of He-II as the gas mixture condenses. © *1999 American Institute of Physics.*
[S0021-3640(99)00823-3]

PACS numbers: 67.40.Yv

In the present letter we report observations of metastable water clouds (icebergs) that form in superfluid He-II when helium gas containing water vapor as an impurity condenses. Judging from the results of our investigations and the published data[1–5] on the properties of condensates of molecular gases in superfluid helium, it can be inferred that in the process of condensation, porous icebergs permeated with He-II, whose cores consist of small water clusters surrounded by a layer of solidified helium, form in the volume of the superfluid liquid. The observed water condensate can be called a ''water gel'' by analogy with aerogel.

We note that the possibility of the formation of a metastable condensate in helium when an impurity gas is introduced into a cryostat containing liquid helium was reported in Ref. 1, published more than 50 years ago. It was discovered that at temperatures below 2.5 K the properties of the impurity particles formed and the character of their interaction depend strongly not only on the composition of the impurity but also on the temperature and the properties of liquid helium. For example, when air impurity was introduced into the cryostat, a fog formed in the vapor above the liquid, i.e., impurity gas molecules joined into small clusters. The rate of settling of air clusters in liquid ^{4}He and the form of the ''flakes'' formed in the volume of the liquid as a result of the clusters sticking together changed substantially as temperature decreased and a transition from normal
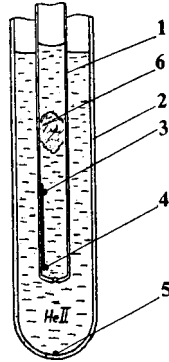
FIG. 1. Diagram of the apparatus. *1* — Cell, *2* — ampul, *3*, *4*, *5* — thermometers, *6* — iceberg.

He-I to superfluid He-II occurred. Moreover, it was found that the flakes containing water impurity decomposed when the liquid was heated and a transition from He–II to He–I to occurred. The results of the observations in Ref. 1 served as a basis for the development of a method for producing small particles (clusters with average diameter 5–7 nm) by evaporating metal in helium vapors, which is widely used today for decorating the distribution of vortices in superconductors (see, for example, Refs. 6 and 7), as well as methods for preparing metastable condensed systems containing molecules and atoms (free radicals)of molecular gases.[2] A setup for introducing into a cryostat a helium gas jet, containing impurity molecules and atoms of the molecular gas under study (nitrogen, for example), directed onto the surface of superfluid He-II and the first results of the investigations of the properties of a metastable nitrogen condensate containing nitrogen molecules and atoms are described in Refs. 2–4. Subsequent x-ray measurements[5] have shown that in the cold vapor above a liquid helium surface most impurity molecules and atoms join into clusters with average diameter ~6 nm, so that in accordance with the results of Refs. 1 and 5–7 primarily a cluster beam enters the liquid helium. The interaction between clusters in the He–II volume leads to the formation of a metastable porous condensate, which we mentioned at the outset.

The construction of the apparatus is shown schematically in Fig. 1. The experimental cell — a glass tube *1* with an inner diameter of 9 mm and a 1.5 mm in diameter exit opening at the bottom of the tube — is placed inside a glass ampul *2*. The apparatus is placed inside a glass helium dewar. The ampul and the cell can be periodically filled with superfluid liquid from an external helium bath using a heat pump. The germanium thermometers *3*, *4*, and *5*, placed inside the cell and at the bottom of the ampul, make it possible to monitor the temperature distribution in the apparatus. ^{4}He gas with water vapor impurity enters the cell at the top. As is evident from Fig. 1, in our apparatus all of the gas condenses inside the experimental cell, in contrast to the apparatus described in Ref. 2, where a substantial portion of the entering gas flow is carried off together with the liquid helium vapors into the evacuation line of the dewar.

A differential manometer (not shown in Fig. 1), connected with the mixture feed line, making it possible to measure the difference of the gas pressures between the tube and the helium dewar and, if necessary, to connect the cell to the outer helium bath in order to equalize the pressures, is used to monitor the rate of inflow of the gas. Besides
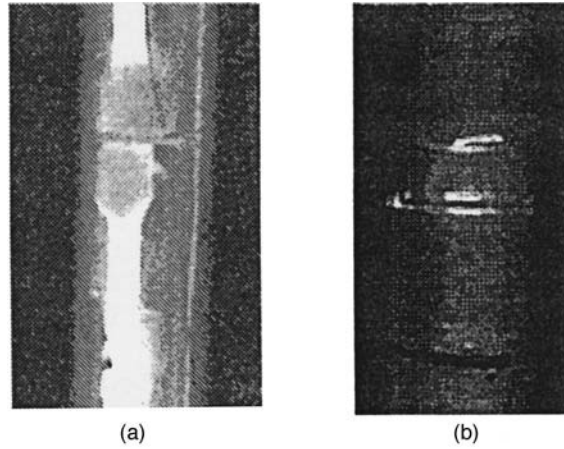
FIG. 2. a — Photograph of icebergs located below the He–II surface. b — The dome-shaped top of an iceberg protrudes above the He-II surface in the cell (the level of the liquid in the ampul is lower than the He-II level in the cell).

visual observations of the processes occurring in the cell as the impurity accumulattes and the condensate heats up, a vidoeo tape recording of the experiment was made using a camera placed outside the dewar.

Before the experiment started, the dewar was filled with liquid ^{4}He and then cooled to temperature $T = 1.3 - 1.4$ K by evacuating the liquid helium vapors. Then, using a heat pump, the ampul and cell were filled with superfluid He-II. ^{4}He gas containing about 3% water vapor impurity entered the cell through the top of the tube, which was connected to the mixture feed line through a fine-adjustment valve. As the observations showed, the optimum rate of accumulation of gas was ~ 0.5 cm^3/sec at atmospheric pressure, and the pressure difference between the gas inside the tube and the dewar was maintained at 100–200 Pa. The warm gas was cooled as the flow moved along the tube and condensed on the He-II surface. The He-II temperature in the cell and ampul increased by less than 0.1 K during the accumulation process. Naturally, a substantial portion of the impurities condensed in the form of ice on the glass wall at the top of the tube. For this reason, the water content in the condensate formed in the He-II volume can be judged only on the basis of the experimental results.

Several minutes after condensation commenced, a cloud, which is semitransparent in visible light and possesses a diameter close to that of the cell, appeared above the surface of the liquid and slowly slid downward along the wall of the tube. With feed line closed and a constant temperature in the cell $T \sim 1.4$ K, the initial shape of the cloud changed with time: from a ''soft'' cloud with shape varying in the course of the motion to a more dense (judging from the decrease in light transmission), virtually stationary, ''iceberg'' with average diameter close to that of the tube, suspended on the walls inside the cell at a certain distance from the surface of the liquid. Opening the feed line once again, we were able to prepare two or three icebergs, located one under another inside the cell (Fig. 2a). Naturally, as the impurity accumulated, some of it condensed on the cell walls directly near the liquid–vapor interface. This resulted in the appearance of a meniscus
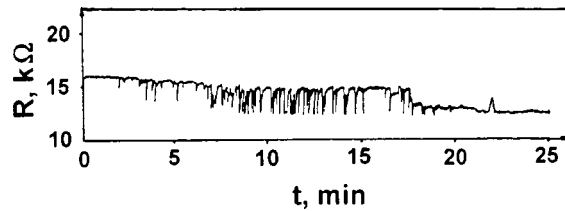
FIG. 3. Temperature jumps accompanying heating of the icebergs in a helium gas atmosphere (top thermometer). Initial temperature $T = 1.8$ K, the amplitude of the jumps corresponds to $\Delta T \sim 0.3$ K.

with a depth of the order of 1–2 mm on an initially flat He–II surface. If condensation is stopped and the He-II level in the cell is increased, the liquid surface once again becomes flat, i.e., the superfluid helium wets well the water condensate formed, much more strongly than the surface of the glass wall.

As the level of superfluid liquid in the cell was subsequently gradually decreased, a shiny upper edge of the iceberg was observed to emerge above the He-II surface (Fig. 2b). Then, the iceberg abruptly shifted downwards and stopped once again at some distance below the surface of the liquid. Several successive jumps of the iceberg could be observed as the level of the liquid decreased monotonically. The jumps of the icebergs were accompanied by pressure jumps in the cell, but the temperature of the liquid remained virtually unchanged, i.e., the hops were caused by the efflux of cold gas from the surface of an iceberg heated by an external light source (an iceberg absorbs visible light much more strongly than liquid helium or the walls of the glass apparatus).

An even stronger flow of helium gas was observed from the surface of ''dry'' icebergs, lying at the bottom of the cell, from which liquid helium was just removed. As long as the He-II level in the ampul 2 (Fig. 1) was located at a distance of 0.5–2 mm from the exit opening, a distinct, ~ 1 mm deep, cone could be seen on the surface of the liquid; this cone indicated the existence of a strong gas jet emanating from the cell. In the helium gas atmosphere, the temperature of the icebergs heated by the external light source increased monotonically from ~ 1.4 to ~ 1.8 K over a long time (tens of minutes). In the range 1.8–2.2 K the thermometers 3 and 4 recorded sharp temperature jumps with amplitude $\Delta T \sim 0.3$ K (the time variation of the indications of the upper thermometer are illustrated by the thermogram shown in Fig. 3; the trace was started when the temperature inside the cell increased to 1.8 K). The temperature jumps were accompanied by pressure jumps and breakup of the iceberg into small ice particles. The total volume of the condensate decreased by almost two orders of magnitude. Above 2.2 K the jumps ceased, and the gas temperature inside the cell increased quite rapidly to $T \geqslant 4.2$ K. From these observations it is easy to estimate that the water content inside an iceberg is of the order of 10^{20} molecules/cm^3 and the interaction energy between the clusters formed by the water gel does not exceed tens of K.

It is important to note that the volume of the icebergs in a cell filled with liquid remained essentially unchanged as the temperature increased from 1.4 to 4.2 K. For this reason, the decomposition of the condensate in a gas atmosphere cannot be explained only by a decrease in the thermal conductivity of the liquid, permeating the porous matter, at a transition from He-II to He-I.

A large quantity of condensate accumulated in the volume and at the bottom of the cell with prolonged accumulation of the gas mixture. In this case, the pressure jumps in a closed cell with a decrease in the He-II level reached $\Delta P \sim 2000$ Pa, which led to extrusion of part of the condensate through the exit opening into the ampul. As a result, a layer of a fine-grain white powder appeared in the liquid at the bottom of the ampul; this powder remained stable as the temperature of the liquid helium increased from 1.4 to 4.2 K, just as the ice particles formed on the cell walls after the icebergs broke up. Therefore, even small, nonuniform mechanical stresses can break up the porous condensate in a superfluid liquid.

In conclusion, we note that the investigations of the properties of ''soft'' clouds formed at the moment at condensation and icebergs into which they transform with time are continuing. By analogy with condensates of molecular gases, it is natural to infer that the water condensate in superfluid helium consists mainly of water clusters with average diameter of the order of 5 nm (i.e., one cluster contains of the order of 10^4 H_2O molecules), surrounded by a layer of solidified helium. The interaction between these particles results in the appearance of a new porous substance (water gel), whose properties vary appreciably with time even at constant temperature $T \geqslant 1.3$ K and/or with a change in temperature and properties of the liquid helium permeating the porous system.

[1] P. Savich and A. Shalnikov, J. Phys. USSR **10**(3), 299 (1946).

[2] E. B. Gordon, L. P. Mezhov-Deglin, O. F. Pugachev, and V. V. Khmelenko, Prib. Tekh. Éksp. **6**, 247 (1975).

[3] E. B. Gordon, L. P. Mezhov-Deglin, and O. F. Pugachev, JETP Lett. **19**, 63 (1974).

[4] E. B. Gordon, L. P. Mezhov-Deglin, O. F. Pugachev, and V. V. Khmelenko, Zh. Éksp. Teor. Fiz. **73**, 952 (1977) [Sov. Phys. JETP **46**, 502 (1977)].

[5] V. Kiryukhin, B. Kreimer, R. E. Boltnev *et al.*, Phys. Rev. Lett. **79**, 1774 (1997).

[6] L. Ya. Vinnikov and A. O. Golubok, ''High-resolution method of direct observation of magnetic structure on the surface of type-II superconductors,'' Preprint, Institute of Solid-State Physics, Russian Academy of Sciences, Chernogolovka (1984), p. 9.

[7] L. Ya. Vinnikov, I. V. Grigor'eva, and L. A. Gurevich, in *The Real Structure of HTSC Superconductors,* Springer Series in Material Science **23**, edited by V. Sh. Shehtman (Springer, New York, 1993) p. 89.

Magnetoplastic effect in LiF crystals and longitudinal spin relaxation

V. I. Al'shits*) and E. V. Darinskaya†)

Institute of Crystallography, Russian Academy of Sciences, 117333 Moscow, Russia

New features of the dependence of the average travel distance l of dislocations on the magnetic field B have been found in an investigation of the magnetostimulated dislocation mobility in LiF crystals: A transition has been found from ordinary proportionality $l \propto B^2$ to saturation $l \approx$ const in high fields B. It is shown that the experimental points can be described satisfactorily by the theoretical dependence $l \propto [(B_0/B)^2 + 1]^{-1}$ ($B_0 \approx 0.8$ T), typical for the mechanism of longitudinal spin relaxation in a system of radical pairs, which are supposedly formed when dislocation nuclei interact with paramagnetic impurity centers. According to the theory, the level of the field B_0 is determined by the characteristic frequency of the oscillations of the internal fields in the lattice, which for $B_0 \sim 1$ T is of the order of $10^{11}\,\mathrm{s}^{-1}$, which corresponds to the typical frequency of characteristic oscillations of dislocation segments between pinning centers, which, naturally, does not depend on temperature. This in turn explains the fact that the measured values of B_0 are the same at 293 K and 77 K. © *1999 American Institute of Physics.* [S0021-3640(99)00923-8]

PACS numbers: 75.80.+q, 61.72.Lk

Among the spin effects occurring in nonmagnetic materials there is a group of phenomena that stands out. These are phenomena that are limited by spin conversion in definite centers under the action of an external magnetic field. This conversion process terminates with a change in the spin state of the system and corresponding removal of the quantum forbiddenness on a possible electronic transition in the system. As a result, a sharp transformation of the configuration of the system occurs. This transformation is often accompanied by a radical change in the type and level of interaction of its constituent elements. In addition, all this occurs with virtually no change in the total energy of the system, since the spin-dependent transitions under consideration are initiated in a magnetic field not by adding energy to the system but rather by removing the spin forbiddenness on the indicated transitions. Such processes have been described in Ref. 1 in connection with the observation of a magnetic effect on the rate of chemical reactions. Later a magnetic influence of the same nature on a variety of diverse processes was observed,[2] specifically, on the photocurrent in semiconductors,[3] on the viscosity of amorphous alloys,[4] and so on.

The so-called magnetoplastic effect (MPE) was the last phenomenon to be observed in this group. The MPE was first observed in Ref. 5 in NaCl crystals and consisted in magnetically stimulated depinning of dislocations from paramagnetic impurities. Over the last ten years the magnetic effect on micro- and macroplasticity of nonmagnetic crystals has been subjected to very intense study in a number of independent groups. The number of publications on this subject is approaching 100 (see, for example, Refs. 6–16). At present, there is no doubt that the MPE exists and that it is of a spin-dependent nature. However, unfortunately, the specific physical mechanisms on which it is based are not yet fully understood.

Specifically, it is still necessary to determine the type of process leading to the evolution of spins in a radical pair formed by a paramagnetic center and a dangling bond in a dislocation nucleus. In experiments with individual dislocations, their average travel distance l, which is inversely proportional to the average time τ_{dp} before depinning of a dislocation from a local stop (i.e., the characteristic spin conversion time in a pair), is usually linear in B^2. This is positively observed in NaCl, CsI, Zn, and Al crystals. Such a dependence has been found earlier also for LiF crystals in measurements of the dislocation mobility in magnetic fields $B \lesssim 1$ T. For sufficiently weak magnetic fields the linearity of the reciprocal of the evolution time of spins of unpaired electrons of a radical pair as a function of B^2 is characteristic for the spin relaxation mechanism in an external magnetic field associated with the name Brocklehurst (see Ref. 1). The physical reason for this spin relaxation mechanism is anisotropy of the g factor (usually estimated to be of the order of $\Delta g \sim 10^{-2} - 10^{-3}$), which results in magnetically induced transitions between S and T spin states of radical pairs. Here it is necessary to distinguish longitudinal and transverse spin relaxation, corresponding to $S - T_{\pm}$ and $S - T_0$ transitions and characterized by the times T_1 and T_2. In the theory of recombination of radicals in solutions,[1] the rates of intercombination transitions in radical pairs, limited by longitudinal and transverse relaxations, increase differently with increasing magnetic field B:

$$T_1^{-1} = \tau^{-1} f(B^2/B_0^2), \quad T_2^{-1} = \tau^{-1}[aB^2/B_0^2 + \beta f(B^2/B_0^2)], \tag{1}$$

where

$$\tau^{-1} = \Delta g^2/5\tau_b, \quad B_0 = \hbar/\mu_B \tau_b, \quad f(B^2/B_0^2) = (B_0^2/B^2 + 1)^{-1}, \tag{2}$$

α and β are coefficients of the order of 1, μ_B is the Bohr magneton, and τ_b is the correlation time of the rotational motion of a radical. In application to the description of spin relaxation in a paramagnetic center — dislocation system, it is natural to replace the parameter τ_b by the characteristic period τ_d of the characteristic oscillations of dislocation segments pinned by paramagnetic impurities (usually $\tau_d \sim 10^{-11}$ s).

As one can see from Eqs. (1) and (2), for $B^2/B_0^2 \ll 1$ both functions $[T_1(B)]^{-1}$ and $[T_2(B)]^{-1}$ are proportional to B^2. However, for high fields ($B^2/B_0^2 \gg 1$) these dependences are characterized by a much different behavior: $[T_1(B)]^{-1} \approx$ const and $[T_2(B)]^{-1} \propto aB^2 + b$ (a and b are constant parameters). Thus, to make an experimental choice between the longitudinal and transverse spin relaxation mechanisms, measurements must be performed in high magnetic fields. In so doing, it is desirable to use as the object of investigation crystals with not too high a field B_0. As we shall see, from this standpoint, the crystal LiF is an entirely suitable object for our purposes.
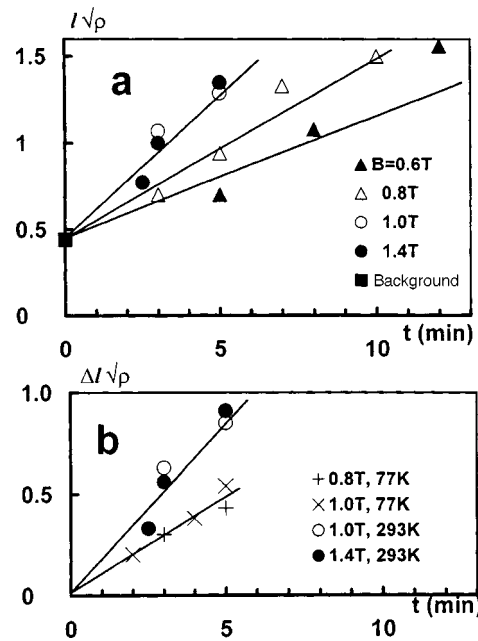
FIG. 1. Normalized average dislocation travel distance $l\sqrt{\rho}$ versus the holding time t of samples in a magnetic field for different levels of magnetic induction B (a) and two temperatures (b), $\Delta l = l - l_0$.

The experiments were performed on LiF crystals with total impurity concentration $C \approx 10^{-5}$ moles/mole and yield point $\tau_y = 300$ kPa. Fresh dislocations with average density $\rho_d \lesssim \rho$ were introduced by a light impact into preannealed samples with dislocation density $\rho_d \sim 10^4$ cm^{-2}. Their initial positions were fixed using the standard method of selective chemical etching of crystal surfaces. Next, the samples were placed in a constant magnetic field $B = 0.4 - 1.4$ T for time $t = 2 - 12$ min at room and liquid-nitrogen temperatures. No mechanical load was applied, so that the driving force for dislocations after their magnetostimulated depinning from local centers was due to long-range internal stresses from other dislocations. In individual experiments, to increase the average travel distance l, an additional force on charged edge dislocations was produced using an external constant electric field $E = 3 - 6.1$ kV/m, applied simultaneously with a magnetic field. After magnetic treatment, the sample was subjected to repeated chemical etching to determine the new positions of the dislocations. Next, histograms of dislocation travel distances were constructed and the average travel distance l was calculated according to them.

Figure 1a demonstrates the dependence of the average dislocation travel distance l, scaled to the average distance between dislocations $(1/\sqrt{\rho})$, on the ''magnetization'' time t for different fields B at 293 K. The background travel distance l_0 at $t = 0$ is determined by etching out near-surface stops and does not depend on the parameters varied. It is easy to see that the increase in the slope of the linear dependence $l(t)$ with increasing magnetic field B stops at quite high fields. Lowering the temperature to 77 K decreases the slope dl/dt somewhat, but it does not change the saturation of the average travel distance l with respect to the magnetic field (see Fig. 1b). Even more pronounced saturation
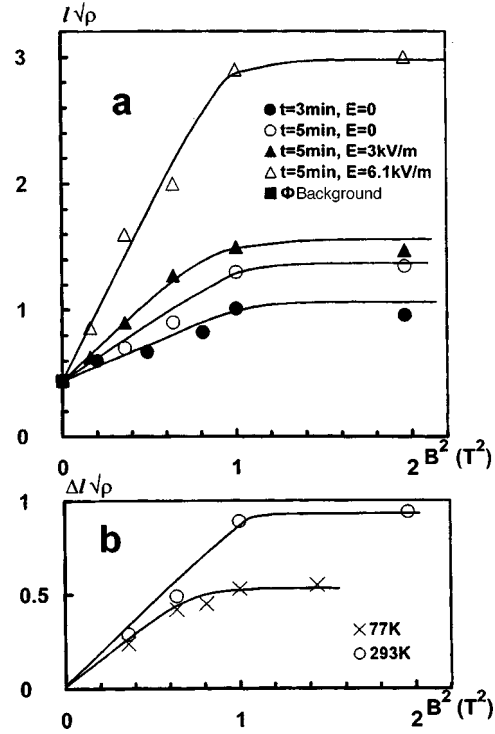
FIG. 2. Saturation of dislocation travel distances in high magnetic fields for different magnetic treatment times t and electric fields E (a) and at two temperatures (b).

appears in the coordinates $l(B)$ (Fig. 2a and 2b). It is significant that the decrease of the time t from 5 to 3 min (Fig. 2a) also decreases the saturation level, i.e., the latter is not related with the geometric limit typical of relaxation displacements.

Thus, the behavior of the dependence $l(B)$ in relatively high fields suggests that the observed effect is based on longitudinal spin relaxation processes in a magnetic field, and the depinning time τ_{dp} of a dislocation from an impurity center can be identified with the time T_1 (1). If this assumption is correct, then all experimental curves in Figs. 2a and 2b should be described by the dependence

$$l\sqrt{\rho}=At(B_0^2/B^2+1)^{-1}, \tag{3}$$

where A is an adjustable parameter that depends on the temperature and the force acting on the dislocation (specifically, on the intensity of the electric field), and the field B_0 $=\hbar/\mu_B\tau_d$, determined by the characteristic frequency of the oscillations of the dislocation segments, can depend on the impurity concentration but not on the temperature or the electric field E. In Fig. 3 the experimental points are the data from Figs. 2a and 2b replotted in the coordinates $(l\sqrt{\rho}/At-B^2/B_0^2)$ for four values of the parameter A, and the solid curve corresponds to the function $(B_0^2/B^2+1)^{-1}$ with $B_0=0.8$ T. This level of the field B_0 corresponds to $\tau_d=\hbar/\mu_B B_0\sim 10^{-11}$ s, which agrees completely with the generally accepted estimate of the period of the characteristic oscillations of dislocation segments pinned by point defects. We note that for this scale of the parameter τ_d and
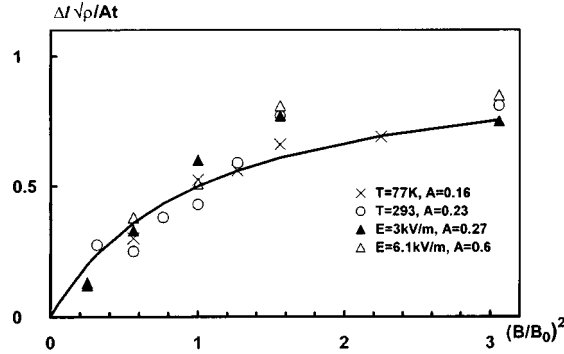
FIG. 3. Experimental points from Fig. 2, replotted in the coordinates $(\Delta l \sqrt{\rho}/At - (B/B_0)^2)$, in comparison with the theoretical dependence $[(B_0/B)^2 + 1]^{-1}$ (solid curve), $B_0 = 0.8$ T.

characteristic values of the g-factor anisotropy $\Delta g \sim 10^{-2} - 10^{-3}$, the characteristic time τ corresponding to $T_1^{\min}$ as $B \to \infty$ in Eqs. (1) and (2) is unexpectedly large and is estimated as $10^{-4} - 10^{-6}$ s, which, incidentally, agrees fairly well with the estimate of the depinning time τ_{dp} presented in Ref. 10 on the basis of completely independent considerations.

The satisfactory agreement between the theoretical curve and the experimental points attests to the hypothesis that longitudinal spin relaxation plays a determining role. The possibility of describing the curves $l(B)$ for two strongly different temperatures 77 and 293 K using the same parameter $B_0 = 0.8$ T also confirms this hypothesis. The prediction, following from the scheme considered above, that B_0 increases with the impurity concentration, resulting in a decrease of the average length of dislocation segments and hence the characteristic time τ_d, should also be checked. Unfortunately, at present we do not have the required crystals with different level of doping with the same impurities, so that this check is postponed for the future.

In closing, we thank A. I. Shushin for helpful suggestions and discussions, L. M. Soĭfer for the LiF crystals, and V. P. Kisel' for assisting in the preparation of the samples. This work is supported by an Russian Fund for Fundamental Research Grant 97-02-16327.

[1] A. L. Buchachenko, R. Z. Sagdeev, and K. M. Salikhov, *Magnetic and Spin Effects in Chemical Reactions* (Nauka, Novosibirsk, 1978).

[2] Ya. B. Zel'dovich, A. L. Buchachenko, and E. L. Frankevich, Usp. Fiz. Nauk **155**, 3 (1988) [Sov. Phys. Usp. **31**, 385 (1988)].

[3] V. V. Kveder, Yu. A. Osip'yan, and A. I. Shalynin, Zh. Éksp. Teor. Fiz. **83**, 699 (1982) [Sov. Phys. JETP **56**, 389 (1982)].

[4] S. A. Dembovskiĭ, E. A. Chechetkin, and S. A. Kozyukhin, JETP Lett. **41**, 88 (1985).

[5] V. I. Al'shits, E. V. Darinskaya, T. M. Perekalina, and A. A. Urusovskiĭ, Fiz. Tverd. Tela (Leningrad) **29**, 467 (1987) [Sov. Phys. Solid State **29**, 265 (1987)].

[6] V. I. Alshits, E. V. Darinskaya, and E. A. Petrzhik, Mater. Sci. Eng., A **164**, 322 (1993).

[7] Yu. I. Golovin and R. B. Morgunov, JETP Lett. **58**, 191 (1993).

[8] M. I. Molotskii, R. E. Kris, and V. N. Fleurov, Phys. Rev. B **51**, 12531 (1995).

[9] Yu. I. Golovin and R. B. Morgunov, JETP Lett. **61**, 596 (1995).

[10] V. I. Al'shits, E. V. Darinskaya, O. L. Kazakova *et al.*, JETP Lett. **63**, 668 (1996).

[11] V. I. Alshits, E. V. Darinskaya, O. L. Kazakova *et al.*, Mater. Sci. Eng., A **234-236**, 617 (1997).

[12] M. I. Molotskii and V. Fleurov, Phys. Rev. Lett. **78**, 2779 (1997).

[13] Yu. I. Golovin and R. B. Morgunov, Zh. Éksp. Teor. Fiz. **115**, 605 (1999) [JETP **88**, 332 (1999)].

[14] V. I. Al'shits, N. N. Bekkauer, A. E. Smirnov, and A. A. Urusovskaya, Zh. Éksp. Teor. Fiz. **115**, 951 (1999) [JETP **88**, 523 (1999)].

[15] N. A. Tyapunina, V. L. Kransnikov, and É. P. Beloserova, Fiz. Tverd. Tela (St. Petersburg) **41**, 1035 (1999) [Phys. Solid State **41**, 942 (1999)].

[16] E. V. Darinskaya and M. V. Koldaeva, JETP Lett. **70**, 228 (1999).

Translated by M. E. Alferieff

Quantum Hall effect in the bulk semiconductors bismuth and antimony tellurides: proof of the existence of a current-carrier reservoir

V. A. Kul'bachinskiĭ and A. Yu. Kaminskiĭ

M. V. Lomonosov Moscow State University, 119899 Moscow, Russia

N. Miyajima, M. Sasaki, H. Negishi, M. Inoue, and H. Kadomatsu

Graduate School of Advanced Sciences of Matter, Hiroshima University, 739-8526 Higashi-Hiroshima, Japan

The quantization of the Hall resistivity ρ_{xy} in the form of plateaus in the dependence of ρ_{xy} on the magnetic field B is observed in the semiconductors Bi_2Te_3 and Sb_2Te_3; the minima of the transverse magnetoresistivity ρ_{xx} correspond to the start of the plateaus. The quantization of ρ_{xy} is due to the presence of a current-carrier reservoir. An impurity band with a high density of states or a different band with a much higher current-carrier effective mass serves as the reservoir. © *1999 American Institute of Physics.* [S0021-3640(99)01023-3]

PACS numbers: 72.20.My, 73.40.Hm

1. The quantum Hall effect[1,2] still arouses enormous interest among investigators. For an ordinary two-dimensional system (2D), it consists in the fact that the off-diagonal component of the resistivity tensor (the Hall resistivity ρ_{xy}) at low temperatures in a strong perpendicular magnetic field is quantized: $\rho_{xy} = h/ie^2$, where $i = 1,2,3 \ldots$ In other words, plateaus appear in the dependence of ρ_{xy} on the magnetic field B. The diagonal component (the transverse magnetoresistivity ρ_{xx}) oscillates in a manner so that the minima of ρ_{xx} correspond to the centers of the plateaus. The presence of localized states between the Landau levels and extended states at the center of each level explains the appearance of plateaus.

In semiconductor superlattices, where the degree of three-dimensionality can be regulated by preparing layers of different thickness, the presence of current-carrier dispersion in the direction of a magnetic field directed perpendicular to the layers still does not destroy the quantum Hall effect, though a number of features appear.[3] Surface states can play a fundamental role in the existence of the quantum Hall effect in three-dimensional objects.[4] Oscillations of the Hall coefficient are also observed in bulk InSb near the metal–insulator transition.[5]

We have investigated the quantization of the diagonal ρ_{xx} and off-diagonal ρ_{xy} components of the resistivity tensor of the bulk semiconductors Bi_2Te_3, Sb_2Te_3, and $Bi_{2-x}Sb_xTe_3$ at low temperatures in a strong magnetic field. Plateaus were observed to

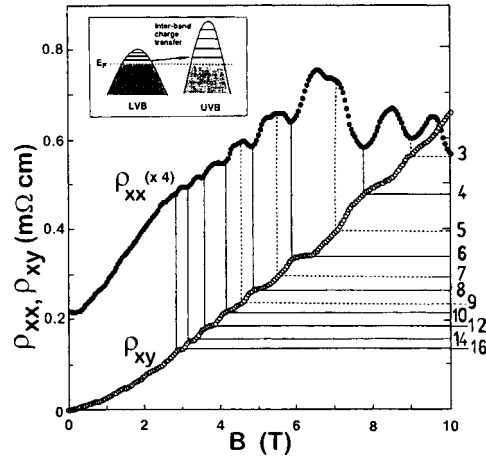FIG. 1. Hall resistivity ρ_{xy} and transverse magnetoresistivity ρ_{xx} versus the magnetic field B for Bi_2Te_3 at $T = 0.3$ K. Inset: Structure of the valence band in Bi_2Te_3 and Sb_2Te_3. *LVB* — lower valence band, *UVB* — upper valence band, E_F — Fermi level.

appear in the dependence of the Hall resistivity ρ_{xy} on the magnetic field. An important feature is that the minima of the oscillations of ρ_{xx} coincide with the start of the plateaus in ρ_{xy}.

2. Bismuth telluride Bi_2Te_3, like antimony telluride Sb_2Te_3, belongs to semiconductors with the symmetry group D_{3d}^5. Grown with stoichiometric composition, both semiconductors are always *p*-type with a high hole density because of the presence of crystalline charged point defects. Ordinarily, these are so-called antistructural defects, i.e., Bi (or Sb) occupies the Te position in the crystal lattice. The band gap E_g in Bi_2Te_3 and Sb_2Te_3 is indirect and is approximately $E_g = 0.20$ meV (Bi_2Te_3) and $E_g = 0.25$ meV (Sb_2Te_3) at room temperature, increasing to 0.25 meV and ≈ 0.26 meV, respectively, as temperature decreases to 4.2 K.[6] The valence band of both semiconductors is a multivalley band and consists of an upper valence band (*UVB*) and a lower valence band (*LVB*). Both valence bands are hexaellipsoidal. The ellipsoids possess anisotropy $S_{max}/S_{min} \approx 3.8$ and are tilted with respect to the basal plane by the angle $\theta \approx 31.5°$ and $\theta \approx 50°$ in Bi_2Te_3 and Sb_2Te_3, respectively. The energy gap ΔE_v between the bands is about 20 meV and 30 meV for Bi_2Te_3 and Sb_2Te_3.[7,8] The schematic structure of the valence-band top in Bi_2Te_3 and Sb_2Te_3 is shown in the inset in Fig. 1. Filling of the lower valence band starts at hole density exceeding the critical value $p_0 \approx 5 \cdot 10^{18}$ cm^{-3}. An important feature is the difference of the effective masses in the upper and lower valence bands: The cyclotron mass in Bi_2Te_3 is $m_c^U \approx 0.08 m_0$ in the upper valence band and $m_c^L \approx 0.16 m_0$ in the lower band.[7,8] In the mixed crystals $Bi_{2-x}Sb_xTe_3$ the energy spectrum varies smoothly with increasing x from the Bi_2Te_3 to the Sb_2Te_3 spectrum. This is expressed as a large increase of the effective masses in the lower valence band (to $m_c^U \approx m_0$). When bismuth telluride was doped with tin, an impurity band,[9,10] lying above the top of the lower valence band against the background of the states of the upper valence band (inset in Fig. 2), was also observed.

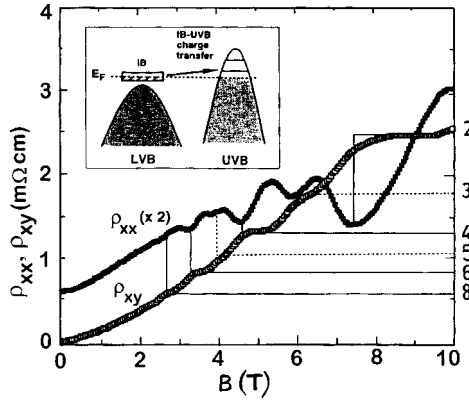In the present work we investigated samples grown by a modified Bridgman method

FIG. 2. Hall resistivity ρ_{xy} and transverse magnetoresistivity ρ_{xx} versus the magnetic field B for $Bi_{2-x}Sn_xTe_3$ at $T = 0.3$ K. Inset: Structure of the valence band in $Bi_{2-x}Sn_xTe_3$. *LVB* — lower valence band, *UVB* — upper valence band, *IB* — impurity band, E_F — Fermi level.

with characteristic dimensions $1 \times 0.5 \times 5$ mm^3 and hole density $p > p_0$ and Hall hole mobility at liquid-helium temperature $\mu_H \approx 6000-7000$ cm^2/V·s (Bi_2Te_3 and $Bi_{2-x}Sn_xTe_3$) and $\mu_H \approx 650$ cm^2/V·s (Sb_2Te_3 and the mixed crystals $Bi_{2-x}Sb_xTe_3$). The current was directed along the C_2 axis, and the magnetic field was perpendicular to the current in the direction of the C_3 axis.

3. Curves of ρ_{xx} and ρ_{xy} for Bi_2Te_3 and $Bi_{2-x}Sn_xTe_3$ as a function of the magnetic field at $T = 0.3$ K are presented in Figs. 1 and 2. As one can see from Fig. 1, plateaus appear in the dependence of the Hall resistivity ρ_{xy} on the magnetic field B. The minima of the resistivity ρ_{xx} correspond to the start of the plateaus. The broken lines mark features corresponding to the spin splitting of the Landau levels. The frequency of the oscillations of ρ_{xx} corresponds to the extremal section of the Fermi surface of the upper hole band (for $B \parallel C_3$ the cross sections of the Fermi surface from all six ellipsoids coincide). Oscillations of the resistivity from the lower valence band in Bi_2Te_3 are not observed, since the hole mobility in it is much lower and the quantization of the spectrum still does not appear in the magnetic-field range presented. As the temperature increases to 4.2 K, the effect washes out and the plateaus in $\rho_{xy}(B)$ vanish completely. The plateaus are more distinct in $Bi_{2-x}Sn_xTe_3$. This is because a small addition of tin in Bi_2Te_3 substantially increases the hole mobility and decreases the Dingle temperature of the Shubnikov–de Haas oscillations.[11] As an example, the dependences $\rho_{xx}(B)$ and $\rho_{xy}(B)$ for $Bi_{1.995}Sn_{0.005}Te_3$ are presented in Fig. 2. As the temperature decreases from 4.2 K to 0.3 K, the width of the plateaus increases, the slope of the plateaus decreases, and the plateaus corresponding to the spin splitting of the Landau levels (odd numbers in Fig. 2) become sharper. The substantially higher temperature at which plateaus can be observed in $Bi_{2-x}Sn_xTe_3$ as compared with Bi_2Te_3 is a consequence of the higher hole mobility of the upper valence band in $Bi_{2-x}Sn_xTe_3$ than in the initial Bi_2Te_3 samples.

4. The explanation of the appearance of plateaus in $\rho_{xy}(B)$ is that in an experiment oscillations of $\rho_{xx}(B)$ can be observed only from holes in the upper valence band, while the density of these holes varies in a magnetic field. The Fermi level in $Bi_{2-x}Sn_xTe_3$ was fixed in an impurity band with a high density of states. As the magnetic field increases
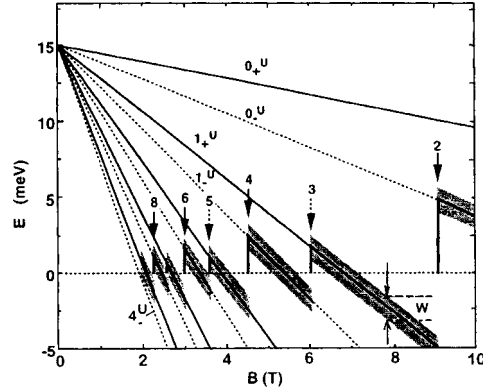
FIG. 3. Calculation of the motion of Landau levels with up spin (+, solid line) and down spin (−, broken line) in a magnetic field for $Bi_{2-x}Sn_xTe_3$.

and the next Landau level emerges [which corresponds to a maximum in the dependence $\rho_{xx}(B)$], the current carriers flow from the impurity band (*IB*) into the next Landau level (the number of states in which increases in proportion to the magnetic field) in the upper valence band (*UVB*), as shown in the inset in Fig. 1. Since the Hall resistivity $\rho_{xy}(B)$ $\sim R_H B$ and the Hall coefficient $R_H \sim 1/pe$, the hole density p in the upper valence band (these are the holes that determine the Hall effect) increases with the magnetic field as B, $R_H \sim 1/Be$, and $\rho_{xy}(B) =$ const up to emergence of the next Landau level. The three-dimensionality of the energy spectrum (the dispersion of the current carriers in the direction of the magnetic field) causes the plateaus to acquire a small slope. We note that plateaus in $\rho_{xy}(B)$ are observed for any orientation of the magnetic field with respect to the crystallographic axes of the sample, and the frequencies of the oscillations of $\rho_{xx}(B)$ correspond to a hexaellipsoid Fermi surface.

The motion of Landau levels with the number $n_\pm^U$ in a magnetic field can be calculated using a simple model. The energy level $E_\pm^U = \bar{E}_F^U - \hbar\omega_c^U(n_\pm^U + 1/2) \pm (1/2)g^*\mu_B B$ (g^* is the effective g factor and μ_B is the Bohr magneton). The computational results are presented in Fig. 3 for the sample $Bi_{1.995}Sn_{0.005}Te_3$. The energy of each level is shown by a solid or broken line for up and down spin, respectively. The hatched bands show the broadening of each level $W = 0.8$ meV. The arrows mark the appearance of plateaus with a definite number; these same numbers are presented in Figs. 1 and 2. The computational results agree well with experiment. A similar calculation for Bi_2Te_3 also gave good agreement with experiment. The difference from the preceding case lies in the fact that in Bi_2Te_3 the lower valence band serves as the current-carrier reservoir.

5. Investigation of Sb_2Te_3 samples and samples of the mixed crystals $Bi_{2-x}Sb_xTe_3$ with an order of magnitude lower hole mobility than in Bi_2Te_3 showed that for them a plateau is also observed in the dependences $\rho_{xy}(B)$. All features of the quantum Hall resistivity described previously remain. However, because of the low hole mobility oscillations of $\rho_{xx}(B)$ and $\rho_{xy}(B)$ start in magnetic fields $B > 10$ T. As an example, ρ_{xx} and ρ_{xy} versus B at $T = 4.2$ K are presented in Fig. 4 for the sample $Bi_{0.5}Sb_{1.5}Te_3$ with $B \parallel C_3$.

In summary, a quantum Hall effect due to the presence of a current-carrier reservoir (an impurity band or the lower valence band) is observed in the bulk semiconductors
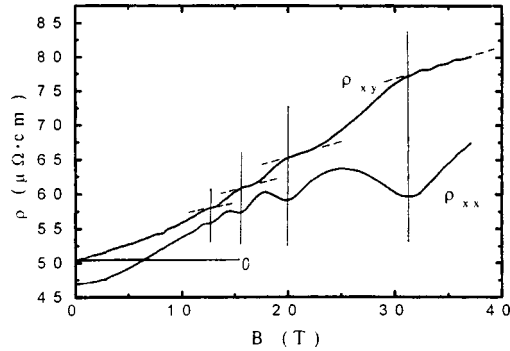
FIG. 4. Hall resistivity ρ_{xy} (measured from zero) and transverse magnetoresistivity ρ_{xx} versus the magnetic field B in $Bi_{0.5}Sb_{1.5}Te_3$ at $T = 4.2$ K.

Bi_2Te_3, Sb_2Ter_3, and $Bi_{2-x}Sb_xTe_3$ with a complicated energy spectrum. An important feature of the effect is that the minima of $\rho_{xx}(B)$ correspond not to the center but rather to the start of the plateaus in $\rho_{xy}(B)$.

[1] K. von Klitzing, G. Dorda, and M. Pepper, Phys. Rev. Lett. **45**, 494 (1980).
[2] D. C. Tsui and A. C. Gossard, Appl. Phys. Lett. **37**, 550 (1981).
[3] H. L. Stormer, J. P. Eisenstein, A. C. Gossard *et al.*, Phys. Rev. Lett. **56**, 85 (1986).
[4] S. Hill, S. Sandhu, J. S. Qualls *et al.*, Phys. Rev. B **55**, R4891 (1997).
[5] U. Zeitler, A. G. Jansen, P. Wyder, and S. S. Murzin, J. Phys.: Condens. Matter **6**, 4289 (1994).
[6] K. Funagai, Y. Miyahara, H. Ozaki, and V. A. Kulbachinskii, in *Proceedings of International Conference on Thermoelectrics*, edited by T. Caillat, Pasadena, USA, March 1996, p. 408.
[7] V. A. Kulbachinskii, M. Inoue, S. Sasaki *et al.*, Phys. Rev. B **50**, 16921 (1994).
[8] V. A. Kulbachinskii, Z. M. Dashevskii, M. Inoue *et al.*, Phys. Rev. B **52**, 10915 (1995).
[9] V. A. Kul'bachinskiĭ, N. E. Klokova, Ya. Khopak *et al.*, Fiz. Tverd. Tela (Leningrad) **31**, 205 (1989) [Sov. Phys. Solid State **31**, 112 (1989)].
[10] V. A. Kulbachinskii, N. B. Brandt, P. A. Cheremnykh *et al.*, Phys. Status Solidi B **150**, 237 (1989).
[11] V. A. Kul'bachinskiĭ, N. E. Klokova, S. Ya. Skipidorova *et al.*, Vest. MGU, ser. 3, fiz., astron. **30**, 68 (1989).

Translated by M. E. Alferieff

The widths of single-particle states of anisotropic, strongly correlated electron systems in solids

V. A. Khodel and M. V. Zverev

Kurchatov Institute, Russian Research Center, 123182 Moscow, Russia

The damping $\gamma(\varepsilon)$ of electron states in crystals is investigated beyond the phase transition point related to a rearrangement of the Fermi surface. Attention is focused on the alteration of the standard Landau theory due to the emergence of a flat portion in the spectrum $\xi(\mathbf{p})$ of single-particle excitations as a result of the rearrangement. In the limit $\varepsilon \to 0$, the width $\gamma(\varepsilon)$ of the states in the region of the Brillouin zone where the dispersion of $\xi(\mathbf{p})$ is of an ordinary order of magnitude is found to depend on ε almost linearly, in contrast to the Fermi-liquid-theory result $\gamma(\varepsilon) \sim \varepsilon^2$. © *1999 American Institute of Physics.*
[S0021-3640(99)01123-8]

PACS numbers: 71.27.+a

In a number of articles[1–5] using the Landau–Migdal quasiparticle picture, a new phase transition in strongly correlated Fermi systems, called fermion condensation, has been described. Its salient feature is in the appearance of a fermion condensate (FC), a group of degenerate single-particle states whose energy at the temperature $T=0$ coincides with the chemical potential μ. Owing to the degeneracy, the quasiparticle occupation numbers $n(\mathbf{p}, T=0)$ are no longer 1 or 0. They are determined by the variational condition

$$\delta E_0(n)/\delta n(\mathbf{p}) = \mu, \quad \mathbf{p} \in \Omega, \tag{1}$$

where $E_0[n(\mathbf{p})]$ stands for the ground-state energy, while Ω denotes the FC region, whose boundaries are determined by Eq. (1) itself. According to Landau, the left-hand side of (1) is nothing but the quasiparticle energy $\varepsilon(\mathbf{p})$, and therefore this equation implies smearing the Fermi surface — its metamorphosis into a volume in three-dimensional systems or into a surface in two-dimensional ones. The flattening of the single-particle electron spectra $\xi(\mathbf{p})$ has been experimentally observed in many quasi-two-dimensional superconductors (see, e.g., Refs. 6 and 7 and references cited therein). The observed single-particle peaks have much larger widths γ than those calculated employing Fermi liquid (FL) theory (see e.g., Refs. 8 and 9), a fact which is presumably due to the flattening of $\xi(\mathbf{p})$ near the Fermi surface.

Our purpose is to calculate the imaginary part of the mass operator $\Sigma(\mathbf{p}, \varepsilon)$ in the presence of a flat portion in the electron spectrum $\xi(\mathbf{p})$ due to the fermion condensation. In the following we consider a crystal with a cubic or square lattice, assuming the FC to

be positioned in the vicinity of the van Hove points,[4,5] the FC density $\rho_c \equiv \eta\rho$ being rather small. In regard to the momentum dependence of $\mathrm{Im}\,\Sigma(\mathbf{p},\varepsilon)$, two regions can be distinguished: i) the FC region Ω, which is made up of ''patches'' adjacent to the van Hove points, and ii) the normal region, where the dispersion has an ordinary order of magnitude, i.e., $|\nabla\xi(\mathbf{p})| = p_F/M^*$, where M^* is the effective mass of the ordinary quasiparticle, independent of T. We neglect possible variations of relevant quantities inside these regions and use the subscript c for the FC region and the subscript n for the ''normal'' one: $\mathrm{Im}\,\Sigma(\mathbf{p}\notin\Omega)\equiv\mathrm{Im}\,\Sigma_n$.

Without loss of generality, we restrict ourselves to the decay of a particle, hence implying $\varepsilon>0$ in all formulas. We focus our attention on the process of the generation of an additional particle–hole (p–h) pair and neglect contributions from collective modes, e.g., spin fluctuations, which are important for understanding many of the properties of high-T_c superconductors.[7] In doing so, we assume that T exceeds the critical temperature T_c of the superfluid phase transition at which the p–p correlations make no difference and such contributions may be omitted. In this article, we deal with energies ε exceeding a characteristic FC energy $\xi_{FC}=\langle\xi(\mathbf{p}\in\Omega)\rangle$, which, in turn, exceeds T. With these restrictions, the damping $\gamma(\mathbf{p},\varepsilon>0)$ is evaluated with the help of the formula[10]

$$\gamma(\mathbf{p},\varepsilon>0)=\frac{1}{2}\mathrm{Tr}\int\int d\tau_2 d\tau_3 \int_0^\varepsilon \frac{d\omega}{2\pi}\int_0^\omega \frac{d\varepsilon_3}{2\pi}\,|\Gamma(\mathbf{p},\varepsilon,\mathbf{p}_1,\varepsilon_1,\mathbf{p}_2,\varepsilon_2,\mathbf{p}_3,\varepsilon_3)|^2$$

$$\times\,\mathrm{Im}\,G(\mathbf{p}_1,\varepsilon_1)\,\mathrm{Im}\,G(\mathbf{p}_2,\varepsilon_2)\,\mathrm{Im}\,G(\mathbf{p}_3,\varepsilon_3). \tag{2}$$

Here $\mathbf{p}_3=\mathbf{q}+\mathbf{p}_2\equiv\mathbf{p}-\mathbf{p}_1+\mathbf{p}_2$; $\varepsilon_3=\omega+\varepsilon_2\equiv\varepsilon-\varepsilon_1+\varepsilon_2$ and $d\tau=d^n p/(2\pi)^n$ where n is the dimensionality of the lattice. Since we are only interested in clarifying the energy dependence of quantities at issue we shall omit numerical factors in future calculations.

If FL theory were applicable to systems with the FC, then the ratio $r(\varepsilon)\equiv|\gamma(\varepsilon)|/\varepsilon$ would be small, and $\mathrm{Im}\,G(\mathbf{p},\varepsilon)$ could be replaced by $-\pi\,\delta[\varepsilon-\xi(\mathbf{p})]$. However, as we shall see, the damping of single-particle states in systems with the FC is drastically enhanced compared to the predictions of FL theory. This motivates us to take into account an irregular part σ of $\mathrm{Re}\,\Sigma$ and to write $\mathrm{Im}\,G$ in the form

$$\mathrm{Im}\,G(\mathbf{p},\varepsilon)=\frac{\gamma(\mathbf{p},\varepsilon)}{(\varepsilon-\sigma(\mathbf{p},\varepsilon)-\xi(\mathbf{p}))^2+\gamma^2(\mathbf{p},\varepsilon)}. \tag{3}$$

The connection between the quantities σ and γ stems from the usual dispersion relation for the mass operator, which implies that $\sigma(\varepsilon)/\gamma(\varepsilon)\sim\ln\varepsilon$ at $\varepsilon\to0$, provided $r_c\sim1$. For example, dealing with the marginal Fermi liquid discussed in Ref. 11, one has $\gamma(\varepsilon\to0)\sim\varepsilon, \sigma(\varepsilon\to0)\sim\varepsilon\ln|\varepsilon|$.

Since the momentum dependence of quantities in the FC region is neglected, the density $N_c(\varepsilon)$ of the FC states becomes

$$N_c(\varepsilon)=-\int_\Omega \mathrm{Im}\,G_c(\mathbf{p},\varepsilon)\,d\tau=\eta\rho\,\frac{|\gamma_c(\varepsilon)|}{d_c^2(\varepsilon)}, \tag{4}$$

where $d_c^2(\varepsilon)=(\varepsilon-\sigma_c(\varepsilon)-\xi_{FC})^2+\gamma_c^2(\varepsilon)$. In the weak-damping limit, Eq. (4) reduces to $N_c(\varepsilon)=\eta\rho\,\delta(\varepsilon)$. In the strong-damping limit $r_c>1$, the contribution of the FC region $\varepsilon\simeq\xi_{FC}$, is of no importance, and then d_c^2 in Eq. (4) can be replaced by $d^2(\varepsilon)=(\varepsilon$

$-\sigma_c(\varepsilon))^2 + \gamma_c^2(\varepsilon)$. To avoid unjustified complications we restrict ourselves to the momentum-independent zeroth Landau harmonic in the Legendre expansion of the interaction amplitude $\Gamma(\cos\chi)$, where χ is the angle between the momenta of incoming particles. In this approximation, we make the replacement $\Gamma_{n_1 n_2}(\mathbf{p}_i, \varepsilon_i) \to \Gamma_{n_1 n_2}(\omega)(1 - \boldsymbol{\sigma}_1 \boldsymbol{\sigma}_2)$, where the index n_1 (n_2) indicates the number of FC states in the initial (final) state.

The damping γ decomposes into a sum

$$\gamma(\mathbf{p}, \varepsilon) = \gamma_0(\mathbf{p}, \varepsilon) + \gamma_1(\mathbf{p}, \varepsilon) + \gamma_2(\mathbf{p}, \varepsilon), \tag{5}$$

where the term $\gamma_k (k=0,1,2)$ accumulates contributions containing k final FC Green functions. It should be pointed out that for the square or cubic lattice the decay of the FC particle into a final state with no less than two FC states unambiguously results in the appearance all three FC final states.

Since we are ignoring collective modes, reserving the analysis of their role for a future article, the contributions to γ_0 overwhelmingly come from the region of momentum transfer $q \sim p_F$ quite far from the van Hove points. There the functions Γ_{00}, Γ_{01} are known to vary slowly enough, and so does the p–h propagator $A_n(q, \omega)$, the dimensionless imaginary component of which is generally written as

$$b(\mathbf{q}, \omega) = \frac{1}{N_n(0)} \int \int_0^\omega \operatorname{Im} G(\mathbf{p}, \varepsilon) \operatorname{Im} G(\mathbf{p} - \mathbf{q}, \varepsilon - \omega) \, d\tau \frac{d\varepsilon}{\pi}, \tag{6}$$

where we have introduced the density of states $N_n(0) \sim \rho M^*/\varepsilon_F^0$ as a normalization factor, ε_F^0 is the Fermi energy of a noninteracting gas with density ρ. All of them may be replaced by averaged values:

$$b_n(\omega) \sim -\omega N_n(0)/\rho, \quad |A_n(\omega) N_n(0)| \sim 1, \quad N_n^2(0) |\Gamma_{00}|^2 \sim N_n^2(0) |\Gamma_{01}|^2 \sim 1. \tag{7}$$

After these values are substituted into Eq. (2), the integrals cease to depend on $\mathbf{p}$, and we arrive at the usual result

$$\gamma_0(\varepsilon) = -\gamma_0 (\varepsilon^2/\varepsilon_F^0), \tag{8}$$

where γ_0 is a dimensionless positive constant.

When evaluating the term $\gamma_{1n}(\varepsilon)$, we combine two ordinary Green functions entering Eq. (2) into a p–h propagator A_n (see Fig. 1), so that

$$\gamma_{1n}(\varepsilon) \sim N_n(0) \int_0^\varepsilon N_c(\varepsilon - \omega) |\Gamma_{01}|^2 b_n(\omega) \, d\omega \sim \frac{1}{\rho} \int_0^\varepsilon N_c(\varepsilon_1)(\varepsilon_1 - \varepsilon) \, d\varepsilon_1. \tag{9}$$

The magnitude of this integral depends crucially on the value of $r_c(\varepsilon_1) = |\gamma_c(\varepsilon_1)|/\varepsilon_1$. If this ratio is relatively small, then the integral (9) receives its predominant contributions (of the order of 1) from the FC region, where $\varepsilon_1 \simeq \xi_{FC}$ and $N_c(\varepsilon) \sim \delta(\varepsilon)$. Then, after a simple integration, we are led to formulas inherent to marginal Fermi liquids:[11]

$$\gamma_{1n}(\varepsilon) = -\gamma_{1n} \eta \varepsilon, \quad \sigma_{1n}(\varepsilon) = \frac{2\gamma_{1n}\eta}{\pi} \varepsilon \ln \frac{|\varepsilon|}{\varepsilon_L}, \tag{10}$$

where γ_{1n} is a positive numerical constant of the order of 1. We see that the magnitude of the linear in ε term is proportional to $\eta < 1$ and is therefore quite small.
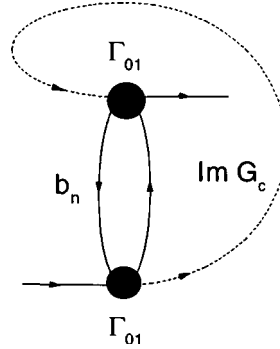
FIG. 1. The graphical representation for the contribution γ_{1n} to the total damping.

In the opposite case of strong damping with $r_c > 1$, the contribution of γ_{1n} to the damping γ is minor compared to that of γ_{2n}. In the evaluation of the latter quantity, two final FC states come into play (see Fig. 2b), and γ_{2n} is given by

$$\gamma_{2n}(\mathbf{p},\varepsilon) \sim -N_n(0) \int_{\Omega'} \int_0^\varepsilon \text{Im}\, G_n(\mathbf{p}_1, \varepsilon - \omega) \, |\Gamma_{02}(\omega)|^2 \, b_c(\omega) \, d\tau_1 \, d\omega. \tag{11}$$

Here we have introduced a special notation Ω' for the momentum integration region in (11), which is determined by the requirement that the momentum $\mathbf{p}_1$ is appropriate for the formation of a pair with momenta $\mathbf{p}_2$ and $(\mathbf{p} - \mathbf{p}_1 + \mathbf{p}_2)$ both in the FC region. We omit the insignificant term σ_n in $\text{Im}\, G_n$ and assume that η has a value be sufficient for satisfying the inequalities $\varepsilon_{\max} > |\gamma_n(\varepsilon)|$, where $\varepsilon_{\max}$ is the upper energy limit admissible for the normal states in the region Ω'; this yields

$$\int_{\Omega'} \text{Im}\, G_n(\mathbf{p} - \mathbf{q}, \varepsilon) \, d\tau_{\mathbf{q}} \sim N_n(0) \int_0^{\varepsilon_{\max}} \frac{\gamma_n(\varepsilon) \, d\xi}{(\varepsilon - \xi)^2 + \gamma_n^2(\varepsilon)} \sim -N_n(0).$$
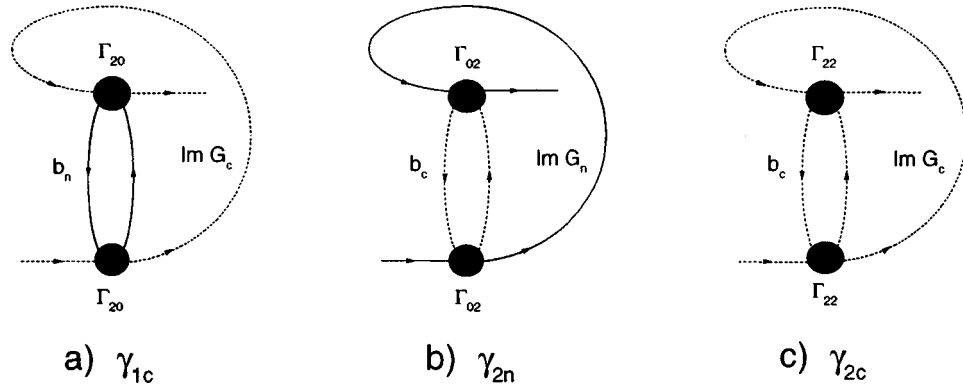
As a result, one finds

a) γ_{1c} b) γ_{2n} c) γ_{2c}

FIG. 2. The same for γ_{1c} (a), γ_{2n} (b) and γ_{2c} (c).

$$\gamma_{2n}(\varepsilon) \sim N_n^2(0) \int_0^\varepsilon |\Gamma_{02}(\omega)|^2 \, b_c(\omega) \, d\omega. \tag{12}$$

The interaction amplitude Γ_{02} is extracted from the set of algebraic equations

$$\Gamma_{02}(\omega) = \mathcal{F}_{02} + \mathcal{F}_{02} A_c(\omega)\Gamma_{22}(\omega) + \mathcal{F}_{00} A_n(\omega)\Gamma_{02}(\omega),$$

$$\Gamma_{22}(\omega) = \mathcal{F}_{22} + \mathcal{F}_{22} A_c(\omega)\Gamma_{22}(\omega) + \mathcal{F}_{20} A_n(\omega)\Gamma_{02}(\omega). \tag{13}$$

This set is easily solved to arrive at

$$\Gamma_{02}(\omega) = \mathcal{F}_{02}/D(\omega), \quad \Gamma_{22}(\omega) = [\mathcal{F}_{22}(1 - \mathcal{F}_{00} A_n(\omega)) + \mathcal{F}_{20}^2 A_n(\omega)]/D(\omega), \tag{14}$$

where $D(\omega) = (1 - \mathcal{F}_{00} A_n(\omega))(1 - \mathcal{F}_{22} A_c(\omega)) - \mathcal{F}_{02}^2 A_n(\omega) A_c(\omega)$.

Omitting the contributions of $\operatorname{Re} A_c(\omega)$, since they are insignificant,[12] and replacing $A_n(\omega)$ by $-N_n(0)$ as before, one finds

$$|N_n(0)\Gamma_{02}(\omega)|^2 \sim \frac{h_{20}^2}{h_{00}^2 + b_c^2(\omega)}, \quad |N_n(0)\Gamma_{22}(\omega)|^2 \sim \frac{1}{h_{00}^2 + b_c^2(\omega)}, \tag{15}$$

where the notation $f_{ab} = \mathcal{F}_{ab} N_n(0)$ and $h_{20} = f_{20}/[f_{22}(1 + f_{00}) - f_{20}^2]$, $h_{00} = (1 + f_{00})/[f_{22}(1 + f_{00}) - f_{20}^2]$ is introduced. With these results, Eq. (12) becomes

$$\gamma_{2n}(\varepsilon) \sim h_{20}^2 \int_0^\varepsilon \frac{b_c(\omega)\,d\omega}{h_{00}^2 + b_c^2(\omega)}. \tag{16}$$

To take the next step one needs to evaluate the propagator $b_c(\omega)$, which, in turn, requires calculating the damping γ_c of the FC particles, which is made up of three terms (5), where $\gamma_0(\varepsilon)$ is given by Eq. (8), and $\gamma_{1c}(\varepsilon)$ and $\gamma_{2c}(\varepsilon)$, depicted in Figs. 2a and 2c, are written as follows:

$$\gamma_{1c}(\varepsilon) \sim -N_n(0) \int_\Omega \int_0^\varepsilon \operatorname{Im} G_c(\varepsilon - \omega) \, |\Gamma_{20}(\omega)|^2 \, b_n(\omega) \, d\tau_1 \, d\omega$$

$$\sim -\frac{h_{20}^2}{\rho} \int_0^\varepsilon \frac{\omega \, N_c(\varepsilon - \omega) \, d\omega}{h_{00}^2 + b_c^2(\omega)},$$

$$\gamma_{2c}(\varepsilon) \sim -N_n(0) \int_\Omega \int_0^\varepsilon \operatorname{Im} G_c(\varepsilon - \omega) \, |\Gamma_{22}(\omega)|^2 \, b_c(\omega) \, d\tau_1 \, d\omega$$

$$\sim \int_0^\varepsilon \frac{N_c(\varepsilon - \omega) \, b_c(\omega) \, d\omega}{N_n(0) \, [h_{00}^2 + b_c^2(\omega)]}. \tag{17}$$

Summing up the various contributions to γ_c, we are finally led to a nonlinear integral equation

$$\gamma_c(\varepsilon) = -\gamma_0 \frac{\varepsilon^2}{\varepsilon_F^0} + \int_0^\varepsilon \frac{\gamma_c(\varepsilon - \omega) \, [C_1 h_{20}^2 \eta \, \omega - C_2 \delta_F b_c(\omega)]}{d_c^2(\varepsilon - \omega) \, [h_{00}^2 + b_c^2(\omega)]} \, d\omega, \tag{18}$$

where C_1, C_2 are positive numerical constants of the order of 1, and $\delta_F = \eta\rho/N_n(0) = \eta\varepsilon_F^0 M/M^*$. The propagator $b_c(\omega)$ defined by Eq. (6) reads

$$b_c(\omega) \sim \frac{1}{N_n(0)} \int_\Omega \int_0^\omega \operatorname{Im} G_c(\mathbf{p}, \varepsilon) \operatorname{Im} G_c(\mathbf{p} - \mathbf{q}, \varepsilon - \omega) \, d\tau \, d\varepsilon$$

$$\sim \delta_F \int_0^\omega \frac{\gamma_c(\varepsilon) \, \gamma_c(\varepsilon - \omega) \, d\varepsilon}{d_c^2(\varepsilon) \, d_c^2(\varepsilon - \omega)}. \tag{19}$$

It is easily verified that the FL solution $\gamma_c(\varepsilon) \sim \varepsilon^2$ (the first term in Eq. (18)) fails in the low-energy limit $\varepsilon \to 0$. Indeed, if it were valid then the ratio $\gamma_c(\varepsilon)/d_c^2(\varepsilon)$ could be replaced by $-\pi \delta(\varepsilon)$ and the propagator b_c by a constant. Upon inserting these results into the integral (18) and doing a simple integration, we would obtain a constant term which does not vanish at $\varepsilon \to 0$ as it must, since $\gamma_c(\varepsilon)$ is supposed to be proportional to ε^2.

To find a correct solution at $\varepsilon \to 0$ we employ the scaling approach, assuming

$$\gamma_c(\varepsilon \to 0) = -\gamma_c \, \varepsilon^\nu \, |\ln \varepsilon|^\beta, \tag{20}$$

where γ_c is a positive constant, while ν and β are critical exponents calculated from the requirement of cancellation between the leading terms on the right-hand side of Eq. (18) and $\gamma_c(\varepsilon)$ itself. We shall see that at least one solution has the critical exponent $\nu < 1$. In this case, the ratio $r_c(\varepsilon \to 0) = |\gamma_c(\varepsilon)|/\varepsilon$ diverges, and one may therefore retain in the denominators of Eq. (19) only the term $\sigma_c(\varepsilon) \sim \gamma_c \, \varepsilon^\nu \, |\ln \varepsilon|^{\beta+1}$ together with the analogous term $\sigma_c(\varepsilon - \omega)$.

Upon substituting them into Eq. (19), we are led to

$$b_c(\omega \to 0) = -\frac{\delta_F}{\gamma_c^2} \int_0^\omega \frac{d\varepsilon}{\varepsilon^\nu (\omega - \varepsilon)^\nu \, |\ln \varepsilon|^{\beta+2} |\ln(\omega - \varepsilon)|^{\beta+2}} \simeq \frac{\delta_F}{\gamma_c^2} \omega^{1-2\nu} |\ln \omega|^{-2\beta-4}. \tag{21}$$

Inserting this term into Eq. (18), we find that the term with the factor C_2 prevails on the right-hand side of Eq. (18). The requirement of its cancellation with $\gamma_c(\varepsilon)$ itself yields

$$\nu = 1/2, \quad \beta = -3/2, \quad \gamma_c^2 \simeq \delta_F / h_{00}. \tag{22}$$

Knowing $\gamma_c(\omega)$ and $b_c(\omega)$, one can straightforwardly evaluate the damping $\gamma_{2n}(\varepsilon)$ from Eq. (16). One obtains $\gamma_{2n}(\varepsilon) \sim \varepsilon / \ln \varepsilon$, with the numerical factor proportional to the ratio h_{20}^2 / h_{00}. In principle this ratio may be rather small, and then the FL term proportional to ε^2 becomes significant; otherwise, $\gamma_n(\varepsilon \to 0)$ is practically a linear in ε function with a prefactor of the order of 1. Collecting all the results, one finally obtains

$$\gamma_c(\varepsilon \to 0) \sim -\sqrt{\frac{\delta_F}{h_{00}} \frac{\varepsilon}{|\ln \varepsilon|^3}}, \quad b_c(\omega \to 0) \sim \frac{h_{00}}{\ln \omega}, \quad \gamma_n(\varepsilon \to 0) \sim -\frac{h_{20}^2}{h_{00}} \frac{\varepsilon}{|\ln \varepsilon|} + O(\varepsilon^2). \tag{23}$$

It can be verified that this is the single solution of the problem. Thus the damping of normal excitations at low energies exhibits marginal behavior with a factor of the order of 1, while the damping of the FC states is enormously enhanced. This means that for dealing with the damping of single-particle states beyond the FC phase transition point, FL theory fails even in the limit $\varepsilon \to 0$.

Solution of the integral Equation (18) is also greatly facilitated at sufficiently high energies that the characteristic values of $r_c(\varepsilon)$ in the integrals standing on the left-hand

side of Eq. (18) are less than 1. In this case, $N_c(\varepsilon)$ can be replaced by $\eta\rho\,\delta(\varepsilon)$, and we are left with an algebraic equation, which after utilization of the relation (19) for b_c and some algebra, takes the form

$$\gamma_c(\varepsilon)\left[1-C_2\,\frac{\delta_F^2\,d_c^2(\varepsilon)}{\gamma_{22}^2\,d_c^4(\varepsilon)+\delta_F^2\,\gamma_c^2(\varepsilon)}\right]=-\gamma_0\frac{\varepsilon^2}{\varepsilon_F^0}-C_1\eta\,\varepsilon\,\frac{\gamma_{20}^2\,d_c^4(\varepsilon)}{\gamma_{22}^2\,d_c^4(\varepsilon)+\delta_F^2\,\gamma_c^2(\varepsilon)}. \quad (24)$$

In the weak-damping limit $r_c\ll 1$, the C_2 term in the square brackets can be omitted, and then formula (10) is recovered. However, as we have seen above, the smallness of $r_c(\varepsilon)$ cannot always hold as ε goes down to zero. More precisely, the weak-damping limit persists until the terms in the square brackets on the lelft-hand side of Eq. (24) start to cancel each other as ε goes to 0. A rough estimate for the ''watershed'' ε_{cr} separating the weak-damping from the from the strong-damping limit can be obtained by setting this sum to zero at the point $\gamma_c=0$. As a result, one obtains

$$\varepsilon_{cr}\simeq\sqrt{C_2}\,(\delta_F/\gamma_{22}). \quad (25)$$

At lower energies, solutions (23) can be applied as a first approximation. At energies $\varepsilon>\varepsilon_{cr}$, the value of $b_c(\varepsilon)\sim\delta_F\gamma_c(\varepsilon)/\varepsilon^2\sim\eta$ becomes small, and, according to Eq. (12), so does the derivative $d\gamma_{2n}(\varepsilon)/d\varepsilon$. Thus the energy dependence of the damping $\gamma_n(\varepsilon>\varepsilon_{cr})$, given primarily by the term (10), again turns out to be linear, with a relatively small slope. More precisely,

$$|\gamma_n(\varepsilon>\varepsilon_{cr})|=\gamma_{2n}+\gamma_1\eta\,\varepsilon+\gamma_0\,(\varepsilon^2/\varepsilon_F^0). \quad (26)$$

Upon substituting the propagator $b_c(\varepsilon)$ given by Eq. (23) into Eq. (16) and integrating over energy, one finds $\gamma_{2n}\sim\delta_F$.

Thus the energy dependence of the damping $\gamma_n(\varepsilon)$ of the normal states in systems with the FC turns out to be more complicated than in a marginal FL: one linear regime with a slope of the order of 1 transforms into another linear regime with a lower slope at energies $\varepsilon\simeq\varepsilon_{cr}$. This result is consistent with recent precise measurements of the linewidths of normal states in the compound Bi2212.[9]

In conclusion, we have analyzed the energy dependence of the damping $\gamma(\varepsilon)$ at a distance from the Fermi surface exceeding the characteristic energy ξ_{FC} of the FC. We have concentrated on the coarse features of this phenomenon without specific attention to numerical factors in the quantities of interest. We have demonstrated that for dealing with the damping of single-particle states in these systems there is no room for Landau theory: even in the limit $\varepsilon\to 0$ the ratio $r(\varepsilon)=|\gamma(\varepsilon)|/\varepsilon$ exceeds unity. Our results for the damping $\gamma_n(\varepsilon)$ differ significantly from those obtained in the theory of nearly antiferromagnetic Fermi liquids[13] and in the model of marginal FLs considered in Ref. 11.

It became clear some ten years ago[11,14] that the analysis of numerous experimental data on the basis of the Luttinger liquid, characterized by a vanishing of the renormalization constant z, is an appropriate guide to understanding the properties of strongly correlated electron systems in solids, including transport phenomena dependent mainly on the damping of the single-particle degrees of freedom. At the same time, other properties of these systems, including the existence of the Fermi surface itself, are known to

be successfully treated within Landau theory. What we have demonstrated in this article is that the fermion condensation model serves as a ''bridge'' connecting the two approaches.

[1] V. A. Khodel and V. R. Shaginyan, JETP Lett. **51**, 553 (1990); Condens. Matter Theor. **12**, 222 (1997).

[2] P. Nozières, J. Phys. France I **2**, 443 (1992).

[3] V. A. Khodel, V. R. Shaginyan, and V. V. Khodel, Phys. Rep. **249**, 1 (1994).

[4] G. E. Volovik, JETP Lett. **59**, 830 (1994).

[5] V. A. Khodel, J. W. Clark, and V. R. Shaginyan, Solid State Commun. **96**, 353 (1995).

[6] Z.-X. Shen and D. S. Dessau, Phys. Rep. **253**, 1 (1995).

[7] J. C. Campuzano *et al.*, Phys. Rev. Lett. **83**, 3709 (1999).

[8] Z.-X. Shen and J. R. Schrieffer, Phys. Rev. Lett. **78**, 1771 (1997).

[9] A. Kaminski *et al.*, http://xxx.lanl.gov/abs/cond-mat/9904390.

[10] A. A. Abrikosov, L. P. Gor'kov, and I. E. Dzyaloshinskiǐ, *Methods of Quantum Field Theory in Statistical Physics*, Prentice-Hall, Englewood Cliffs, N.J. (1963).

[11] C. M. Varma, P. B. Littlewood, S. Scmitt-Rink *et al.*, Phys. Rev. Lett. **63**, 1996 (1989).

[12] V. A. Khodel and M. V. Zverev, http://xxx.lanl.gov/abs/cond-mat/9907061.

[13] A. M. Dyugaev, Zh. Éksp. Teor. Fiz. **70**, 2390 (1976) [Sov. Phys. JETP **43**, 1247 (1976)]; A. J. Millis, Phys. Rev. B **45**, 13047 (1992).

[14] P. W. Anderson, Phys. Rev. Lett. **64**, 1839 (1990).

Asymmetry of the propagation of conformational excitations in a double-strand DNA molecule

V. L. Golo[*)]

M. V. Lomonosov Moscow State University, 119899 Moscow, Russia

Yu. M. Evdokimov

Institute of Molecular Biology, Russian Academy of Sciences, 117984 Moscow, Russia

E. I. Kats

L. D. Landau Institute of Theoretical Physics, Russian Academy of Sciences, 117940 Moscow, Russia

A very simple model describing the conformational degrees of freedom of a double-strand DNA molecule is proposed. It is shown that the characteristic modes of the model consist of an acoustic (longitudinal with respect to the axis of the double helix) and two transverse optical modes. The latter modes are directly related with the deformations of the ideal structure of the double helix, which necessarily leads to softening of one of the optical modes on a finite wave vector. It is found that the conformational excitations propagating in DNA are asymmetric. © *1999 American Institute of Physics.* [S0021-3640(99)01223-2]

PACS numbers: 87.15.Gg, 87.15.He

1. As is well known,[1] the DNA molecule consists of two polynucleotide chains wound into a double helix. In the last few years (especially in connection with the impressive experiments of Ref. 2 on the indirect measurement of the deformation of a DNA molecule under the action of an external force), interest has appeared in the elastic properties of DNA, specifically, the conformational vibrations of the double-strand structure. In order to neglect polymer entropy effects, attention must be confined to the so-called mesoscales, i.e., small segments of the DNA molecule (not exceeding the persistence length $\xi \sim 10^3$ Å) must be considered.

Conformational fluctuations of the DNA molecule are characterized by changes in the relative arrangement of the pairs of bases, i.e., they occur on microscopic scales of the order of the distance between the neighboring pairs of bases (3.4 Å). To describe such processes, we cannot use the macroscopic theory of elasticity, but rather a microscopic model must be used. A complete microscopic model should include a description of the dynamics in $6N$-dimensional phase space (where N is the number of atoms in the DNA molecule; the equilibrium arrangement of these atoms is determined by minimizing the total free energy of the system) taking account of the thermal noise from the surrounding medium. Such a program cannot be implemented fully even on modern computers. How-

ever, for a particular approximation of the interactions the numerical simulation of the Brownian dynamics of a DNA molecule is fully realizable (see, for example, Ref. 3), and neglecting dissipation of the conformational excitations due to the interaction with the surrounding medium, it does not even require a large numerical computation.[4]

In the present letter we propose a minimal model of the conformational dynamics of a DNA molecule. On the one hand this model can be analyzed analytically, while on the other it takes account of the basic physical features of the phenomena, specifically, the presence of two strands forming a helical structure. The justification for our simplified model is that it makes it possible to reproduce certain rough features of the spectrum of modes, found earlier by numerical simulation.[4,3]

The conformational degrees of freedom are important for understanding transcription processes occurring in the DNA molecule under the action of enzymes (see, for example, Ref. 5). These processes do not reduce to small perturbations of the structure of the double helix, which are the subject of the present letter. Our model can be modified to describe these phenomena also, for which anharmonic effects describing the breaking of the hydrogen bonds must be included in it (see, for example, Ref. 6). We note, however, that under natural conditions the number of broken hydrogen bonds is very small (10^{-7}, according to Ref. 7, at room temperature).

2. Following Refs. 4 and 3, we shall use a discrete model of the DNA molecule (a system of particles with a harmonic pair interaction). To describe this pair interaction, we take into account explicitly the equilibrium configuration in the form of an ideal helix. To describe the conformation of a double-strand DNA molecule we employ a vector field $\mathbf{y}_n$, determined at the points of the central line of the molecule, where $\mathbf{y} = 0$ corresponds to the unperturbed structure of the ideal duplex (see also Refs. 6 and 8).

Technically, the Hamiltonian of such a model can be written in the form

$$H_{el} = \sum_n \frac{1}{2\rho} \mathbf{P}_n^2 + \sum_n \frac{K}{2} (\nabla \mathbf{y}_n)^2. \tag{1}$$

Here n enumerates the nodes containing the base pairs, $\mathbf{P}_n$ is the generalized momentum conjugate to the field of conformational displacements $\mathbf{y}_n$, which describes the dynamics of the conformational degrees of freedom at the site n; ρ is a coefficient which has the meaning (and dimensions) of a linear mass density, K is the elastic modulus (ergs/cm), corresponding to the harmonic pair potential. The energy in Eq. (1) contains the covariant derivative ($\nabla \mathbf{y}_n$). A covariant derivative appears because the changes in the field $\mathbf{y}$ relative to the natural (local or Frenet) system of coordinates and the change in the local system itself must be taken into account in the deformation energy of the field $\mathbf{y}$ (which is written in Eq. (1) in the stationary (laboratory) system of coordinates).

Thus, in the discrete model corresponding to the ideal structure of a double helix the covariant derivative can be represented in the form

$$\frac{1}{a} [(\mathbf{y}_{n+1} - \mathbf{y}_n) + \hat{R}_n^{-1}(\hat{R}_{n+1} - \hat{R}_n)\mathbf{y}_n] \equiv [\mathbf{y}_{n+1} - \mathbf{y}_n + \Omega \mathbf{y}_n] \frac{1}{a}, \tag{2}$$

where we have denoted by Ω the matrix

$$\hat{\Omega} = \hat{R}_n^{-1}(\hat{R}_{n+1} - \hat{R}_n) \equiv \hat{R} - \hat{I} \tag{3}$$

and $\hat{R}_n$ is the matrix describing the rotation from the local coordinate system at the site n to the laboratory system, and $\hat{R}$ without an index is the matrix describing a rotation accompanying a displacement by a distance between the base pairs $a = 3.4$ Å .

To find the spectrum of conformational oscillations described by the Hamiltonian (1) it is convenient to switch to the Fourier components

$$\mathbf{y}_q = \frac{1}{\sqrt{N}} \sum_n e^{inqa} \mathbf{y}_n, \tag{4}$$

where N is the total number of sites (base pairs) in the molecular fragment under consideration (of the order of the persistence length).

The Hamiltonian (1) [taking account of the definition (3)] can be diagonalized by the standard method using a canonical transformation. This gives the following dispersion laws for the three modes:

$$\lambda_3 = \frac{2v}{a} \left| \sin \frac{aq}{2} \right|, \tag{5}$$

$$\lambda_{1,2} = \frac{v}{a} [f(\varphi, qa) \pm 2|\sin \varphi \times \sin qa|]^{1/2}, \tag{6}$$

where $v = \sqrt{K/\rho}$ is, dimensionally and physically, the characteristic velocity of conformational oscillations, the angle φ parameterizes an elementary rotation $\hat{R}$ of the ideal double helix

$$\hat{R} = \begin{pmatrix} \cos \varphi & \sin \varphi \\ -\sin \varphi & \cos \varphi \end{pmatrix},$$

and the function f has the form

$$f = 4 \left(1 + 2 \sin^2 \frac{\varphi}{2} \right) \sin^2 \frac{qa}{2} + 4 \sin^2 \frac{\varphi}{2}. \tag{7}$$

The dispersion laws for the conformational modes are shown in Fig. 1. There are an acoustic branch of oscillations (λ_3) and two optically branches $\lambda_{1,2}$.[1] The optical mode λ_1 [corresponding to the minus sign in Eq. (6)] has a quite deep minimum at a finite wave numbee q_*. The DNA duplex, because of the presence itself of the helix, is characterized by an axial anisotropy vector which changes sign at a transition from a right- to a left-hand helix (reflection in a plane parallel to the axis of the helix). The frequency $\lambda_1(q_*) \neq 0$, so that the circular polarizations differ by the signs of the rotation in a pair of waves corresponding to the characteristic mode λ_1.

We also studied the propagation of local disturbances of a double helix, which are described by the so-called covariant wave equation following from the Hamiltonian (1). For this, the initial perturbation must be represented as a superposition of the characteristic modes found above, and the coefficients in this superposition must be found from the initial and boundary conditions. Leaving to a separate work the detailed investigation of solutions of this equation, here we only formulate the interesting, in terms of the biophysical consequences, qualitative features of the propagating disturbances. The co-
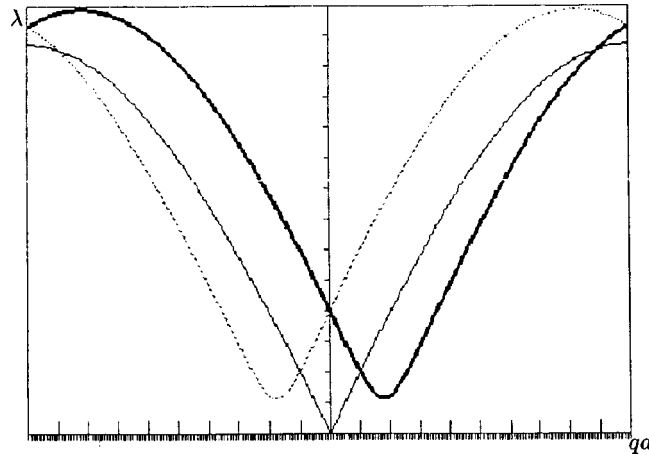
FIG. 1.

variant wave equation describes excitations propagating in both directions along the axis of the double helix. Depending on the structure (amplitude and polarization) of the initial excitation and the parameters of the model, these waves can have either the same or opposite signs of the elliptical polarization of both waves (i.e., in the waves traveling in both directions the displacements $\mathbf{y}_n$ of the polynucleotide chains can rotate in the same direction (in-phase) or in opposite directions, i.e., in antiphase).

Formally, the reason for such asymmetry in a mirror symmetric (with respect to the reflection plane perpendicular to the axis of the helix) ideal structure of a double helix (here we neglect, for simplicity, the dependence of the model parameters on the sequence of the base pairs) is quite obvious. The initial perturbation of the duplex, having different amplitudes of displacements $\mathbf{y}$ along arbitrary axes in a plane perpendicular to the axis of the helix (i.e., elliptical polarization), excites different superpositions of the optical modes λ_1 and λ_2. When the direction of propagation is reversed (or, equivalently, $q \to -q$), because of the helical symmetry the relation $\lambda_1(-q) \to \lambda_2(q)$ holds, and for this reason, in general, the polarizations of the waves propagating in opposite directions are different.

3. Thus, in the present letter we have formulated a very simple model of the double-strand structure of DNA. The proposed model, using a small number of phenomenological parameters (K, ρ, a, φ), we hope, adequately describes the conformational degrees of freedom of the double-strand DNA molecule.

The parameters a and φ are determined by the structure of the DNA molecule and are well known ($a = 3.4 \times 10^{-8}$ cm; $\varphi = \pi/5$). The linear mass density ρ in all organic polymers does not vary much, and in order of magnitude it can always be estimated as 1 g/cm$^3 \times d^2 \approx 10^{-14}$ g/cm (where $d \approx 20$ Å is the diameter of a polynucleotide chain).

The recent results of Ref. 9 can be used to estimate the elastic modulus K. In this work the force required to separate the two polynucleotide chains of DNA to a distance of the order of 10^{-4} cm was measured directly. Dimensionally (and physically) this force

can serve as an upper limit of the conformational elastic modulus K which we have introduced. Using the data presented in Ref. 9, we obtain $K \sim 10^{-6}$ ergs/cm.

Thus, all the parameters of our model have been determined, and the characteristic propagation velocity of conformational excitations can be calculated from Eqs. (5) and (6) as $v \simeq 10^5$ cm/s. These conformational excitations are small (they do not break the hydrogen bonds between the base pairs) perturbations of the double helix, similar to phonons in crystal lattices. Taking account of the dissipation will inevitably cause the excitations which we have found to decay. It cannot be ruled out that a purely relax-ational dynamics arises instead of propagating waves (as most often happens in proteins). However, the DNA molecules on mesoscales are much more rigid than proteins, so that dissipation may not lead to overdamping of the conformational modes. Rough estimates[5] of the dissipation due to the interaction of the conformational degrees of freedom with the surrounding medium show that this dissipation can indeed be neglected.

In biology, transcription processes which do not reduce to small perturbations of the duplex play an important role. In Ref. 5 the phenomenon of transcription in the *B* form of DNA was studied under conditions where the rotation of the enzyme inducing transcrip-tion is hindered and, instead, twisting of the DNA molecule itself occurs. This twisting will lead to superspiralling of the DNA molecule. As the enzyme moves, the direction of rotation of the polynucleotide chains in front of it is opposite to that behind it.

An important question is the choice of the direction of motion of the enzyme, which under certain conditions propagates in the direction of positive superspiralling while in other cases it propagates in the direction of negative superspiralling. Our results show the presence of a natural asymmetry of propagation of excitations even in an absolutely symmetric conformation of the double helix. This asymmetry is determined primarily by the structure of the initial perturbation of the duplex. The dependence of the model parameters on the sequence of base pairs gives a second possible reason for asymmetry of propagating excitations.

In summary, depending on the polarization of the initial perturbation and the param-eters of the model, the perturbation can propagate in the direction of positive and nega-tive superspiralling, and the relative rotation of the polynucleotide chains in both waves can occur in- or antiphase.

[*])e-mail: golo@mech.math.msu.su
[1])The vibrational modes of a mechanical model of DNA were first analyzed in Ref. 4.

[1] W. Saenger, *Principles of Nucleic Acid Structure* (Springer-Verlag, New York, 1984).
[2] S. B. Smith, L. Funzi, and C. Bustamante, Science **258**, 1122 (1992).
[3] K. V. Klenin, M. D. Frank-Kamenetskii, and J. Langowski, Biophys. J. **68**, 81 (1995).
[4] H. Cappelmann and W. Beim, Z. der Phys. **209**, 276 (1968).
[5] L. F. Liu and J. C. Wang, Proc. Natl. Acad. Sci. USA **84**, 7024 (1987).
[6] T. Dauxois, M. Peyrard, and A. R. Bishop, Phys. Rev. E **47**, R44 (1993).

[7] M. Gueron, M. Kochoyan, and G. L. Leroy, Nature (London) **328**, 89 (1987).
[8] V. L. Golo, Yu. M. Evdokimov, E. I. Kats, and S. G. Skuridin, Zh. Éksp. Teor. Fiz. **115**, 940 (1999) [JETP **88**, 517 (1999)].
[9] B. E. Roulet, U. Bockelmann, and F. Heslot, La Recherche, **316**, 37 (1999).

Translated by M. E. Alferieff